Computational Studies of Blood Flow at Arterial Branches in relation to the Localisation of Atherosclerosis

by

Asimina Kazakidi

Department of Aeronautics
Imperial College London, London SW7 2AZ

This thesis is submitted for the degree of Doctor of Philosophy of the University of London

2008

Abstract

Atherosclerotic lesions are non-uniformly distributed at arterial bends and branch sites, suggesting an important role for haemodynamic factors, particularly wall shear stress (WSS), in their development. Using computational flow simulations in idealised and anatomically realistic models of aortic branches, this thesis investigates the role of haemodynamics in the localisation of atherosclerosis.

The pattern of atherosclerotic lesions is different between species and ages. Such differences have been most completely documented for the origins of intercostal arteries within the descending thoracic aorta. The first part of the thesis deals with the analysis of wall shear stresses and flow field near the wall in the vicinity of model intercostal branch ostia using high-order spectral/*hp* element methods. An idealised model of an intercostal artery emerging perpendicularly from the thoracic aorta was developed, initially, to study effects of Reynolds number and flow division under steady flow conditions. Patterns of flow and WSS were strikingly dependent on these haemodynamic parameters. Incorporation of more realistic geometrical features had only minor effects. The WSS distribution in an anatomically correct geometry of a pair of intercostal arteries resembled in character the pattern seen in the idealised geometry. Under unsteady and non-reversing flow conditions, the effect of pulsatility was small. However, significantly different patterns were generated for reversing aortic near-wall flow and reversing side branch flow.

The work was extended to study the wall shear stress distribution within the aortic arch and proximal branches of mice, in comparison to that of men. Mice are increasingly used as models to study atherosclerosis and it has been shown that, in knockout mice lacking the low density lipoprotein receptor and apolipoprotein E,

lesions develop in vivo at the proximal wall of the entrance to the brachiocephalic artery. Three aortic arch geometries from wild-type mice were reconstructed from MRI images using in-house and commercial software, and the WSS distribution was calculated under steady flow conditions to establish the mouse haemodynamic environment and mouse-to-mouse variability. Approximated human aortic arch geometries were further considered to enable comparison of the flow and WSS fields with that of mice. The haemodynamic environment of the aortic arch varied between the two species. The overall distribution of wall shear stress was more heterogeneous in the human aortic arch than in the mouse arch, although some features were similar. Intraspecies differences in mice were small and influenced primarily by the detailed anatomical geometry and the Reynolds number.

A number of simplifications were made in the above flow analyses, and clearly, relaxing these assumptions would increase complexity. Nonetheless, this thesis demonstrates the fundamental features of flow, which underlie the disparate patterns of WSS in different species and/or ages, for simplified cases, and the results are expected to be relevant to more complex ones. Aspects of the observed WSS patterns in the simplified model of intercostal artery correlate with, and may explain, some of the lesion patterns in human, rabbit and mouse aortas. WSS distributions in the aortic arch of wild-type mice associate with lesion locations seen in diseased mice.

To my newborn niece

and my sister

Acknowledgments

I would first like to thank my supervisors, Professors Spencer Sherwin and Peter Weinberg, for their excellent supervision and their expert advice and guidance throughout this study, for their support and patience, and for proof-reading this thesis and many other documents related to this work. I am grateful to them for giving me the opportunity to attend several conferences, meetings etc. within the UK and abroad, which helped in my research. Furthermore, I would like to thank all the people from the Department of Bioengineering, where I previously completed a one-year MSc course, and especially the late Professor John Lever and Professors Kim Parker and Colin Caro, for the support and encouragement to start and continue this research. My thanks also go to Drs Denis Doorly and Joaquim Peiro, from the Department of Aeronautics, for their constructive suggestions.

I am grateful to Drs Martina McAteer, Jurgen Schneider, Robin Choudhury and Professor Keith Channon, from the John Radcliffe Hospital, Oxford, for generously providing the MR images used in the study of wall shear stress in the aortic arch. I would also like to thank Dr Declan O'Regan from the Hammersmith Hospital for generously providing an MRI dataset of a human aortic arch, although it was not presented in this thesis. Finally, many thanks go to Dr Bettina Nier and Mr Anthony Hunt for letting me attend real-time experiments and aortic casting procedures, and especially to Dr Bettina Nier for providing the micro-CT images used in the study of flow around intercostal arteries.

However, this research would not have been possible without the financial assistance provided by the Institute of Biomedical Engineering, IC, the Alexander S. Onassis Public Benefit Foundation, and an EPSRC Doctoral Training Account from

the Department of Aeronautics, IC, to all of which I express my gratitude. I would also like to thank the Imperial College Trust, the Royal Academy of Engineering, and the EU Marie Curie fellowships for awarding me conference grants and scholarships to attend conferences and a training course during this work.

It has been a great pleasure to work with the people from both the Physiological Flow Studies (PFSG) and the Bio-Flow Groups, to whom I am most grateful. In particular, many thanks go to Donal Taylor for his technical advice and to Adrian Lee for his help early on in this work. A big thank-you to my office mates in E557 between 2004-2006, Nina Nier, Costas Anastassiou, Stephanie Cremers, and Andrew Bond, for their patience, encouragement and fun! Also, many thanks to Jazmin Aguado, Chistina Warboys, Jordi Alastruey, Severin Harvey, Yoko Kikuchi, Elena Phoka, Pei Ling Leow, Eleni Bitziou, Bhavik Patel, Zhao Hong, Nicholas Foin, Gianfilippo Coppola, Alberto Gambaruto, Adelaide De Vecchi, Peter Vincent, Michael Broadhurst, Nadir Abdessemed and many other people from both Departments.

I would also like to thank the Warden of Lillian Penson Hall, Dr Martin Usoh, for giving me the opportunity to remain in the hall for the duration of my studies, for the position of senior resident and his support. A special thank-you to Sinan Arkin, Constantine Athanasiadis and Jose Bellido, for being there for me at difficult times and for making the life in the hall pleasant and fun! Also, many thanks to my friends, Hercules, Angeliki and George (and their upcoming baby!), Efi and Giannis, Eleni, Bill, Christina, Mari, Evi, Niki and Filippos (and their children, Eirini and Michael), Panos, Masako and Colin (and their son, Tom), Robin, Dario, Vasilis, Dimitris, Christos, and Savina, for their encouragement.

Finally, a special HUGE thank-you to my family Lena, Anestis, Menia and (let's not forget the dog!) Andri, and Natali, Dimitris and their beautiful newborn baby girl, for their tireless care, patience and continuous encouragement all these years. I dedicate this thesis to my sister and my niece who was born the day I submitted the last chapter!

London, September 2008

Preface

This thesis describes work carried out in the Departments of Aeronautics and Bioengineering at Imperial College London under the supervision of Professors Spencer J. Sherwin and Peter D. Weinberg. It was financially supported by the Institute of Biomedical Engineering, IC, the Alexander S. Onassis Public Benefit Foundation, and an EPSRC Doctoral Training Account from the Department of Aeronautics, IC. I declare that the work presented in this thesis is my own, except where acknowledged.

Asimina (Melina) Kazakidi

Contents

List of Figures

Chapter 1

Introduction

Atherosclerosis, an inflammatory disease, is the underlying cause of most cardiovascular diseases, including coronary heart disease[1], peripheral artery disease, heart failure, and stroke. Cardiovascular diseases at present are the leading cause of death, accountable for 30% of all deaths globally in 2005 (WHO, 2007), and are projected to remain so in the future according to the World Health Organisation. It is of no surprise, therefore, that the need for elucidating the mechanisms involved in the development and progression of these diseases is urgent and has been the subject of active research in the past decades.

Despite intensified research, there is currently controversy over the exact processes involved in the initiation and localisation of atherosclerosis. The reason may lie in the sheer complexity of the cardiovascular system, where multiple interactions take place. Several methodologies have been employed in an attempt to understand the functions of the vascular system, for example, in vivo and ex vivo experimentations on humans or animals, in vitro observations, or analysis using mathematical models. The implementation of numerical methods in the solution of equations describing the blood flow in arterial vessels has attracted considerable attention in recent years, mainly due to their capability of quantifying variables not measurable in vivo, their reproducibility and reliability, and their role as diagnostic and treatment tools for disease conditions. Limitations in the use of numerical methods are related primar-

[1] Coronary heart disease is the main cause of angina, myocardial infarction (heart attack) and sudden cardiac death.

ily to the complexity of the systems they can examine[2], restricting them, hence, to more simple and basic theoretical problems. Abstract and simplified interpretations, however, have always been the cornerstone of understanding the physical world.

In relation to the initiation and localisation of atherosclerosis, this thesis focuses on the investigation of blood flow at arterial branches of (i) the descending thoracic aorta and (ii) the aortic arch, using computational methods for fluid dynamics. Specifically, it develops simplified and anatomically correct three-dimensional models of the thoracic aorta and aortic arch—increasing, therefore, the complexity from previous one- or two-dimensional models—to study flow and wall shear stress distribution near branch ostia. This thesis attempts to answer controversial issues concerning the localisation of atherosclerosis and establish detailed blood flow characteristics within the two arterial sections.

This chapter gives a brief overview of the clinical aspects of atherosclerosis and a current proposed theory of atherogenesis, at a molecular level. It describes the role of wall shear stress in atherosclerosis by documenting prior literature and presenting some elementary fluid mechanics aspects of flow in blood vessels. It sets the motivation for this research, and describes the objectives and general approach considered. Finally, it reports on publications of work presented in this thesis and a synopsis of the remaining thesis.

1.1 Pathophysiology of atherosclerosis

Atherosclerosis is a disease affecting mainly the larger systemic arteries of the cardiovascular system[3]—the aorta and its major branches—and is characterised by the focal accumulation of lipids, inflammatory cells and connective tissue components within the arterial wall. Local accumulation of lipids and the formation of foam

[2]Cost-effectiveness, computer power and other issues are also important (See Chapter 2 for more details on numerical methods).

[3]The human circulatory system is a closed system transporting nutrients, oxygen and waste throughout the body. The *systemic circulation* transports oxygenated blood from the left heart to the body and returns deoxygenated blood to the right heart. The *pulmonary circulation* moves the deoxygenated blood through the lungs to oxygenate it and return it to the left heart.

cells generate the early lesions (*fatty streaks*), which can be detected as early in life as early childhood (Rose, 1991; Ajjan and Grant, 2006). A cascade of processes can gradually lead to the formation of a plaque, known as *atheroma*, which protrudes into the lumen of the vessel and causes narrowing (*stenosis*[4]) or occlusion. The disease may remain clinically silent for many years, until an abrupt change in the environment and composition of the plaque may induce fissuring in the cap of the plaque that allows the formation of a thrombus and later causes embolism (Richardson et al., 1989; Lucas and Greaves, 2001; Ajjan and Grant, 2006). It is still unclear what exactly causes a plaque to become unstable and rupture.

Several risk factors exacerbate the disease, such as smoking, high blood pressure, increased concentration of cholesterol in the blood, and diabetes (Rose, 1991). Although recent advances in medical imaging have allowed for earlier diagnosis of the disease and the success rate of currently available treatments is high, the high rate of restenosis remains a major limitation.

1.1.1 Theory of atherogenesis

It is now well accepted[5] that atherogenesis is associated with damage to the endothelium (*endothelial dysfunction*), which is the innermost layer of the arterial wall and is in direct contact with the flowing blood. Endothelial cells line the surface of the intima with only small gaps between the cells, about $200\mathring{A}$ wide (Bergel et al., 1976). The endothelium is further covered by a porous endothelial glycocalyx layer, a network rich in carbohydrates (Reitsma et al., 2007). The endothelial glycocalyx layer has recently received great attention due to its possible role in the vascular biology of atherogenesis (Davies, 1995).

Endothelial cells, when they are healthy, protect the vessel wall from inflamma-

[4]There are several features that differentiate advanced atherosclerotic plaques such as a concentric or eccentric lipid pool within the arterial wall and a thick (stable) or thin (unstable) fibrous cap overlying the plaque. The majority of the plaques, however, appear to be eccentric to the axis of the vessel (Richardson et al., 1989; Lucas and Greaves, 2001).

[5]Despite the recent attention due to the increasing number of individuals affected, atherosclerosis is not a problem studied only in the present day. Rudolf Virchow proposed the initiating role of inflammation in atherosclerosis from as early as the mid 19th century (Mayerl et al., 2006).

tion and prevent the migration of inflammatory cells. High concentrations of low density lipoprotein (LDL) molecules from the blood may build up in the lesion after entering the wall. Once within the wall, LDL molecules are oxidised to form ox-LDL molecules which are known to promote atherogenesis (Figure 1.1, After Hansson et al., 2006). Damage to the endothelium activates the endothelial cells and allows the expression of adhesion molecules on their surface. These adhesion molecules bind inflammatory cells from the blood stream and let them migrate into the vessel wall.

The inflammation continues with the recruitment of T cells to the site of early lesions and the activation of macrophages. Multiple processes take place at this stage which result in the formation of foam cells (Figure 1.1, After Hansson et al., 2006). Local accumulation of lipids contributes to the formation of a core in the atheromatous plaque. In addition, proliferation and migration of vascular smooth muscle cells at the site of inflammation promotes the enlargement of the atheroma. The fibrous cap covering the lesion is originally thin but is stabilised with collagen. However, activation of macrophages produces matrix metalloproteinases (MMP) which result in the weakening of the cap by degradation of the collagen. This causes the plaque to destabilise and become vulnerable. Plaque rupture brings the blood in contact with the material in the plaque, resulting in the formation of a thrombus and possibly embolism (Hansson et al., 2006; Ajjan and Grant, 2006; Krams et al., 2003).

1.2 Shear stress and atherosclerosis

One significant observation is that atherosclerosis is not distributed uniformly within the arterial system; rather, it is highly patchy and shows a predilection for curvature and branching points (Figure 1.2 shows a line graph of lesions localisation in the apolipoprotein E-deficient mouse; after Nakashima et al., 1994). Some regions of the arteries appear to be protected from the disease, whereas others are prone to it. Even when advanced atherosclerotic plaques have developed in one location within an artery, nearby locations may show no sign of the disease. The reasons why this occurs have not yet been established and remain under investigation. If the properties of the wall in regions free from the disease were known, one could

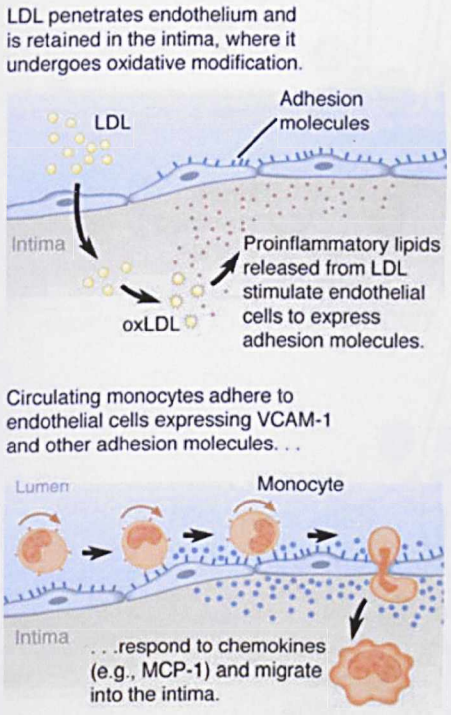

Recruitment and activation of macrophages in atheroma. Macrophages, which are abundant in atheroma, are recruited from blood monocytes that enter through the surface endothelium. In advanced lesions, plaque microvessels may also provide a route of entry for monocytes. Several leukocyte adhesion molecules and chemokines govern the recruitment process, which is followed by differentiation of the monocytes into macrophages. During this process, pattern recognition receptors, such as scavenger receptors (ScRs), are upregulated. ScRs mediate the uptake of oxidized low-density lipoprotein (oxLDL), and cause the accumulation of LDL-derived cholesterol and foam-cell formation. Other macrophages are primed for activation when stimulated by the T cell cytokine, interferon-γ (IFNγ). These macrophages are activated by pathogen-associated molecular patterns that ligate toll-like receptors (TLRs), as well as the pro-inflammatory cytokines interleukin (IL)-1 and tumor necrosis factor (TNF). As a result of activation, the macrophages release a host of pro-inflammatory mediators, including reactive oxygen and nitrogen species, pro-inflammatory cytokines, vasoactive molecules, and several kinds of proteases. Th1, T helper-1; MCP-1, monocyte chemoattractant protein-1; M-CSF, macrophage-colony-stimulating factor; VCAM-1, vascular cell adhesion molecule-1; HSP60, heat shock protein 60.

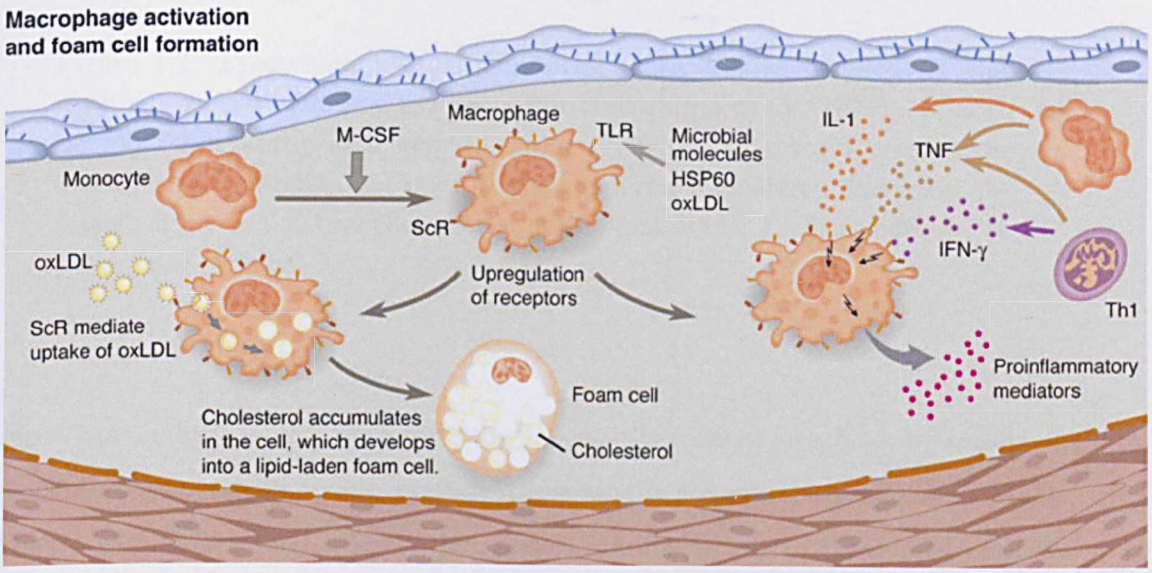

Figure 1.1: Initiation mechanism of atherosclerosis: Endothelial activation (top), Macrophage activation and foam cell formation (bottom) (After Hansson et al., 2006).

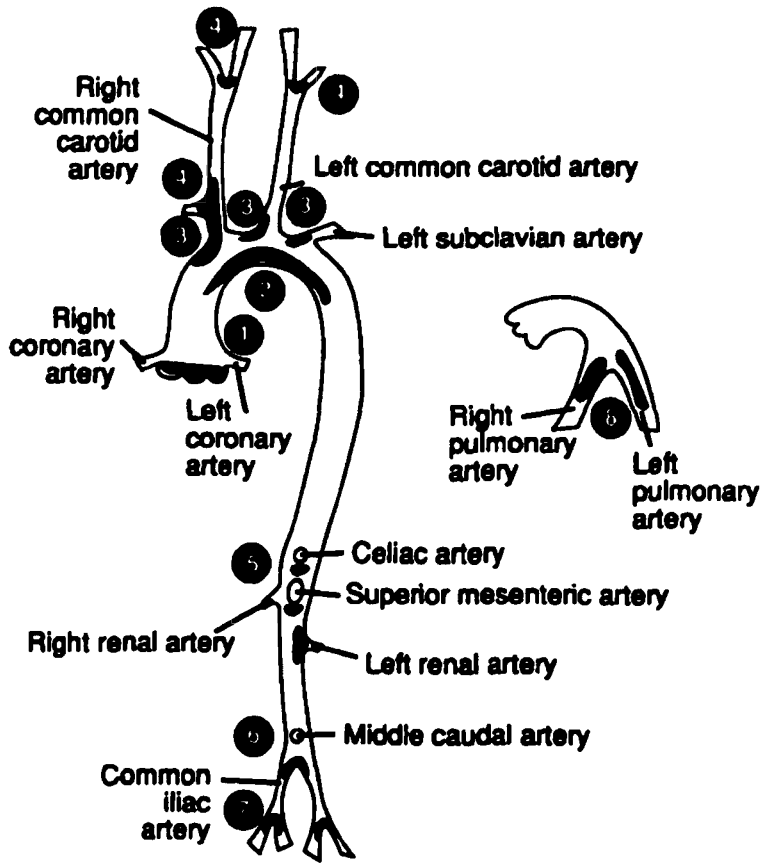

Figure 1.2: Predominant sites of atherosclerotic lesions (shaded) in the apolipoprotein E-deficient mouse (After Nakashima et al., 1994). 1: aortic root, 2-3: aortic arch and its major branches, 4: carotid arteries, 5: branches of the abdominal aorta (celiac, superior mesenteric, and renal arteries), 6: terminal branches of the abdominal aorta, 7: iliac arteries, 8: pulmonary arteries.

argue that induction of these properties in pro-atherogenic locations, by means of pharmacological agents, could prevent or eventually reverse the progression of the disease. Understanding, hence, what makes atherosclerosis to be a focal disease, affecting only discrete regions of the vasculature and not others, is crucial, since this can contribute to the development of future treatment methods and therapeutic strategies.

Several factors are believed to affect this preferential distribution of atherosclerotic lesions. Nevertheless, there are perhaps only three main elements that play a part:

the *vessel wall*, and its components[6]; the *blood*, and its constituents; and the *flow* of the blood, and its characteristics. These elements may interact either in a purely mechanical or biological way, or in combination; that is, when mechanical stimuli initiate biological or chemical activity. Mechanical forces are applied through the exertion of stresses on the wall by the flow of blood. Biological processes, at a molecular, cellular and/or genetical level, are identified through activation of cells and expression of molecules within the wall. Biological or biochemical activity due to applied mechanical forces is observed in processes like vessel wall mass transport[7] (Tarbell, 2003), endothelial mechanotransduction[8] (Davies, 1995), and others.

The stresses that blood flow exerts on the vessel walls are thought to be of critical significance in relation to the patchy distribution of atherosclerotic lesions. Mechanical stresses can be resolved into stresses applied tangentially to the vessel wall (*shear stress*), and those applied in the normal direction to the wall (*pressure*). Of these two, pressure is thought to play a minor role in the distribution of lesions compared to that of shear stress. This is because pressure acts approximately uniformly on the vessel wall as a whole; its fluctuations due to the nature of blood flow are considered insignificant compared to the variations in shear stress which depends on the local velocity gradients and therefore varies substantially along the vasculature due to the non-uniformity of the blood flow pattern.

[6]The wall of the blood vessels consists of three layers (from the vessel lumen outwards): the *tunica intima*, the *tunica media*, and the *tunica adventitia*. The former is the thinnest layer of all and is covered with endothelial cells; the tunica media is the thickest layer, while the tunica adventitia of the aorta and larger arteries also contains a network of nutrient capillaries (*vasa vasorum*) which can penetrate the tunica media from the side of the adventitia (White, 1989; Langheinrich et al., 2007).

[7]The vessel walls are porous and permeable, and allow the transport of materials between the blood and the subendothelial space. A full review concerning possible mass transport mechanisms can be found in Tarbell (2003).

[8]Endothelial mechanotransduction refers to the activation of multiple biochemical mechanisms, such as the activation of ion channels and signalling pathways, in response to mechanical stimuli originating from the flow of blood or from blood pressure. See Davies (1995) for a detailed analysis of possible transduction mechanisms.

1.2.1 Current consensus

For the past forty years or so, there has been much research attempting to identify the exact role of shear stress in the distribution of atherosclerosis. Early work by Fry (1969) and Caro et al. (1971) showed contradictory results; the former reported occurrence of lesions at sites with high shear stress, the latter at sites with low shear stress. The controversy remained for years and sparked intense research in the field with the use of experimental (in vitro and in vivo), theoretical and computational methods. To this contributed also the difficulty in measuring velocity profiles and gradients in vivo and hence accurately estimating in vivo wall shear stress. Today, there is accumulating evidence that atherosclerotic lesions are unlikely to develop at regions of high shear; instead, lesion patterns are recognised at regions where the wall shear stress is low and/or is spatially and temporally oscillating (Caro et al., 1971; Ku et al., 1985). Furthermore, it is widely accepted that endothelial cells sense changes in the wall shear stress and can vary their shape and orientation as a result (Langille and Adamson, 1981; Malek et al., 1999). Finally, there is increasing evidence that processes such as mass transfer between the blood and the vessel wall and endothelial signalling depend highly on shear stress (Tarbell, 2003; Davies, 1995).

1.2.2 Challenging features

However, human atherosclerotic lesions appear to change location with age. Studies near side branches of the human aorta have shown that during the foetal period, and infancy, sudanophilic lesions (early atherosclerosis) occur in a confined region downstream of the origins of branches (Sinzinger et al., 1980); in young adulthood, fatty streaks develop laterally and, later in age, upstream of the branch mouth (Svindland and Walløe, 1985; Sloop et al., 1998); finally, in elderly people the disease completely surrounds branch ostia (Mitchell and Schwartz, 1965). Investigations have been made also in rabbit (Cornhill and Roach, 1976; Barnes and Weinberg, 1998), murine (McGillicuddy et al., 2001), and pigeon (Cornhill et al., 1980; Richards and Weinberg, 2000) aortas, where several different lesion patterns have been observed. Rabbit atherosclerotic lesions in weanlings and mature rabbits are similar to the two earliest distributions seen in humans (Barnes and Weinberg, 1998, 1999,

2001), whereas lesions in mice of all ages are comparable to disease patterns of aged people (McGillicuddy et al., 2001; Weinberg, 2002). Consequently, age—and species—appear to be important in the distribution of atherosclerosis[9]. This implies that there may be changes in the shear stress forces applied on the vessel wall with age and/or species.

1.2.3 Blood flow mechanics in arteries

To demonstrate the importance of shear stress in the arteries and its local variations, we briefly present here, following in parts the description of Caro et al. (1985), some basic aspects of the mechanics of blood flow in idealised geometries. The arteries are considered as circular tubes with rigid walls, and the viscosity of the flow is assumed constant (Newtonian fluid[10]). These assumptions clearly do not represent the arteries in vivo, but are thought to capture the major features of the flow in the larger arteries[11]. For a detailed analysis of these concepts see Caro et al. (1978) and Pedley (1980).

1.2.3.1 Steady flow

Shear stress

Shear stress, τ, is the tangential force exerted on the vessel wall by the flow of blood. For a Newtonian fluid, shear stress is proportional to the gradient of the velocity, dU/dr (*shear rate*), and is given by:

$$\tau = \mu \frac{dU}{dr} \tag{1.1}$$

where μ is the dynamic viscosity, and r is the radial direction. For flow moving next to solid boundaries the *no-slip* condition applies, which states that the velocity of the fluid is zero at the solid surface.

[9] In the current discussion, we ignore effects of certain dietary loads on atherosclerosis, for example in anorexic or obese people, and focus primarily on effects of age and species.

[10] In reality, blood is composed of blood cells (red blood cells, white blood cells and platelets) suspended in plasma, an aqueous solution. Therefore, blood is a non-Newtonian fluid; that is, the viscosity varies with the applied shear rate.

[11] Blood flow is to a large extent laminar, but under certain conditions may undergo instabilities and transition to turbulence. See Parker (1977) for a detailed analysis of blood flow instabilities.

Reynolds number

The characteristic dimensionless parameter that describes viscous flows is the Reynolds number, Re_D, defined as:

$$Re_D = \frac{\rho U D}{\mu} \tag{1.2}$$

where D is the characteristic length (here taken as the diameter of a circular tube), U is the characteristic velocity (for example, the mean cross-sectional velocity), and ρ is the density of the Newtonian fluid. The Reynolds number is a measure of the ratio of inertial forces (ρU^2) to viscous forces ($\mu U/D$). Thus, at high Reynolds numbers, inertial forces are dominant, whereas viscous forces become significant only at low Reynolds values. Blood flow in the aorta and larger arteries take Reynolds values of several hundreds up to a few thousands. In those arteries, therefore, inertial forces prevail ($Re_D >> 1$).

Flow in a straight pipe

Figure 1.3 shows the development of steady laminar flow in a straight tube. At the entrance to the pipe the velocity profile is almost uniform. Due to the no-slip condition, the velocity is zero at the walls and a velocity gradient is immediately generated with the neighbouring moving fluid. As a result of this traction, high shear stress appears on the wall and a *viscous boundary layer* starts to grow. The boundary layer progressively decelerates the near-wall fluid, while a concomitant acceleration occurs at the centre of the tube. The shear stress is gradually reduced on the wall, until it becomes constant when the boundary layer has filled the tube and a parabolic velocity profile has been established. This is the well-known steady fully-developed laminar flow (*Poiseuille flow*). The entrance length L—that is, the length in the tube until a fully developed velocity profile develops—is approximately equal to $0.03 Re_D D$ (Parker and Caro, 1993). For a Reynolds number of 1500, the entrance length would be about 45 aortic diameters and, hence, Poiseuille flow type velocity profiles would not occur in the aorta under steady flow. The boundary layer thickness, δ, is proportional to $Re_L^{-1/2} x$, where Re_L is the Reynolds number with respect to the distance L from the entrance of the tube, and x is the axial direction.

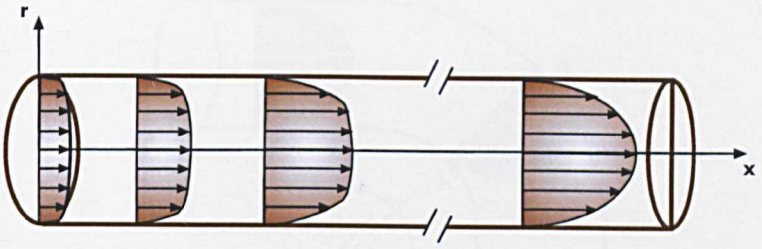

Figure 1.3: Development of steady laminar flow at the entrance of a straight circular rigid pipe (Reproduced after Caro et al., 1985).

Flow in a curved pipe

In curved tubes (Figure 1.4), the curvature forces fluid particles to change direction and accelerate in order to preserve the axial flow. A large pressure gradient is developed that drives this acceleration. If the initial flow is fully developed, the central highest velocities have high inertia and cannot be easily deflected. Fluid near the wall has less inertia and therefore is greatly displaced. Consequently, the highest velocities do not occur in the centre but are found closer to the outer wall of the curvature. The displacement also generates secondary motion in the transverse plane in the form of two counter-rotating vortices (*Dean vortices*), as shown in Figure 1.4. The skewness of the velocity profile implies that in a curved tube high shear stress is developed on the outer wall, and low shear stress on the inner wall (denoted as H and L in Figure 1.4, respectively).

Flow in a bifurcation

The arterial system has many generations of branching, with the aorta branching into the major arteries, the arterioles and finally into the capillaries. Figure 1.5 demonstrates two general examples of Poiseuille flow in idealised bifurcating tubes. Fast moving flow arriving at the flow divider of the bifurcation is forced to follow one of the two branches. Due to its high inertia, the acting pressure gradient cannot displace it immediately into the axial directions of the daughter branches and, hence, the flow moves next to the inner walls of the bifurcation. High shear is developed, as a result, on the flow divider. On the contrary, near-wall fluid in the parent vessel has less inertia and can be greatly deflected. This generates secondary motion

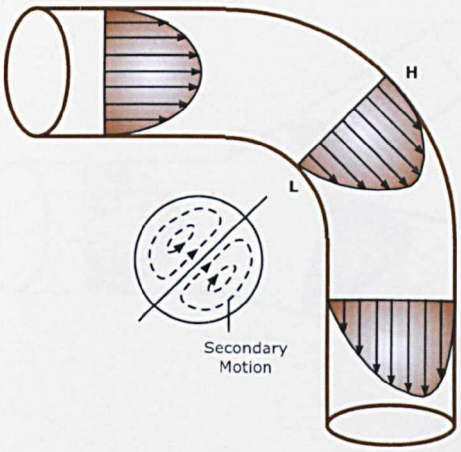

Figure 1.4: Steady flow in a rigid curved pipe and the presence of secondary motion with the formation of two Dean vortices (Reproduced after Caro et al., 1985). Due to skewness of the velocity, high shear (H) develops on the outer wall of the curvature and low shear (L) on the inner wall.

in the transverse plane, while low shear regions develop on the outer walls of the bifurcation. New boundary layers develop along the inner walls that eventually re-establish the Poiseuille flow type in both daughter branches further downstream. At very high initial velocities and sharp angles, large pressure gradients may cause separation of the flow and the formation of a recirculation zone or flow reversal at the outer walls (Figure 1.5b). Such zones are characterised by high particle residence times and low values of wall shear stress.

Arterial geometry

It is apparent from the above analysis that the exact geometry of a tube can influence the distribution of the velocity and wall shear stress, and can therefore alter the characteristics of the flow giving rise to various forms of secondary motion (Schroter and Sudlow, 1969; Caro et al., 2002; Sherwin et al., 2000b). In fact, arteries in vivo are in general three-dimensional and non-planar, in addition to being branched (Caro, 2001; Caro et al., 1996), implying that a detailed knowledge of their geometry is often essential to identify local distributions of flow and wall shear stress.

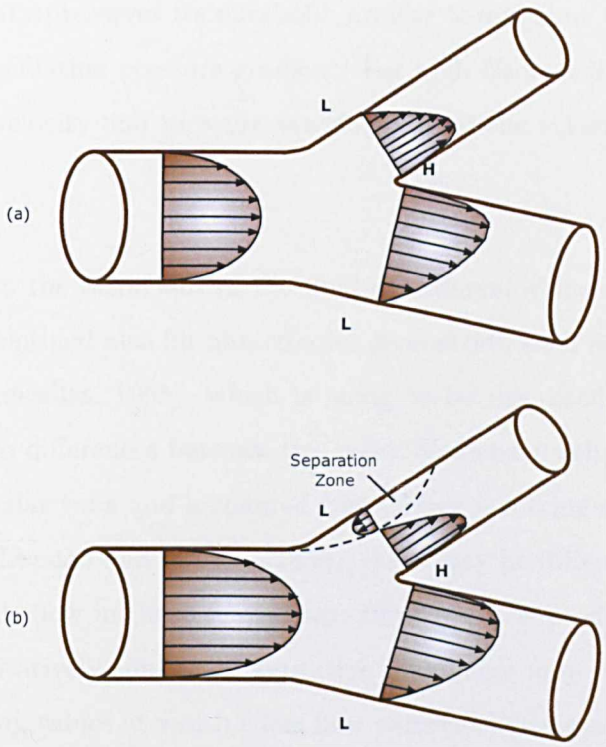

Figure 1.5: Steady flow in a bifurcation (a) without separation, (b) with the formation of a separation zone (Reproduced after Caro et al., 1985). High shear (H) is developed on the flow divider, whereas low shear (L) appears on the outer walls.

1.2.3.2 Unsteady flow

Due to the contractions of the heart, blood flow in arteries is highly pulsatile. Flow waveforms can be, therefore, very complex to analyse, also due to peripheral wave reflections, local instabilities, and other disturbances (Parker, 1977). Some understanding is gained through more simple unsteady cases such as that of a sinusoidally periodic pressure gradient. The dimensionless parameter which is usually used to describe unsteady flows is the Womersley number, denoted as α (or Wo), defined by Womersley (1955) for flow in a straight pipe:

$$\alpha = \frac{D}{2}\sqrt{\frac{\omega}{\nu}} \tag{1.3}$$

where ω $(= 2\pi/T)$ is the frequency of the oscillation and ν $(= \mu/\rho)$ is the kinematic viscosity. The Womersley number is essentially a frequency parameter which characterises the unsteady flow. For low frequencies, the flow is considered *quasi-steady*;

that is, the velocity preserves its parabolic profiles throughout the cycle and is in phase with the oscillating pressure gradient. For high frequencies, there is a phase lag between the velocity and pressure waveforms, and the velocity profiles are not parabolic.

This distinction in the behaviour of the fluid at different values of the Womersley number can be identified also for non-circular geometries, such as that of a channel (Loudon and Tordesillas, 1998), which is going to be discussed in more detail in Chapter 3. Due to differences between the exact Womersley solutions for unsteady flow within a circular tube and a channel (the former involving the use of complex Bessel functions, Landau and Lifshitz, 1959), there may be differences in the development of pulsatile flow in these geometries. However, it is predicted that the flow patterns are qualitatively similar; quantitative differences may be related with the range of Womersley values at which some flow pattern changes occur (as, for example, changes in the frequency and/or the amplitude of the waveform with increasing or decreasing values of α), since the dependence on the parameter is different for each case.

Figure 1.6 shows velocity profiles (non-dimensionalised according to local maximum velocity) at three different Womersley numbers for flow between two parallel plates (After Loudon and Tordesillas, 1998)[12]. For $\alpha < 1$, the velocity and pressure waveforms are in phase and the velocity profiles are parabolic (quasi-steady flow). For $\alpha = 1$, the phase lag between velocity and pressure has already appeared, but the velocity profiles remain in general parabolic. For higher frequencies, the phase lag is well established. The phase lag occurs due to the inability of the faster moving flow (with high inertia) to keep up with the changes in the pressure gradient. As a result, the highest velocities are no longer at the centre; instead, they are closer to the wall. At high frequencies, adjacent fluid particles may end up moving in opposite directions. The Womersley number in the human aorta can take values between 10 and 15 (Caro et al., 1985; Parker and Caro, 1993), implying that the unsteady flow may play a role in the larger arteries.

[12]A more detailed discussion on this is presented in Chapter 3. See also Appendix A.1 for a detailed derivation of the Womersley solution for flow between two parallel plates.

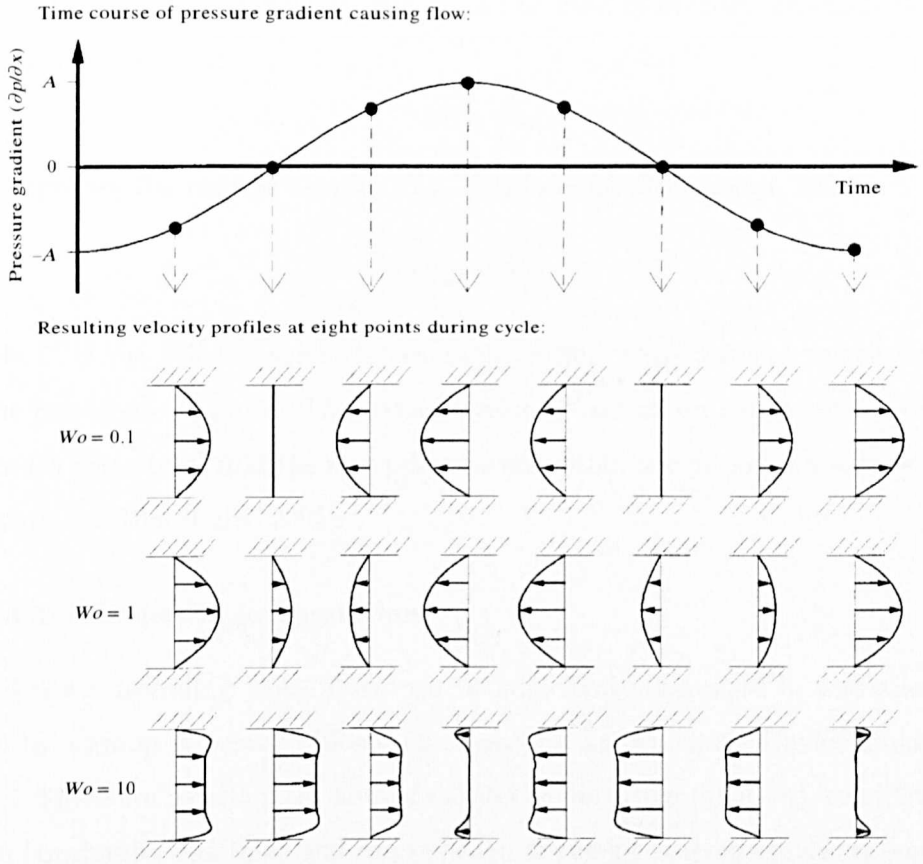

Figure 1.6: Non-dimensional velocity profiles (bottom) when the pressure gradient is oscillating sinusoidally (top). Three different Womersley numbers (α or Wo) are considered for flow between two parallel plates (After Loudon and Tordesillas, 1998).

A sinusoidally oscillating pressure gradient alone has a zero net flow and is clearly not ideal for describing flow in the arteries where blood has to progress distally within the blood vessels. A summation of a steady (mean) and an oscillatory component is often assumed instead[13]. Physiological waveforms vary, depending also on the site of measuring. For further details on features of unsteady flows see Parker (1977); Parker and Caro (1993); Caro et al. (1985); Pedley (1995); Loudon and Tordesillas (1998).

[13]See also relevant discussion in Loudon and Tordesillas (1998).

Two other non-dimensional parameters can be used to describe unsteady flows, the Strouhal number, St:

$$St = \frac{D}{UT} \tag{1.4}$$

or its inverse, the *reduced velocity*, U_{red} (Sherwin and Blackburn, 2005):

$$U_{red} = \frac{UT}{D} \tag{1.5}$$

where U is the velocity scale (for example, mean cross-sectional velocity), and T is the period of the pulse. The reduced velocity parameter can be seen as the distance (in diameters) that the mean flow covers within one period (axial information; Sherwin and Blackburn, 2005).

1.2.3.3 Navier-Stokes equations

Fluid flows, including blood flow, can be sufficiently described in a mathematical form by a group of partial differential equations, known as the Navier-Stokes equations. These are based on the laws of motion (*momentum equation*), conservation of mass (*continuity equation*) and conservation of energy (*energy equation*), and apply to most of the common fluids.

The Navier-Stokes equations can be written in conservation form using vector notation as (Sherwin and Mathews, 2004):

$$\frac{\partial}{\partial t}\mathbf{U} + \frac{\partial}{\partial x}\mathbf{F}_x + \frac{\partial}{\partial y}\mathbf{F}_y + \frac{\partial}{\partial z}\mathbf{F}_z = \frac{\partial}{\partial x}\mathbf{G}_x + \frac{\partial}{\partial y}\mathbf{G}_y + \frac{\partial}{\partial z}\mathbf{G}_z \tag{1.6}$$

where the vectors of unknowns and the inviscid fluxes are described as:

$$\mathbf{U} = \begin{bmatrix} \rho \\ \rho u \\ \rho v \\ \rho w \\ \rho E \end{bmatrix}, \quad \mathbf{F}_x = \begin{bmatrix} \rho u \\ \rho u^2 + p \\ \rho uv \\ \rho uw \\ \rho uH \end{bmatrix}, \quad \mathbf{F}_y = \begin{bmatrix} \rho v \\ \rho vu \\ \rho v^2 + p \\ \rho vw \\ \rho vH \end{bmatrix}, \quad \mathbf{F}_z = \begin{bmatrix} \rho w \\ \rho wu \\ \rho wv \\ \rho w^2 + p \\ \rho wH \end{bmatrix}$$

and the viscous fluxes as:

$$\mathbf{G}_x = \begin{bmatrix} 0 \\ \sigma_{xx} \\ \sigma_{xy} \\ \sigma_{xz} \\ (\sigma \cdot \mathbf{u})_x + kTx \end{bmatrix}, \mathbf{G}_y = \begin{bmatrix} 0 \\ \sigma_{yx} \\ \sigma_{yy} \\ \sigma_{yz} \\ (\sigma \cdot \mathbf{u})_y + kTy \end{bmatrix}, \mathbf{G}_z = \begin{bmatrix} 0 \\ \sigma_{zx} \\ \sigma_{zy} \\ \sigma_{zz} \\ (\sigma \cdot \mathbf{u})_z + kTz \end{bmatrix}$$

where:

$$\begin{aligned} (\sigma \cdot \mathbf{u})_x &= u\sigma_{xx} + v\sigma_{xy} + w\sigma_{xz} \\ (\sigma \cdot \mathbf{u})_y &= u\sigma_{yx} + v\sigma_{yy} + w\sigma_{yz} \\ (\sigma \cdot \mathbf{u})_z &= u\sigma_{zx} + v\sigma_{zy} + w\sigma_{zz} \end{aligned}$$

and u=$[u,v,w]^T$, $\rho = \rho(T)$. k is the coefficient of thermal conductivity. The viscous stress tensor σ is written as:

$$\sigma_{ij} = \mu \left[\left(\frac{\partial u_i}{\partial x_j} + \frac{\partial u_j}{\partial x_i} \right) - \frac{2}{3} \delta_{ij} (\nabla \cdot \mathbf{u}) \right]$$

where u_i is the velocity in the i^{th} direction, x_j is the j^{th} direction co-ordinate and δ_{ij} is the Kronecker delta (δ_{ij}=1, if $i = j$, and δ_{ij}=0, if $i \neq j$), $\mu = \mu(T)$.

The Navier-Stokes equations of Equation 1.6 are non-linear and coupled, and therefore too complicated to solve. For an incompressible and Newtonian fluid of (constant) density ρ and dynamic viscosity μ, the Navier-Stokes equations can be expressed as:

$$\rho \frac{\partial \mathbf{u}}{\partial t} + \rho(\mathbf{u} \cdot \nabla)\mathbf{u} = -\nabla \mathbf{p} + \mu \nabla^2 \mathbf{u}; \tag{1.7}$$

$$\nabla \cdot \mathbf{u} = \mathbf{0}$$

where $\mathbf{u}$=$[u, v, w]$ is the velocity vector and p the pressure.

1.3 Motivation, objectives and general approach

Motivated by the aforementioned considerations, this thesis investigates flow patterns and wall shear stress distributions near branch ostia of (i) the descending

thoracic aorta (in Chapter 3) and (ii) the aortic arch (in Chapter 4). In the investigation of flow around aortic branches of the thoracic aorta, this study attempts to address for the first time age- and species-related changes in the wall shear stress distribution, and hence to find correlations between flow patterns and locations of atherosclerotic lesions. In the investigation of flow within the aortic arch and its major branches, this work aims to establish the flow characteristics and distribution of wall shear stress in the aortic arch of the mouse, to draw a comparison with the human case, and to find correlations with in vivo lesions.

1.3.1 Flow near side branches in the descending thoracic aorta

This project is particularly motivated by the observation that atherosclerotic lesion patterns vary with species and/or age near intercostal ostia in human, rabbit and mouse aortas—as described in Section 1.2.2 (Figure 1.7). A downstream triangular pattern has been observed in children and immature rabbits; a lateral and an upstream streak pattern has been seen in young and older adults, respectively. The former has also been seen in mature rabbits. Finally, a pattern completely surrounding the origin of the intercostal artery has been identified in elderly people and mice of all ages (reviewed by Weinberg, 2002).

Flow near an orifice on a wall, which has potential application to mouths of side branches such as intercostal ostia, has been previously studied mathematically by Sobey (1977a,b); Pedley (1980) and Tutty (1988) in steady flow, and by Tuck (1970) and DeMestre and Guiney (1971) in unsteady flow[14]. However, these studies were limited to relatively low Reynolds numbers and simplified flow conditions.

Our main hypothesis is that the change of lesion patterns with age and species may reflect differences in the distribution of wall shear stress (WSS) around intercostal ostia. Our main objective is to test this hypothesis and attempt to find correlations with in vivo observed lesion maps. The approach we adopt is to investigate, with the use of computational fluid dynamic methods, the effects of haemodynamic, geometric and other factors on shear stress patterns on the aortic wall around the origins of side branches, for such factors can vary in an age- and species-related way. In doing

[14]See Chapter 3 for a detailed review of prior studies related to this project.

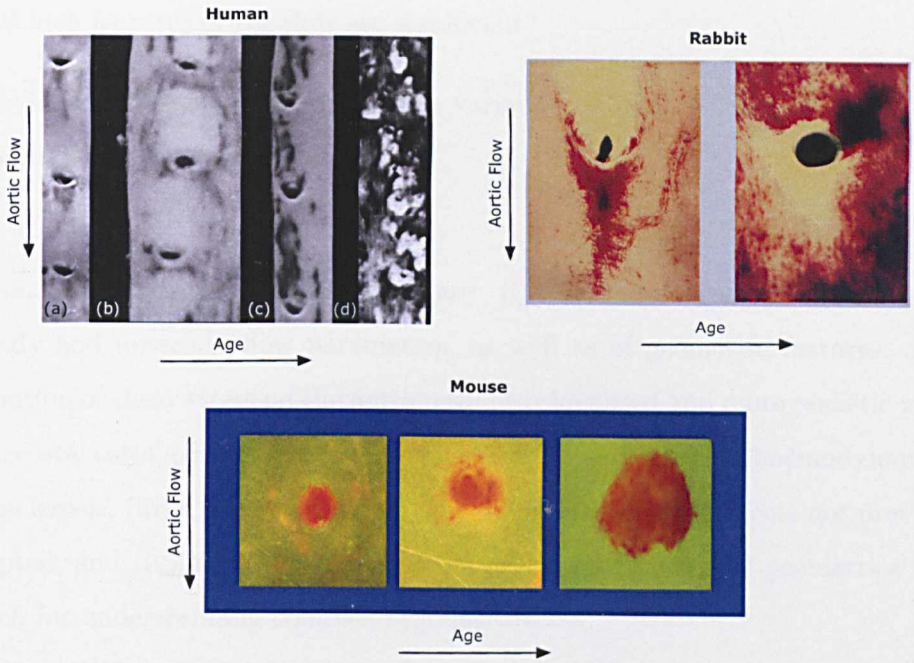

Figure 1.7: Observed atherosclerotic lesions around intercostal ostia in humans [(a) Schroter, R. C., unpublished data from an anorexic young woman, (b-c) Sloop et al. (1998), (d) Mitchell and Schwartz (1965)], rabbits (Barnes and Weinberg, 1999), and mice (McGillicuddy et al., 2001), and their variation with age.

so, we adopt an approach[15] in which the simplest possible geometry representing a side branch is taken at first; additional conditions are included later to increase the complexity of the model and represent more accurately the physiology in vivo. This approach has significant advantages: (i) it allows examination and quantification of haemodynamic, geometric and other features that are difficult to measure in vivo, (ii) it enables identification of individual mechanisms and their influence on the wall shear stress, and (iii) it gives an insight into the use of more generalised (*reduced model*) arterial geometries versus subject-specific vessel geometries.

This project attempts to address the following specific questions:

- Can flow and WSS patterns explain atherosclerotic lesion patterns seen in human, rabbit and mouse aortas?

[15]Often referred to as a *reverse engineering* approach.

- Which features of the flow are significant?
- Which mechanisms can explain the variation of lesion patterns between different species and/or ages?

The main contributions of this project are: (i) a systematic analysis of the effects of steady and unsteady flow parameters, as well as of geometric features, on the distribution of shear stress on the aortic wall near idealised and more realistic models of intercostal ostia, (ii) an understanding of the underlying role of haemodynamics in atherosclerosis, (iii) a consideration of age- and species-related effects not previously attempted, and (iv) an appreciation of the use of *reduced* model geometries in the research for understanding complex systems.

1.3.2 Wall shear stress in the aortic arch

During the past few years there has been an increased interest in the use of the mouse as a model for studying atherosclerosis. The apolipoprotein E-deficient mouse has shown several types of lesions throughout the arterial tree that share many of the features seen in human plaques (Nakashima et al., 1994, see Figure 1.2) and have contributed to identifying the processes involved in atherogenesis. More recently, Johnson and Jackson (2001) have documented the development of advanced atherosclerotic plaques and their susceptibility to rupture in apolipoprotein E knockout (apoE-/-) mice; the ruptures occur predominantly in the brachiocephalic (innominate) artery (BCA)—the first major branch of the aortic arch[16]. Numerous studies have since attempted to characterise such advanced plaques (McAteer et al., 2004; Won et al., 2007). Won et al. (2007) has shown that in lipoprotein receptor-deficient (ldlr-/-) mice lesions occur at the outer wall of the brachiocephalic artery, as well as at the inner (lesser) curvature of the aortic arch.

The success of the mouse as a model of atherosclerosis has also sparked investigation of the haemodynamics within the mouse aortic arch (Suo et al., 2007; Feintuch et al., 2007). However, flow within the human aortic arch has long been studied (Farthing,

[16]The brachiocephalic (innominate) artery is quickly divided into the right common carotid artery (RCCA) and the right subclavian artery (RSCA).

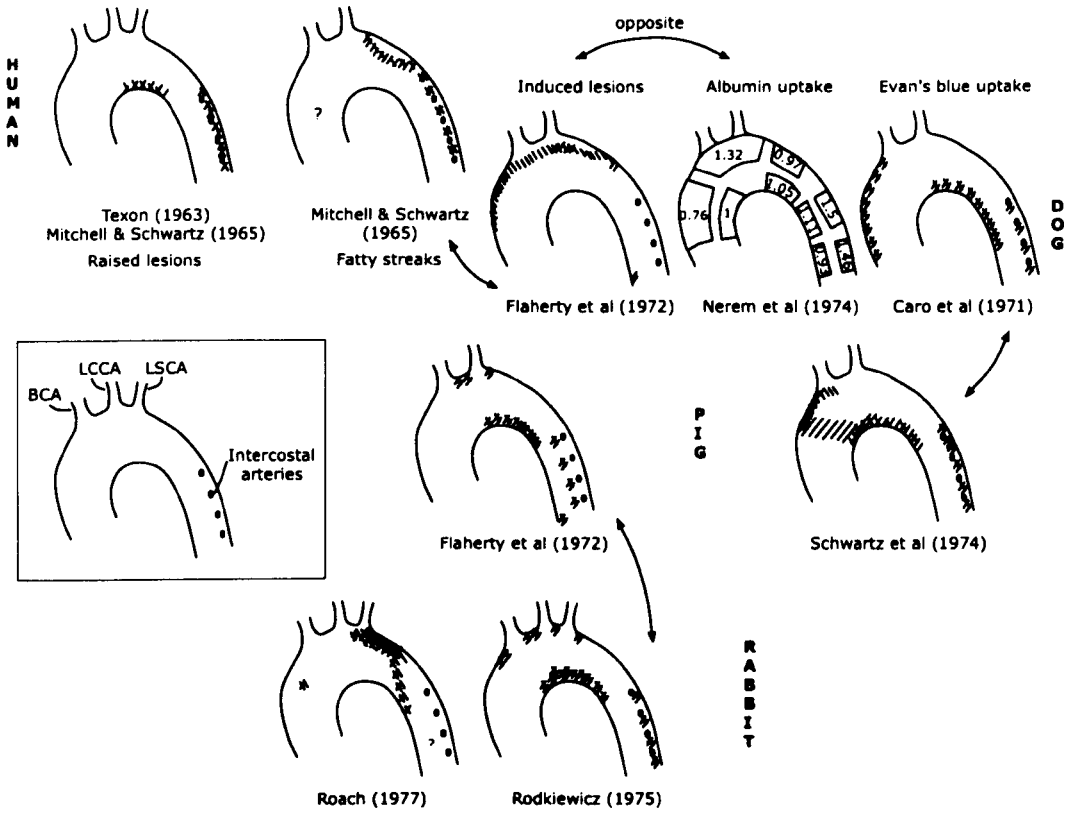

Figure 1.8: Summary of observed atherosclerotic lesion sites in the arch and thoracic aorta of humans, dogs, pigs and rabbits (Reproduced after Farthing, 1978). Arrows imply similar patterns. Inlet was added to show the names of the branches: brachiocephalic artery (BCA), left common carotid artery (LCCA), left subclavian artery (LSCA), and intercostal arteries, which in humans, mice and rabbits are found in pairs.

1978; Shahcheraghi et al., 2002; Jin et al., 2003) and has shown several different distributions. Farthing (1978) has collected past observations of lesions within the arch and thoracic aorta of humans, dogs, pigs and rabbits that show some discrepancies (Figure 1.8, Reproduced after Farthing, 1978). Hence, the haemodynamic environment of the aortic arch is still not well established.

Our main objective is to establish the wall shear stress distribution, and the flow characteristics, within the aortic arch of the wild-type mouse and compare them with those in humans. The Womersley and mean Reynolds numbers for each of these two species are $\alpha \approx 2$ and $Re \approx 100$ for the mouse (the typical heart rate in the mouse is

approximately 450 beats/min, Hartley et al., 2000), and $\alpha \approx 17$ and $Re \approx 1500$ for the human (Suo et al., 2007; Feintuch et al., 2007). Computational models based on magnetic resonance (MR) images are used. Three geometries of different wild-type mice are obtained from MRI datasets (one imaged ex vivo and two in vivo) in an attempt to find flow features that are common in the mouse anatomy, independently of the individual geometries. Furthermore, two approximated human geometries are used to allow comparison with the mouse results.

This project attempts to address the following specific questions:

- What values does the wall shear stress take at the outer wall of the brachiocephalic artery (in relation to the known location of advanced lesions in apoE-/- mice)?
- What is the distribution of wall shear stress at the inner (lesser) curvature of the aortic arch?
- What values does the shear stress take on the walls near the branch flow dividers?
- How is the flow developed within the aortic arch and at the entrance to the descending aorta?
- Does the detailed anatomy play a significant role?

The main contributions of this project are: (i) an analysis of the haemodynamic environment of the mouse aortic arch and major branches in relation to known localisation of atherosclerotic lesions, and (ii) a correlation with the human case.

1.4 Publications

Parts of the results presented in Chapter 3 have been published in the Journal of the Royal Society Interface (Kazakidi et al., 2008, published online before it appears in a printed issue). In addition, two conference abstracts have been published in the Journal of Biomechanics (Kazakidi et al., 2006) and in Heart Online (Kazakidi

et al., 2007) concerning work of Chapter 3. During the course of this thesis, a conference paper was accepted in the 16th Annual Conference of the CFD Society of Canada, Saskatoon, Saskatchewan, Canada, 9-11 June, 2008 (Sherwin et al., 2008). Posters with results of Chapter 3 and Chapter 4 were presented in five Physiological Flow Network meetings, two Hounsfield memorial lectures, two Cardiovascular Technology Network symposiums, the 5th World Congress of Biomechanics, the BSCR & BAS joint 2006 Autumn Meeting and the Bioengineering 08 conference. Oral presentations were given at the Departments of Aeronautics and Bioengineering, IC; the Inaugural International Conference of the Engineering Mechanics Institute (EM08) at the University of Minnesota, Minneapolis, USA, 18-21 May 2008; the RAEng UK Focus for Biomedical Engineering Futures Meeting, London, UK, 15-17 September 2008; and the 7th European Fluid Mechanics conference (EUROMECH), Manchester, UK, 14-18 September 2008.

1.5 Synopsis of thesis

In the remainder of the thesis, Chapter 2 introduces the methodologies used, in particular the computational fluid dynamics and modelling methods. Chapter 3 deals with the investigation of flow and wall shear stress around the origins of intercostal arteries in the descending thoracic aorta. The cases of steady and unsteady flows are examined separately, and geometric considerations are taken into account. Chapter 4 discusses wall shear stress results in the aortic arch and its major branches. Three mouse anatomies and two approximated human geometries are examined. This thesis closes with Chapter 5 where some final conclusions are given together with suggestions for further work.

Chapter 2

Methods

This chapter briefly describes the fundamental theories of the methodologies and numerical algorithms used in the present work. The computations described in Chapter 3 were performed with the flow solver *Nεκταr*, a spectral/*hp* element code (open-source). Section 2.1 introduces, therefore, the mathematical formulation of spectral/*hp* element methods. The *Nεκταr* code utilises three-dimensional unstructured hybrid meshes obtained with a mesh generation technique which is described in Section 2.2. Chapter 4 presents anatomically correct geometries reconstructed from magnetic resonance imaging (MRI) datasets. The techniques used to perform such reconstructions are outlined in Section 2.3. Most of the computations of Chapter 4 were performed with the commercial flow solver Fluent® 6.3. This is a finite volume solver which implements several numerical solution algorithms. The mathematical formulation of the finite volume methods (FVM) is out of the scope of this thesis and, hence, will not be discussed; instead, the book of Ferziger and Perić (2002) is suggested for reference. Other commercially available packages used for some of the models, such as Amira®—an image segmentation software—and Gambit—a mesh generation software for Fluent®—will also not be discussed in detail.

2.1 Spectral/*hp* element methods

2.1.1 Numerical methods: from finite element to spectral/*hp* element methods

Numerical methods are widely used in finding approximate solutions to partial differential equations (PDE). These involve, in general, subdivision of the solution domain into a finite number of subdomains (*elements*) and discretisation of the equations to be solved on the finite grid of elements. There are numerous formulations and discretisation schemes today. See Ferziger and Perić (2002) for a description of the most commonly used schemes.

In the original variational form of the finite element method the solution of the differential equation is found through a minimisation problem for which the solution is identical to the function that minimises a certain functional (Norrie and De Vries, 1978). In the Rayleigh-Ritz approach the solution is approximated with a finite series of functions for which the unknown coefficients are solved in the (*global*) solution domain. Standard finite element methods (FEM) require conversion of the partial differential equation into an integral form and a *weak form*, and discretisation of the approximate solution with a linear combination of basis functions (*expansion basis*). These functions are usually piecewise linear and are defined *locally* in each subdomain. Spectral element methods (SEM), on the other hand, use a finite set of high-order polynomial bases to approximate the solution. This is not to be confused with the spectral methods (SM) which include instead representation of the solution *globally* in the solution domain. There are two main approaches for the implementation of spectral methods: the collocation and the Galerkin formulations.

Spectral/*hp* element methods lie somewhere among the aforementioned standard numerical schemes by utilising the Galerkin formulation and sharing properties from both the finite element and spectral methods: "A spectral/*hp* element method is either a high-order finite element method or a multi-domain spectral method" (Eskillson and Sherwin, 2005). Their advantage is associated with the accuracy of the solution, the type of convergence of the approximate solution to the exact solution, stability errors, cost of computational work and other.

In the finite element methods the error in the numerical solution is reduced by increasing the number of elements in the mesh, while keeping the same expansion basis for the representation of the approximate solution. If h is the characteristic size of the elements in the mesh, convergence is reached by reducing h (that is, as $h \rightarrow 0$). This type of convergence is known as *h-type refinement*, which helps capture complex geometries. In polynomial spectral elements, convergence is achieved by increasing the order p of the polynomial in the expansion basis (that is, as $p \rightarrow \infty$), while the domain is the global solution domain. This is the *p-type refinement* in achieving convergence. While in the h-refinement the solution error decreases by a fixed factor, in the p-refinement the convergence is exponential when the solution is sufficiently smooth; implying a much faster solution (rapid decrease of the solution error) which significantly reduces the computational cost and greatly enhances the accuracy. Therefore, for smooth solutions the p-type refinement is advantageous over the h-type refinement.

The ideal situation is that in which both types of refinement take place. This is known as the *hp refinement*. Hence, for smooth solutions *hp* refinement takes advantage of both the flexibility of the finite element methods in capturing complex geometries and the high accuracy of the polynomial spectral methods. Convergence is reached by both decreasing the size of elements in the mesh (as $h \rightarrow 0$) and increasing the polynomial order of the expansion (as $p \rightarrow \infty$).

Hp-finite element methods (*hp*-FEM) make use of *modal* (or *hierarchical*) expansion bases, that is, the expansion of order P contains all the lower-order (less than P) expansions and the unknown coefficients have no physical meaning. Spectral element methods (SEM), on the other hand, use *nodal* (*non-hierarchical*) expansion bases in which the approximate solution is evaluated at a set of pre-defined points (or *nodes*). Hence, the unknown coefficients have a physical meaning and correspond to the values of the function at the nodes of the element (*nodal values*). The general Galerkin formulation is the same for both *hp*-FEM and SEM, despite the differences in their implementation. Spectral/*hp* element methods are more general and include both techniques, using either *modal* or *nodal* polynomial expansions.

In the following sections, we follow Karniadakis and Sherwin (2005) to describe the basic formulation of the spectral/*hp* element methods (first introduced in Sherwin and Karniadakis, 1996). We start with the Galerkin formulation in Sections 2.1.2 and 2.1.3 and we continue with the expansion bases in one and multiple dimensions in Section 2.1.4. The basic elemental operations for the implementation of spectral/*hp* element methods are described in Section 2.1.5. Finally, Section 2.1.6 presents the spectral/*hp* approach for solving the incompressible Navier-Stokes equations.

2.1.2 Method of weighted residuals

The standard Galerkin formulation is based on an older approximation technique, the method of weighted residuals (MWR), in which the *weighted residual* (*error*) between the exact and the approximate solution is required to be zero. First, let us define the $\mathbf{L}^2(\Omega)$ inner product (*Legendre inner product*) as:

$$(f,g) = \int_{\Omega} f(\mathbf{x})g(\mathbf{x})\mathrm{d}\mathbf{x} \tag{2.1}$$

where $f(\mathbf{x}), g(\mathbf{x})$ are functions defined in the domain Ω.

We consider a linear differential operator D, defined in a domain Ω, which acts on a function u and produces a function f while the equation is constrained by suitable boundary conditions:

$$D(u(\mathbf{x},t)) = f(\mathbf{x},t) \tag{2.2}$$

We approximate the solution $u(\mathbf{x},t)$ by a function $u^{\delta}(\mathbf{x},t)$ such that:

$$u(\mathbf{x},t) \approx u^{\delta}(\mathbf{x},t) = u_o(\mathbf{x},t) + \sum_{i=1}^{N_{dof}} \hat{u}_i(t)\Phi_i(\mathbf{x}) \tag{2.3}$$

The function $u^{\delta}(\mathbf{x},t)$ is a linear combination of basis functions, where $\Phi_i(\mathbf{x})$ are analytic functions (*trial* or *expansion functions*), $\hat{u}_i(t)$ are unknown coefficients (N_{dof}), and $u_o(\mathbf{x},t)$ is a function satisfying the initial and boundary conditions. Substitution of the approximation u^{δ} of Equation (2.3) into the differential operator D of Equation (2.2) results in a solution that, in general, is not equal to $f(\mathbf{x},t)$. The *error* or *residual* R between the approximate and the exact solution is then:

$$R(u^{\delta}) = D(u^{\delta}) - f \neq 0 \tag{2.4}$$

The unknown coefficients $\hat{u}_i(t)$ are determined according to the method of weighted residuals, which requires that the Legendre inner product of the residual R and a *test* or *weight* function $v_j(\mathbf{x})$ be zero over the domain:

$$(v_j(\mathbf{x}), R) = \int_\Omega v_j R(u^\delta) \mathrm{d}\mathbf{x} = 0, \qquad j = 1, ..., N_{dof} \tag{2.5}$$

The choice of the test (*weight*) function v_j, together with the choice of the expansion (*trial*) functions $\Phi_i(\mathbf{x})$ that describe the approximate solution, determines the different numerical methods; including the *collocation*, *finite volume/subdomain*, *least-squares*, and *Galerkin* methods. In the latter formulation, the weight functions are taken to be the same as the trial functions: $v_j(\mathbf{x}) = \Phi_j$ (Bubnov-Galerkin method). In the more generalised form of the Galerkin method (the Petrov-Galerkin method), the test functions v_j are taken to be similar to the trial functions $\Phi_i(\mathbf{x})$, but not identical: $v_j(\mathbf{x}) \neq \Phi_j$[1].

2.1.3 Galerkin formulation

2.1.3.1 Basic concepts

A descriptive introduction to some fundamental concepts of the Galerkin formulation is presented here by considering the one-dimensional Helmholtz equation. The Galerkin problem can then formulate in three steps:

- Problem definition

Suppose the one-dimensional Helmholtz equation:

$$D(u) = \frac{\partial^2 u}{\partial x^2} - \lambda u = f \tag{2.6}$$

where λ is a real positive constant. If the solution is considered in a domain $\Omega = \{x | 0 < x < 1\}$, then the following boundary conditions can be chosen:

$$u(0) = g_D, \qquad \frac{\partial u}{\partial x}(1) = g_N \tag{2.7}$$

where g_D and g_N are constants. The former condition is the *Dirichlet* (or *essential*) boundary condition applied on the solution, whereas the latter condition constraints the derivative of the solution and is known as the *Neumann* (or *natural*) boundary condition.

[1] For more details on the methods of weighted residuals see references in Karniadakis and Sherwin (2005).

- Weak form and the Neumann boundary conditions

To construct the Galerkin problem, we write Equation (2.6) in its integral and *weak* forms. Following the method of weighted residuals, this is achieved by multiplying Equation (2.6) by an arbitrary test (weight) function $v(x)$, which is zero on all Dirichlet boundaries, and integrating over the domain Ω (*integral form*):

$$(v, D(u)) = \int_0^1 v\frac{\partial^2 u}{\partial x^2}\mathrm{d}x - \int_0^1 \lambda v u \mathrm{d}x = \int_0^1 v f \mathrm{d}x \tag{2.8}$$

Integrating Equation (2.8) by parts, produces the *weak form*:

$$\int_0^1 \frac{\partial v}{\partial x}\frac{\partial u}{\partial x}\mathrm{d}x + \int_0^1 \lambda v u \mathrm{d}x + \int_0^1 v f \mathrm{d}x = \left[v\frac{\partial u}{\partial x}\right]_0^1 \tag{2.9}$$

According to the Galerkin approximation, the solution to the original problem of Equation (2.6) is the solution to the *weak* form of the problem of Equation (2.9) when the solution $u(x)$ is approximated by a discrete function $u^\delta(x)$. The function $v(x)$ is also approximated by a finite function, $v^\delta(x)$. By definition, $v(0) = 0$, and by imposing the Neumman boundary condition $[\partial u(1)/\partial x = g_N]$, Equation (2.9) becomes[2]:

$$\int_0^1 \frac{\partial v^\delta}{\partial x}\frac{\partial u^\delta}{\partial x}\mathrm{d}x + \int_0^1 \lambda v^\delta u^\delta \mathrm{d}x + \int_0^1 v^\delta f \mathrm{d}x = v^\delta(1) g_N \tag{2.10}$$

- Dirichlet boundary conditions (*lifting*)

To include the Dirichlet boundary conditions in the formulation, we express the approximate solution, u^δ, as the sum of a known, u^D, and an unknown, u^H, function:

$$u^\delta = u^D + u^H \tag{2.11}$$

The known (*lifted*) function u^D is defined on the Dirichlet boundaries and satisfies the Dirichlet condition: $u^D(\partial\Omega_D) = g_D$. The unknown function u^H is a homogeneous function defined in the interior of the solution domain; it has, therefore, a zero value on the Dirichlet boundaries: $u^H(\partial\Omega_D) = 0$. This process is known as *lifting of*

[2]Equation (2.10) shows that the Neumann boundary conditions are incorporated automatically (naturally) in the Galerkin formulation.

a known solution and is important because it reduces the complexity of the problem by limiting the approximate solution within the interior of the solution domain.

Inserting Equation (2.11) into Equation (2.10) and arranging the terms into unknown (left-hand-side) and known (right-hand-side) leads to:

$$\int_0^1 \frac{\partial v^\delta}{\partial x}\frac{\partial u^H}{\partial x}\mathrm{d}x + \int_0^1 \lambda v^\delta u^H \mathrm{d}x = v^\delta(1)g_N - \int_0^1 v^\delta f \mathrm{d}x - \int_0^1 \lambda v^\delta u^D \mathrm{d}x - \int_0^1 \frac{\partial v^\delta}{\partial x}\frac{\partial u^D}{\partial x}\mathrm{d}x \tag{2.12}$$

Since both the homogeneous solution, u^H, and the test function, v^δ, are finite expansions and the right-hand-side terms are known, Equation (2.12) is a finite-dimension linear algebraic system which can be solved in a matrix form.

Another important property of the *lifting* process is that the homogeneous solution can have the same expansion space as the test function since both are zero on the Dirichlet boundaries[3]. This allows for the Galerkin[4] spectral/*hp* method to be applied by choosing the expansion basis of the homogenous solution, u^H, to be the same as the expansion basis of the test function, v^δ.

2.1.3.2 Matrix form

The approximation of the solution u^δ, as defined by Equation (2.3), and the test function, v^δ, can be expressed in matrix form as:

$$u^\delta(\mathbf{x_j}, t) = \sum_{i=1}^{N_{dof}} \hat{u}_i(t)\Phi_i(\mathbf{x_j}) = \mathbf{\Phi}^T\hat{\mathbf{u}} \tag{2.13}$$

$$v^\delta(\mathbf{x_j}, t) = \sum_{i=1}^{N_{dof}} \hat{v}_i(t)\Phi_i(\mathbf{x_j}) = \mathbf{\Phi}^T\hat{\mathbf{v}} \tag{2.14}$$

where both contain the same expansion basis $\Phi_i(x_j)$ and $\hat{\mathbf{u}}[\mathbf{i}] = \hat{u}_i$, $\hat{\mathbf{v}}[\mathbf{i}] = \hat{v}_i$, $\mathbf{\Phi}[\mathbf{i},\mathbf{j}] = \Phi_i(x_j)$. Equation (2.12) can then be written in a matrix form:

$$\mathcal{B}\hat{\mathbf{u}}^H = \mathbf{f} \tag{2.15}$$

[3]See Karniadakis and Sherwin (2005) for a full discussion on the *lifting* process.

[4]For more details on the properties of the Galerkin approximation see Karniadakis and Sherwin (2005).

where $\hat{\mathbf{u}}^H$ is a vector of the unknown coefficients of the homogeneous expansion basis, $\mathcal{B}$ is a constant matrix with components resulting from the inner products of the homogeneous expansion functions and their derivatives, and $\mathbf{f}$ is a vector including the force function and the Dirchlet and Neumann boundary conditions.

If the domain Ω in the above formulation is divided into more elements, N_{el} (h-refinement), the (*global*) matrix $\mathcal{B}$ can be subdivided into $\mathcal{B}^e$ (*elemental*) submatrices, each associated with one element and the *local* expansion functions. However, there are more *local* degrees of freedom than *global* degrees of freedom due to the requirement that the global expansion be C^o continuous, as we shall demonstrate in Section 2.1.4.1.

2.1.4 Expansion bases

2.1.4.1 Standard element

A fundamental concept in the spectral/*hp* element methods, which simplifies their numerical implementation, is the definition of a *standard element* within which standard *local expansion bases* can be defined. The global expansion bases are then *assembled* from these local bases as it will be shown in the following.

Suppose a solution domain $\Omega = \{x \mid 0 < x < l\}$, which is subdivided into N_{el} finite non-overlapping elements, Ω^e [5]:

$$\Omega^e = \{x \mid x_{e-1} < x < x_e\}, \quad e = 1, 2, .., N_{el} \tag{2.16}$$

We define a *standard element*, Ω_{st}, in terms of a *local* co-ordinate ξ, such that:

$$\Omega_{st} = \{\xi | -1 \leq \xi \leq 1\} \tag{2.17}$$

A local expansion basis, $\phi_i(\xi)$, can now be defined within the standard element Ω_{st}. Via a co-ordinate transformation, $\chi^e(\xi)$, the global co-ordinate x ($x \in \Omega^e$) can be written as a function of the local co-ordinate ξ ($\xi \in \Omega_{st}$). Consequently, the global expansion modes, $\Phi_j(x)$, can be expressed in terms of the local expansion functions.

Suppose the example of a linear finite element decomposition over three non-equal

[5] The union of these finite elements produces exactly the original space Ω.

elements, $N_{el} = 3$ or Ω^1, Ω^2, Ω^3 (middle of Figure 2.1). There are four degrees of freedom in the expansion ($N_{dof} = 4$) and, hence, there are four global expansion modes $\Phi_o(x)$, $\Phi_1(x)$, $\Phi_2(x)$, $\Phi_3(x)$ over the solution domain Ω (top of Figure 2.1). However, in every element the global modes can be constructed by two linearly-varying functions (bottom of Figure 2.1). An appropriate local expansion basis defined within the standard element, Ω_{st}, would be:

$$\phi_o(\xi) = \begin{cases} \frac{1-\xi}{2}, & \xi \in \Omega_{st} \\ 0, & \xi \notin \Omega_{st} \end{cases}, \qquad \phi_1(\xi) = \begin{cases} \frac{1+\xi}{2}, & \xi \in \Omega_{st} \\ 0, & \xi \notin \Omega_{st} \end{cases} \tag{2.18}$$

We can now transform the global co-ordinate x to the local co-ordinate ξ, and vice versa, via the mapping $\chi^e(\xi)$:

$$x = \chi^e(\xi) = \frac{1-\xi}{2} x_{e-1} + \frac{1+\xi}{2} x_e, \quad \xi \in \Omega_{st} \tag{2.19}$$

The finite element approximation, u^δ, which was expressed in terms of the global epxansion modes, $\Phi_i(x)$, can now be written in terms of the local expansion modes, $\phi_p(\xi)$, as:

$$u^\delta(x,t) = \sum_{i=1}^{N_{dof}-1} \hat{u}_i \Phi_i(x) = \sum_{e=1}^{N_{el}} \sum_{p=0}^{P} \hat{u}_p^e \phi_p^e(\xi) \tag{2.20}$$

where P is the polynomial order of the expansion. However, the mapping is not complete without ensuring that the approximate solution u^δ is continuous everywhere in the domain. In the above example, there are six local degrees of freedom [$N_{dof}^e = N_{el}(P+1) = 6$; $P = 1, N_{el} = 3$], but only four global degrees of freedom ($N_{dof} = 4$). Hence, we apply two constraints on the local coefficients to ensure C^o continuity:

$$\begin{aligned} \hat{u}_1^1 &= \hat{u}_0^2 \\ \hat{u}_1^2 &= \hat{u}_0^3 \end{aligned} \tag{2.21}$$

By denoting with $\hat{\mathbf{u}}_\mathbf{g}$ a vector of the global coefficients and $\hat{\mathbf{u}}_\mathbf{l}$ a vector of the local coefficients, then the mapping from local to global bases can be expressed in matrix form as:

$$\hat{\mathbf{u}}_\mathbf{l} = \mathcal{A} \hat{\mathbf{u}}_\mathbf{g} \tag{2.22}$$

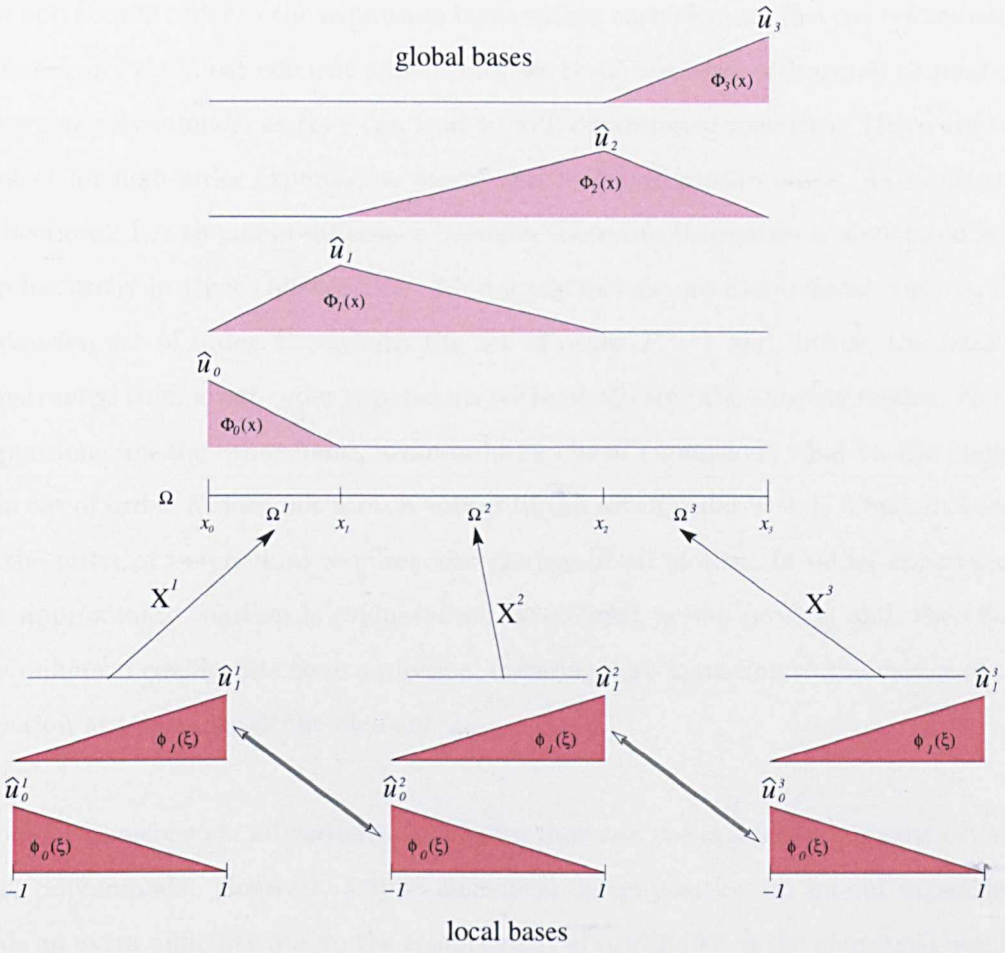

Figure 2.1: Local and global expansion bases and coefficients for a three-element discretisation of the solution domain Ω (After Karniadakis and Sherwin, 2005).

where $\mathcal{A}$ is known as the *assembly matrix*, which is very sparse.

This type of elemental decomposition and further partitioning of the solution (h-type refinement) is advantageous for resolving efficiently arbitrarily complex geometries and flows.

2.1.4.2 One-dimensional expansion bases

Navier-Stokes equations in complex geometries often introduce localised flow structures that are difficult to resolve. An accurate solution can be reached by increasing

the polynomial order of the expansion basis within each element (p-type refinement). Numerically the most efficient expansions are those that use orthogonal or near orthogonal polynomials, as they can lead to well-conditioned matrices. There are two choices for high-order expansions, *modal* and *nodal* expansion bases. As mentioned in Section 2.1.1, the main difference between these two categories is associated with the hierarchy in their construction. Modal expansions are hierarchical, that is, the expansion set of order P contains the set of order $P-1$ and, hence, the basis is constructed from lower-order expansions without altering the existing modes. Nodal expansions, on the other hand, are non-hierarchical expansions, that is, the expansion set of order P does not form a subset in the set of order $P+1$. Thus, a change in the order of polynomial requires also change of all modes. In nodal expansions, the approximate solution is evaluated at pre-defined points (nodes) and, therefore, the unknown coefficients have a physical meaning corresponding to the values of the function at the nodes of the element.

Modal expansions are advantageous because they can use orthogonal or near orthogonal polynomials. However, h-type elemental decomposition on modal expansions adds an extra difficulty due to the requirement of continuity at the elemental boundaries. This is usually resolved by a *boundary and interior decomposition*, for which the local expansions are chosen such that the modes can be divided into *boundary modes*, which have a magnitude at one of the elemental boundaries and zero value at all other boundaries, and *interior modes*, which are zero on all boundaries and only have a magnitude in the interior of the element.

Modal expansion bases usually make use of the Jacobi polynomials, $P_p^{\alpha,\beta}(x)$, which is a family of solutions to a singular Sturm-Liouville problem. Defined in the region $(-1 < x < 1)$ this is expressed as:

$$\frac{\mathrm{d}}{\mathrm{d}x}\left[(1-x)^{1+\alpha}(1+x)^{1+\beta}\frac{\mathrm{d}}{\mathrm{d}x}P_P^{\alpha,\beta}(x)\right] = \lambda_p(1-x)^{\alpha}(1+x)^{\beta}P_P^{\alpha,\beta}(x) \qquad (2.23)$$

where $\lambda_p = -p(\alpha+\beta+p+1)$, and p is the polynomial order. Jacobi polynomials are orthogonal polynomials:

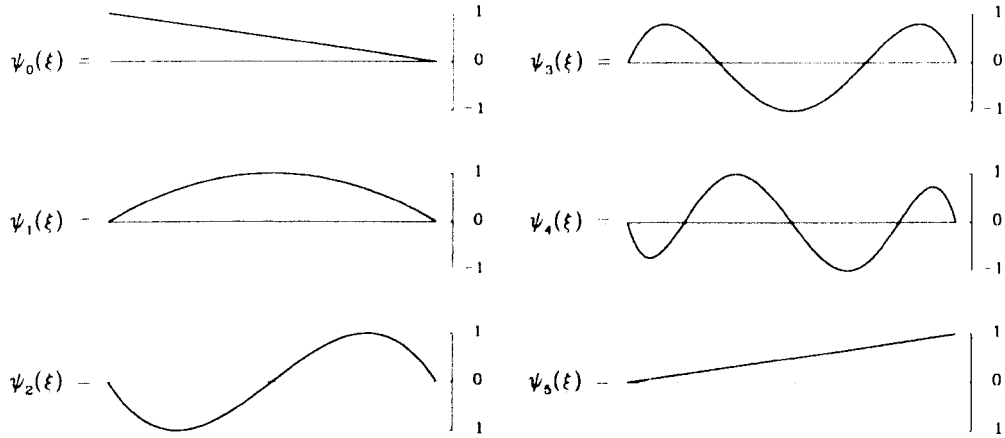

Figure 2.2: Modal expansion modes for polynomial order $P = 5$ (After Karniadakis and Sherwin, 2005).

$$\int_{-1}^{1}(1-x)^{\alpha}(1+x)^{\beta}P_p^{\alpha,\beta}(x)P_q^{\alpha,\beta}(x)\mathrm{d}x = C\delta_{pq} \tag{2.24}$$

where C depends on α, β and p, and δ_{pq} is the Kronecker delta function. According to Equation (2.24), when $P_p^{\alpha,\beta}(x)$ is integrated with respect to $(1-x)^{\alpha}(1+x)^{\beta}$, it is orthogonal to all polynomials of order less than p (Karniadakis and Sherwin, 2005).

Based on the above formulation, we define a p-type modal expansion in the *standard* element, $\Omega_{st} = \{\xi | -1 \leq \xi \leq 1\}$, such that:

$$\phi_p(\xi) \mapsto \psi_p(\xi) = \begin{cases} \dfrac{1-\xi}{2}, & p = 0 \\ \left(\dfrac{1-\xi}{2}\right)\left(\dfrac{1+\xi}{2}\right)P_{p-1}^{1,1}(\xi), & 0 < p < P \\ \dfrac{1+\xi}{2}, & p = P \end{cases} \tag{2.25}$$

where P is the maximum polynomial order, and $\psi(\xi)$ is used to denote the specific polynomial basis. Figure 2.2 displays the shape of the modes for a polynomial order of $P = 5$, normalised to a maximum value of one. The modes for $p = 0$ and

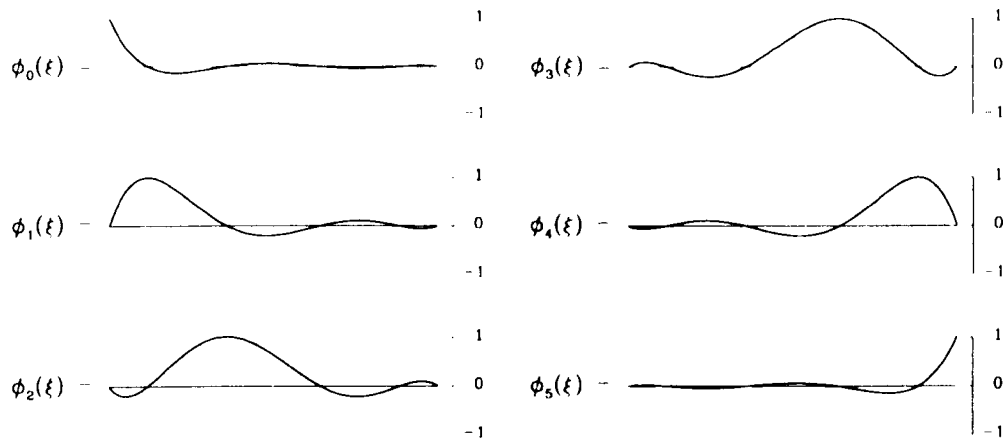

Figure 2.3: Nodal expansion modes for polynomial order $P = 5$ (After Karniadakis and Sherwin, 2005).

$p = P$ are the boundary modes, whereas the others are the interior modes. The Jacobi polynomial $P^{1,1}_{p-1}(\xi)$ preserves significantly its orthogonality and results in an elemental mass matrix which is largely penta-diagonal.

Likewise, a nodal expansion in the standard element Ω_{st} is defined as:

$$\phi_p(\xi) \mapsto h_p(\xi) = \begin{cases} 1, & \xi = \xi_p \\ \dfrac{(\xi-1)(\xi+1)L'_P(\xi)}{P(P+1)L_P(\xi_p)(\xi_p-\xi)}, & \xi \neq \xi_p \end{cases} \qquad 0 \leq p \leq P \quad (2.26)$$

where $L_P(\xi)$ is the Legendre polynomial, the derivative of which can be linked to the Jacobi polynomial $P^{1,1}_{P-1}(\xi)$ (Karniadakis and Sherwin, 2005). Figure 2.3 shows the shapes of the nodal modes for $P = 5$, normalised to a maximum value of one. All modes are of the same order P and can be distinguished into boundary and interior modes[6].

2.1.4.3 Multi-dimensional expansion bases

Equivalent to the one-dimenional expansion bases, we can define a standard element, Ω_{st}, in the two- and three-dimensional regions ($\mathcal{Q}^2, \mathcal{Q}^3$), as the bi-unit square and

[6]For further details on the expansion bases see Karniadakis and Sherwin (2005).

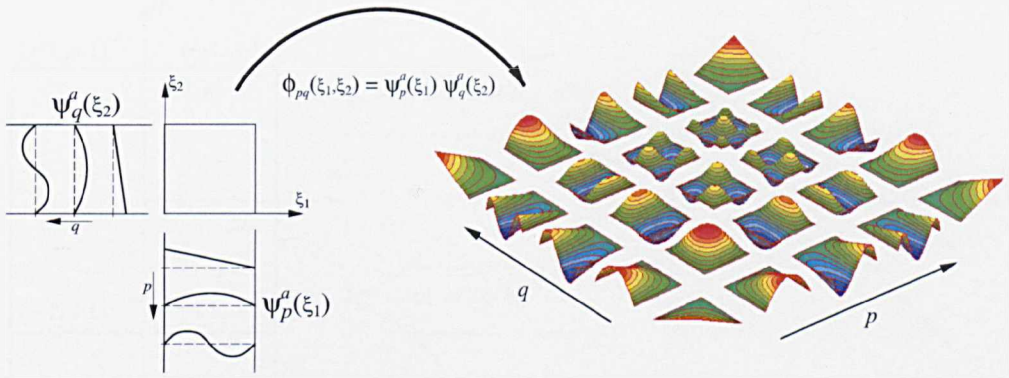

Figure 2.4: Two-dimensional expansion basis constructed from two one-dimensional modal expansions of polynomial order $P = 4$ (After Karniadakis and Sherwin, 2005).

cuboid, respectively:

$$\begin{aligned} \Omega_{st} = \mathcal{Q}^2 &= \{\xi | -1 \leq \xi_1, \xi_2 \leq 1\} \\ \Omega_{st} = \mathcal{Q}^3 &= \{\xi | -1 \leq \xi_1, \xi_2, \xi_3 \leq 1\} \end{aligned} \tag{2.27}$$

where ξ_i $(i = 1, 2, 3)$ are the local Cartersian co-ordinates. This is the simplest approach applied over *structured* partitioning of the solution domain, that is, the mesh includes quadrilateral (in two dimensions) or hexahedral (in three dimensions) elements. The two- and three-dimensional expansion bases, $\phi_{pq}(\xi_1, \xi_2)$ and $\phi_{pqr}(\xi_1, \xi_2, \xi_3)$ respectively, can then be constructed by the product of one-dimensional bases (*tensors*):

$$\begin{aligned} \phi_{pq}(\xi_1, \xi_2) &= \phi_p(\xi_1)\phi_q(\xi_2), && 0 \leq p, q, \quad p \leq P_1, \; q \leq P_2 \\ \phi_{pqr}(\xi_1, \xi_2, \xi_3) &= \phi_p(\xi_1)\phi_q(\xi_2)\phi_r(\xi_3), && 0 \leq p, q, r, \quad p \leq P_1, \; q \leq P_2, \; r \leq P_3 \end{aligned} \tag{2.28}$$

where P_1, P_2, P_3 may not necessarily be equal. Figure 2.4 illustrates the normalised modes of a two-dimensional expansion of polynomial order $P = 4$, constructed from the product of two one-dimensional modal expansions of order $P_1 = P_2 = 4$. This is the most common *hp*-finite element expansion in a quadrilateral mesh. Nodal (non-hierarchic) expansion bases can be equally used for the construction of a two-dimensional expansion. The *boundary and interior decomposition* introduced for

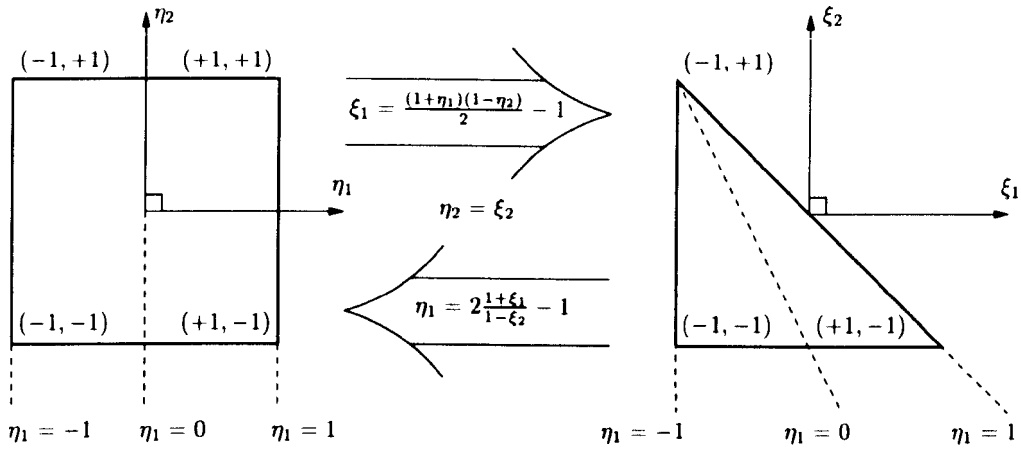

Figure 2.5: Mapping of a quadrilateral element to a triangular element, and vice versa (After Karniadakis and Sherwin, 2005).

one-dimentional expansions can also be applied in multi-dimensional bases dividing the modes into *boundary* (non-zero on the boundaries—*vertex* and *edge* modes) and *interior* modes (zero on the boundaries—*face* modes[7]). This type of decomposition ensures a C^o continuity across the elemental boundaries.

However, standard regions in higher dimensions are not limited to quadrilateral or hexahedral regions (structured meshes). Unstructured meshes are more commonly used and are especially favourable for providing local refinement and solutions in complex geometries. Therefore, the standard regions in two dimensions can be either a triangle or a quadrilateral, whereas in three dimensions Ω_{st} can be a prism, pyramid, tetrahedron or hexahedron (***hybrid*** domains).

To ensure numerical efficiency in the triangular or hybrid expansions equivalent to the efficiency of the quadrilateral or hexahedral expansions at any polynomial order P, it is best to use a tensor product similar to that of Equation (2.28). The main difficulty that arises is in the definition of a triangular or tetrahedral element in the Cartesian co-ordinate system. As seen on the right of Figure 2.5, for a standard triangular element to be described in the Cartesian system, the co-ordinates ξ_1, ξ_2

[7]See Karniadakis and Sherwin (2005) for further details.

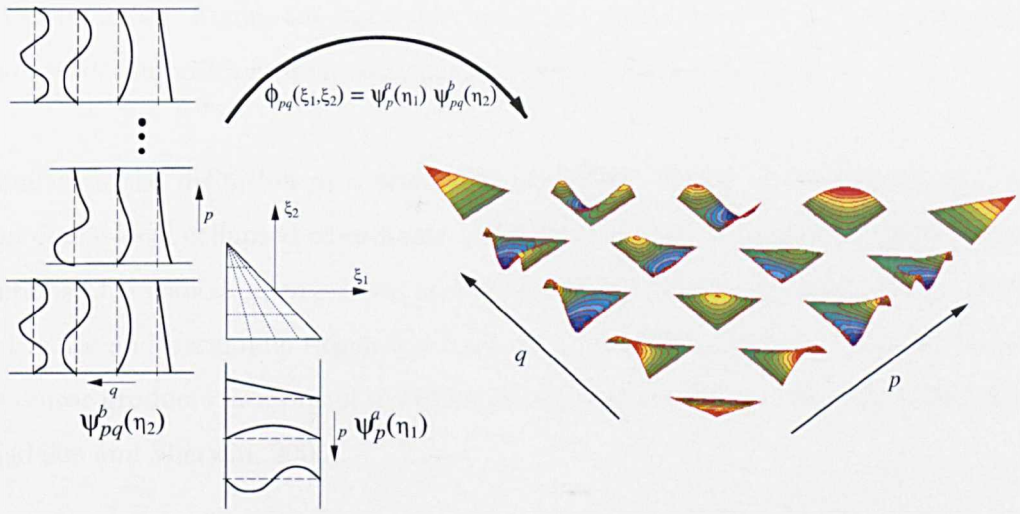

Figure 2.6: Triangular expansion basis in two-dimensions for a polynomial order of $P = 4$ (After Karniadakis and Sherwin, 2005).

have to be dependent on each other: $\mathcal{T}^2 = \{(\xi_1, \xi_2) | -1 \leq \xi_1, \xi_2, \xi_1 + \xi_2 \leq 0\}$. This is resolved by defining a *collapsed co-ordinate system*, in which the local co-ordinates, η_1, η_2, are independent:

$$\mathcal{T}^2 = \{(\eta_1, \eta_2) | -1 \leq \eta_1, \eta_2 \leq 0\} \tag{2.29}$$

The mapping of a triangle to a square, and vice versa, or—in other words—the transformation from the collapsed co-ordinate system to the Cartesian one, and vice versa, is illustrated in Figure 2.5 and is defined as:

$$\begin{aligned} \eta_1 &= 2\frac{(1+\xi_1)}{(1-\xi_2)} - 1 \\ \eta_2 &= \xi_2 \end{aligned} \tag{2.30}$$

A two-dimensional expansion basis for a standard triangular element can then be defined as a tensor product:

$$\psi_{pq}(\xi_1, \xi_2) = \psi^\alpha_p(\eta_1)\psi^\alpha_{pq}(\eta_2) \tag{2.31}$$

where $\psi^\alpha_p(\eta_1)$, $\psi^\alpha_{pq}(\eta_2)$ are a one- and two-dimensional tensors, respectively, known as *modified principal functions* (see definition in Sherwin, 1997; Karniadakis and

Sherwin, 2005). Figure 2.6 shows the expansion modes for $P = 4$. A boundary and interior decomposition of the expansion modes can again be applied.

Similar to the definition of a triangular standard element in two dimensions, we can define local collapsed co-ordinate systems in three dimensions to enable the definitions of tetrahedral, prismatic and pyramidic standard elements. Tethrahedral, prismatic and pyramidic expansion bases in three-dimensions can again be defined as tensor products in terms of modified principal functions (see Sherwin, 1997; Karniadakis and Sherwin, 2005).

2.1.5 Elemental operations

2.1.5.1 Integration

The mathematical operations of integration and differentiation can be numerically performed by using the Gaussian quadrature. In one-dimensional expansions, the numerical integration is approximated as:

$$\int_{-1}^{1} u(\xi)\mathrm{d}\xi \approx \sum_{i=0}^{Q-1} w_i u(\xi_i) \tag{2.32}$$

where w_i are constants (*weights*) and ξ_i $(-1 \leq \xi_i \leq 1)$ is an abscissa of Q quadrature points (*zeros*) at which $u(\xi)$ is evaluated. Gauss quadrature allows for the exact integration of polynomials of order higher than $Q-1$, and has zeros within the region $-1 \leq \xi_i \leq 1$, where $i = 0, ..., Q-1$. The location of the Gauss zero points depend on the quadrature. There are three types: the *Gauss* quadrature, in which the zeros lie in the interior of the interval; the *Gauss-Radau* quadrature, which includes a zero point at one of the boundaries of the element (usually at $\xi = -1$); and the *Gauss-Lobatto* quadrature, which contains both end points of the element ($\xi = \pm 1$).

Similarly, numerical integration in two dimensions, $\mathcal{Q}^2 = \{-1 \leq \xi_1, \xi_2 \leq 1\}$, and three dimensions, $\mathcal{Q}^3 = \{-1 \leq \xi_1, \xi_2, \xi_3 \leq 1\}$, in the standard quadrilateral and hexahedral regions, respectively, are performed as:

$$\int_{Q^2} u(\xi_1,\xi_2)\mathrm{d}\xi_1\mathrm{d}\xi_2 \simeq \sum_{i=0}^{Q_1-1} w_i \left\{ \sum_{j=0}^{Q_2-1} w_j u(\xi_{1i},\xi_{2j}) \right\} \tag{2.33}$$

$$\int_{Q^3} u(\xi_1,\xi_2,\xi_3)\mathrm{d}\xi_1\mathrm{d}\xi_2\mathrm{d}\xi_3 \simeq \sum_{i=0}^{Q_1-1} w_i \left\{ \sum_{j=0}^{Q_2-1} w_j \left\{ \sum_{k=0}^{Q_3-1} w_k u(\xi_{1i},\xi_{2j},\xi_{3k}) \right\} \right\} \tag{2.34}$$

For triangular, tetrahedral, prismatic and pyramidic standard regions, numerical integration is performed in a similar way via an elemental mapping with the use of appropriate *collapsed* co-ordinate systems as defined earlier (see Karniadakis and Sherwin, 2005).

2.1.5.2 Differentiation

The differentiation operation can be numerically performed as follows. Suppose the one-dimensional approximation:

$$u^\delta(x) = \sum_{p=0}^{P} \hat{u}_p \phi_p(\chi(\xi)^{-1}) \tag{2.35}$$

where $\chi(\xi)^{-1}$ is the mapping from local to global regions. The function can be differentiated as:

$$\frac{\mathrm{d}u^\delta(\xi)}{\mathrm{d}x} = \frac{\mathrm{d}u^\delta(\xi)}{\mathrm{d}\xi}\frac{\mathrm{d}\xi}{\mathrm{d}x} = \sum_{p=0}^{P} \hat{u}_p \frac{\mathrm{d}\phi_p(\xi)}{\mathrm{d}\xi}\frac{\mathrm{d}\xi}{\mathrm{d}x} \tag{2.36}$$

where $\frac{\mathrm{d}\phi_p(\xi)}{\mathrm{d}\xi}$ and $\frac{\mathrm{d}\xi}{\mathrm{d}x}$ can be evaluated with equivalent techniques if the mapping $\chi(\xi)$ is iso-parametric, that is, if it uses the same order expansion functions to map the co-ordinates as the dependent variables. The derivative is then evaluated on the nodal points, ξ_i $(-1 \leq i \leq Q-1)$:

$$\left.\frac{\mathrm{d}u(\xi)}{\mathrm{d}\xi}\right|_{\xi=\xi_i} = \sum_{j=0}^{Q-1} u(\xi_j) \left.\frac{\mathrm{d}\phi_j(\xi)}{\mathrm{d}\xi}\right|_{\xi=\xi_i} = \sum_{j=0}^{Q-1} d_{ij} u(\xi_j) \tag{2.37}$$

where d_{ij} is a *derivative matrix*. A similar derivative matrix can be also defined in multiple dimensions. Note that in two and three dimensions derivatives like $\frac{\mathrm{d}x}{\mathrm{d}\xi}$ need to be re-expressed because $\xi(\chi)$ in not known. For the full formulation of the

differentiation operation within the different types of hybrid elements see Chapter 4 in Karniadakis and Sherwin (2005).

2.1.6 Spectral/*hp* model for the incompressible Navier-Stokes equations

Most of the computational results presented in this thesis have been calculated with the flow solver *Nεκταr* (Karniadakis and Sherwin, 2005). This is a spectral/*hp* element code that spatially discretises the incompressible unsteady Navier-Stokes equations:

$$\begin{aligned} \frac{\partial \mathbf{u}}{\partial t} + \mathbf{u} \cdot \nabla \mathbf{u} &= -\frac{1}{\rho} \nabla p + \nu \nabla^2 \mathbf{u} \\ \nabla \cdot \mathbf{u} &= 0 \end{aligned} \tag{2.38}$$

where ρ is the fluid density, p is the static pressure, and ν is the kinematic viscosity.

The *Nεκταr* code can be applied in all dimensions; however, in this thesis we present flow results in three-dimensional geometries with the use of fully unstructured meshes, as it will be discussed in more detail in the next section (Section 2.2). In the solver, the solution is represented within each element by a C^o continuous high-order expansion of polynomial order P. Discretisation in time is performed via a high-order splitting scheme as presented in Karniadakis et al. (1991).

Equations (2.38) can be expressed as:

$$\begin{aligned} \frac{\partial \mathbf{u}}{\partial t} &= -\frac{1}{\rho} \nabla p + \nu \mathbf{L}(\mathbf{u}) + \mathbf{N}(\mathbf{u}) \\ Q &\equiv \nabla \cdot \mathbf{u} = 0 \end{aligned} \qquad \text{in} \quad \Omega \tag{2.39}$$

where $\mathbf{L}$ and $\mathbf{N}$ are the linear diffusion and nonlinear advection operators respectively[8], and Q gives the continuity equation. The time-splitting scheme in a domain Ω is:

[8] $\mathbf{L}(\mathbf{u}) \equiv \nabla^2 \cdot u = \nabla(\nabla \cdot u) - \nabla \times (\nabla \times u)$, $\mathbf{N}(\mathbf{u}) \equiv -\frac{1}{2}[u \cdot \nabla u + \nabla(u \cdot u)]$ (Karniadakis et al., 1991).

$$\frac{\hat{\mathbf{u}} - \mathbf{u}^n}{\Delta t} = \sum_{q=0}^{J_e-1} \beta_q \mathbf{N}(\mathbf{u}^{n-q}) \tag{2.40}$$

$$\frac{\hat{\hat{\mathbf{u}}} - \hat{\mathbf{u}}}{\Delta t} = -\frac{1}{\rho}\nabla \overline{p}^{n+1} \tag{2.41}$$

$$\frac{\mathbf{u}^{n+1} - \hat{\hat{\mathbf{u}}}}{\Delta t} = \nu \sum_{q=0}^{J_i-1} \gamma_q \mathbf{L}(\mathbf{u}^{n+1-q}) \tag{2.42}$$

where n is the discrete time level ($t_n \equiv n\Delta t$), $\overline{p}^{n+1}$ is the time-mean pressure gradient in time Δt, β_q are the coefficients of an Adams-Moulton family scheme of order J_e, and γ_q are the coefficients of an Adams-Moulton family scheme of order J_i (Karniadakis et al., 1991). The Dirichlet boundary conditions are:

$$\mathbf{u}^{n+1} = \vec{v}_o \quad \text{in} \quad \partial\Omega \tag{2.43}$$

According to the scheme, $\hat{\hat{\mathbf{u}}}$ satisfies incompressibility in Ω: $\nabla \cdot \hat{\hat{\mathbf{u}}} = 0$. This leads the pressure field to (in Ω):

$$\nabla^2 \overline{p}^{n+1} = \nabla \cdot \left(\frac{\hat{u}}{\Delta t} \right) \tag{2.44}$$

where the errors can be minimised by a mixed implicit/explicit boundary condition in $\partial\Omega$ (Karniadakis et al., 1991):

$$\frac{\partial \overline{p}^n + 1}{\partial n} = \mathbf{n} \cdot \left[\sum_{q=0}^{J_e-1} \beta_q \mathbf{N}(\mathbf{u}^{n-q}) + \nu \sum_{q=0}^{J_e-1} \beta_q (-\nabla \times (\nabla \times \mathbf{u}^{n-q})) \right] \tag{2.45}$$

Hence, the pressure gradient is evaluated, and so does the field $\hat{\hat{\mathbf{u}}}$ from Equation (2.41). Equation (2.42) becomes the Helmholtz equation, in which the $\hat{\hat{\mathbf{u}}}$ is the forcing function. The full velocity field is obtained at the time step $n + 1$.

2.2 High-order mesh generation methods

Spectral/*hp* element methods, introduced in Section 2.1, are advantageous over other discretisation methods in terms of accuracy and convergence. However, an accurate solution depends also on the quality of the mesh. For complex geometries it is preferable to use unstructured grids as they can improve the representation of the boundary and allow automation of the mesh generation procedure. Triangular and

tetrahedral elements give great flexibility in generating unstructured meshes; however, unstructured tetrahedral elements are avoided adjacent to solid boundaries because they can be thin and long, and may hinder the approximation of the solution. A structured layer made of high-aspect-ratio elements (prisms or structured tetrahedra) is used instead near wall boundaries. This is known as the *boundary-layer mesh* and is particularly favourable for modelling viscous flows where the development of a boundary layer is part of the solution (Ferziger and Perić, 2002). For highly curved geometries, these approaches can be extended to generate high-order curvilinear (body-conforming) elements which greatly enhance the boundary description and allow for high-order discretisations to be applied (Sherwin and Peiró, 2002; Peiró et al., 2002a).

The mesh generation technique we present here is based on the *Felisa* system by Peiró et al. (1994) and produces three-dimensional high-order elements suitable for spectral/*hp* element discretisations. Figure 2.7 illustrates the example of a simple cylindrical geometry. The process involves first the geometrical representation of the computational domain (Section 2.2.1, Figure 2.7a); next, the generation of a three-dimensional coarse mesh, including a boundary-layer mesh (Section 2.2.2, Figure 2.7b); and, finally, the transformation of straight (linear) tetrahedral elements into high-order curvilinear elements (Section 2.2.3, Figure 2.7c).

2.2.1 Geometry representation

Any arbitrary three-dimensional domain can be described as a volume consisting of several surfaces (*boundary faces*), which are bounded by curves (*boundary edges*), which are themselves defined by points. A successful discretisation strategy that ensures accurate representation of the computational domain (*boundary representation* or B-Rep, Figure 2.7a) proceeds in the reverse order. An example is illustrated in Figure 2.8a. Points are given in Cartersian co-ordinates in a sequence that defines the orientation of the curve they describe. Each curve (edge) is then represented as a piecewise interpolation of a cubic spline through a series of points. A boundary surface (face) is defined in a similar way, by the interpolation of spline curves through a rectangular network of points (surface patch). Within this network of data points, a local co-ordinate system (v, w, N) (see Figure 2.8b) defines the sequence of the

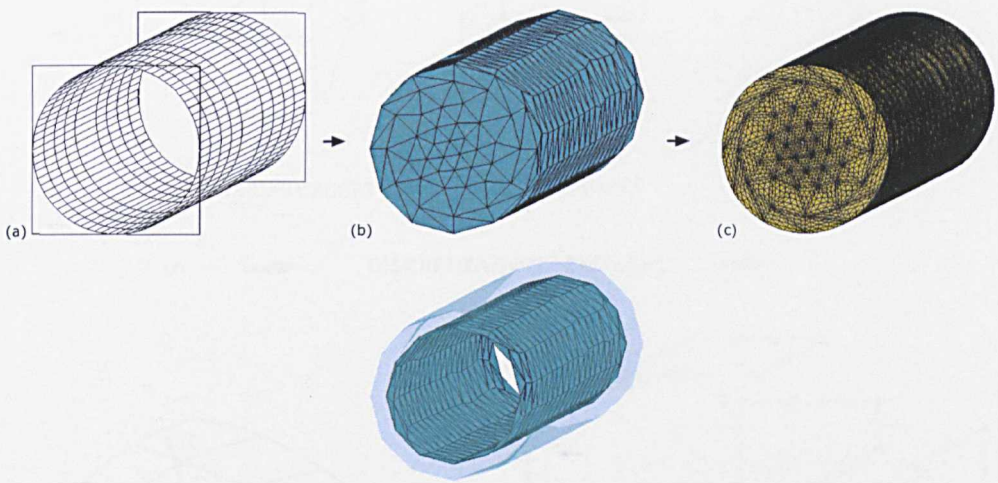

Figure 2.7: Mesh generation process: (a) Boundary representation (B-Rep). (b) Unstructured coarse (linear) mesh. The interior surface of the boundary layer is shown at the bottom. (c) High-order spectral mesh.

interpolation splines through the points of constant v or constant w, as well as the orientation of the surface. The surface normal is chosen to point towards the interior of the domain to be discretised (see Figure 2.8c).

2.2.2 Coarse mesh generation

Once the geometric representation of the computational domain is obtained, a three-dimensional discretisation is achieved using the "bottom-up" approach (Peiró et al., 1994; Karniadakis and Sherwin, 2005). According to this technique the mesh is constructed by first discretising the boundary curves (edges), then the surfaces (based on the edge mesh), and finally the volume (based on the surface mesh). Hence, the starting point of the discretisation of a subsequent component is the end result of the discretisation of a lower dimension component. In practice, a three-dimensional coarse mesh (Figure 2.7b) is generated in three steps:

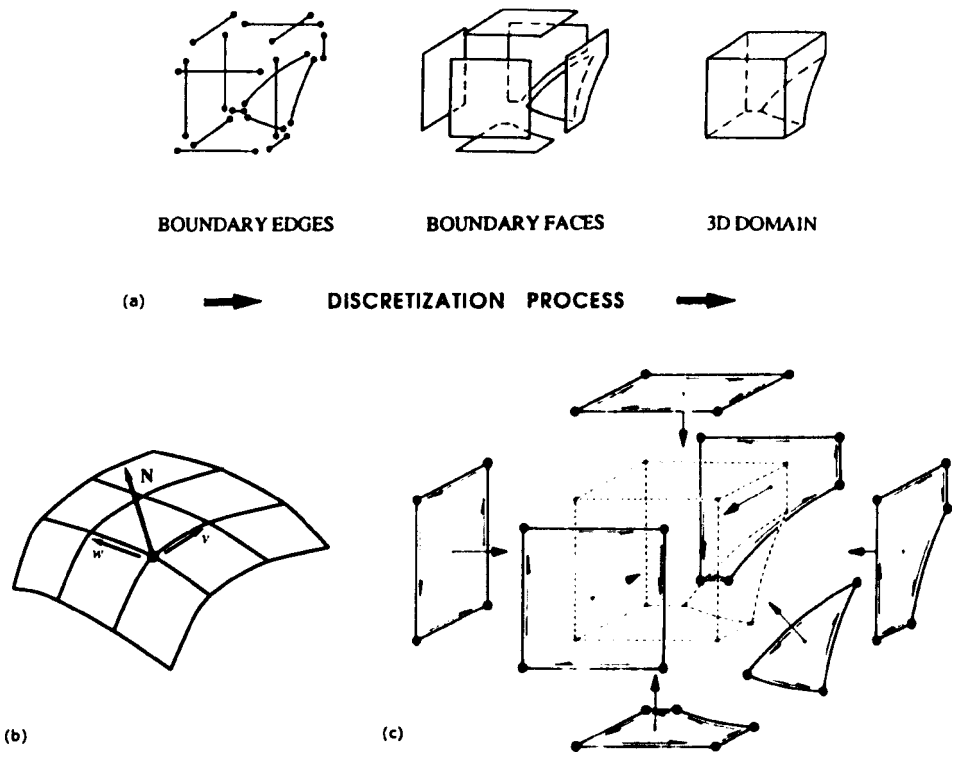

Figure 2.8: Geometry definition: (a) Decomposition of a three-dimensional computational domain. (b) Surface definition. (c) Surface and curves orientation. (After Peiró et al., 1994).

- *Surface triangulation*

The surface boundaries are triangulated according to a generalisation of the *advancing front technique* (Peraire et al., 1993), in which the mesh elements are constructed simultaneously[9] (Figure 2.9). The technique is flexible in terms of size and stretching of the elements it generates.

Boundary curves are discretised by placing nodes along the edges and by connecting successive nodes with straight lines. The length of the line segments, and hence the number of nodes, is controlled by a prescribed value of element size (defined in the *background mesh*). These straight lines form the initial *front*, which is updated continuously during the triangulation process. Each segment from a boundary curve

[9] As opposed to the *Delaunay triangulation* in which the mesh is constructed by connecting points which are predefined in the domain (Peiró et al., 1994).

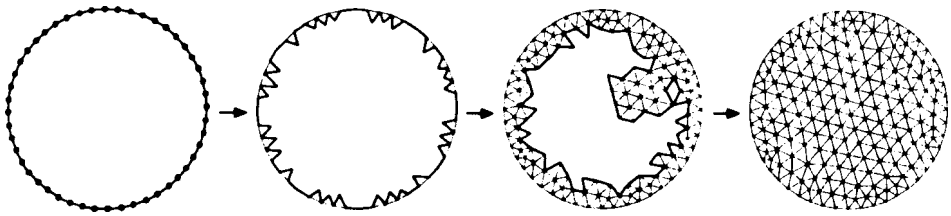

Figure 2.9: Surface triangulation using the *advancing front technique*. The nodes and triangular elements are generated simultaneously. (After Peiró et al., 1994).

becomes a side to a triangular element. New nodes and elements are generated on the surface simultaneously. The *front* is updated after each element generation until it is empty (or the surface is meshed). The process is similar for non-planar surfaces using a mapping from planar (local) to non-planar (global) components (see Peiró et al., 1994).

The resulting mesh can be controlled with the use of a *background mesh*, which defines a minimum mesh spacing, and local sources, which can improve the mesh by local isotropic distributions of elements. These provide the flexibility for the generation of elements of various sizes and stretching, as well as local mesh refinement, which is advantageous for complex geometries.

- *Viscous layer mesh generation*

The boundary (viscous) layer mesh is generated near wall boundaries using a *modified advancing layers method* (Sayma and Peiró, 1995; Peiró and Sayma, 1995). New nodes are added in the interior of the domain along lines almost perpendicular to the solid boundary and at lengths that are consistent with the desired boundary layer thickness. Prismatic or structured tetrahedral elements are produced by connecting these nodes. The boundary layer is a three-dimensional extrusion of the surface mesh (bottom of Figure 2.7b). The viscous layer is extended over continuous solid surfaces within the domain. At the intersections with non-solid boundaries the prismatic elements create a quadrilateral face.

- *Volume mesh generation*

The internal triangular faces of the boundary layer elements (bottom of Figure 2.7b) form the base (initial *front*) for the generation of tethrahedral elements within the three-dimensional domain. New nodes and linear tetrahedral elements are produced simultaneously, in an unstructured fashion, using an *advancing front technique* similar to that for surface triangulation (Peiró et al., 1994). The *front* is updated continuously after the generation of each tetrahedron until the volume is filled.

2.2.3 High-order elements mesh

Curvilinear and body-conforming elements in complex geometries can be produced based on a coarse mesh of linear tethahedra generated with the techniques discussed in Sections 2.2.1 and 2.2.2. A similar "bottom-up" approach is adopted by successively discretising the edges, the faces, and finally the interior of the linear tetrahedra to obtain high-order spectral elements (Sherwin et al., 2000a; Sherwin and Peiró, 2002).

Figure 2.10 shows the different discretisation steps for the generation of a high-order spectral element. The linear edges are subdivided into $P+1$ points for a polynomial interpolation of order P. If the edge is part of a curve of the boundary representation (B-Rep) then the $P-1$ intermediate points are added along the edge at equispaced positions (Figure 2.10a). When the edge is on a face of the B-Rep, the points are placed at equally spaced positions on the surface along a line connecting the two end points of the edge. These interpolation points form the high-order mesh.

High-order triangular elements (faces) can be generated by using a transfinite interpolation within the parametric plane, if the face lies on a B-Rep surface. Figure 2.10b illustrates the various steps of face discretisation. When the face does not belong to a B-Rep surface, a similar interpolation takes place to calculate the co-ordinates of the intermediate points. Transfinite interpolation leads to discretisation of the interior of the tetrahedra to form high-order spectral elements, as shown in Figure 2.10c.

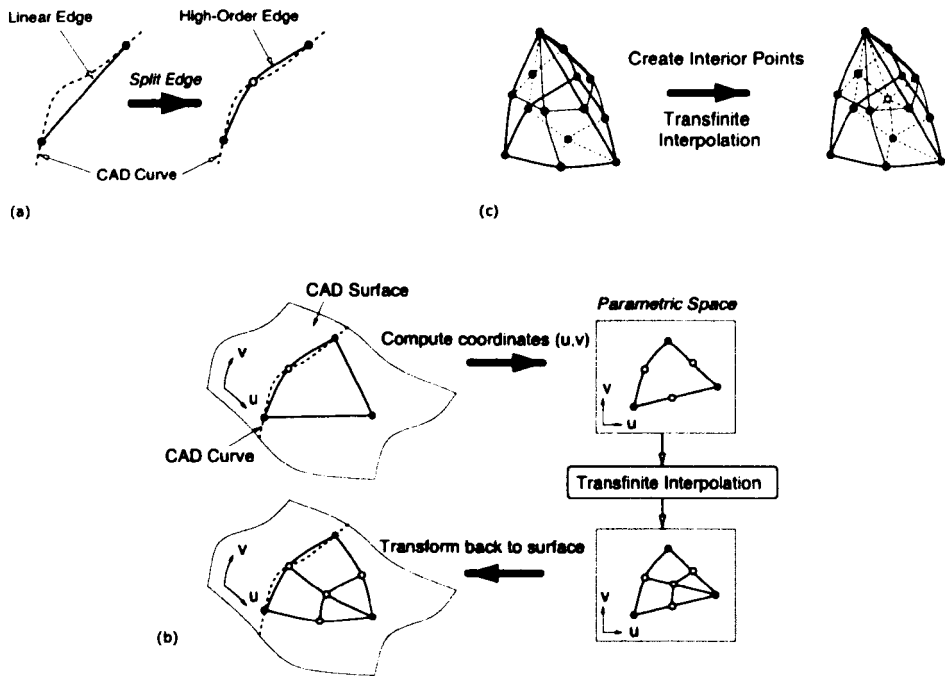

Figure 2.10: Generation of a high-order spectral element: (a) Discretisation of a linear edge. (b) Discretisation of a face of a tetrahedron. (c) Discretisation of a tetrahedral element. (After Sherwin et al., 2000a).

An example of using the above mesh generation technique is given in Figure 2.11a. In this complex geometry (an arterial bypass graft by Sherwin and Peiró, 2002), the prismatic elements are divided into three tetrahedra. If the local surface curvature is convex, then high-order mesh can be generated as described earlier. For locally concave surface curvature the process may lead to invalid high-order elements[10]. A *hybrid discretisation* consisting of a layer of prismatic elements (Figure 2.11b) and an inner mesh of linear tetrahedral elements (Figure 2.11c) can be used instead. This type of discretisation enhances the generation of valid high-order mesh, but it too can generate invalid elements. *Curvature based refinement* is another approach which takes into account the curvature of curves and surfaces in the calculation of the element size. Curvature refinement applied selectively to local regions of concave curvature can improve the quality of the mesh. For further details see Peiró et al. (2002b); Sherwin and Peiró (2002); and Karniadakis and Sherwin (2005).

[10] An element is invalid if the Jacobian is negative or zero (Karniadakis and Sherwin, 2005).

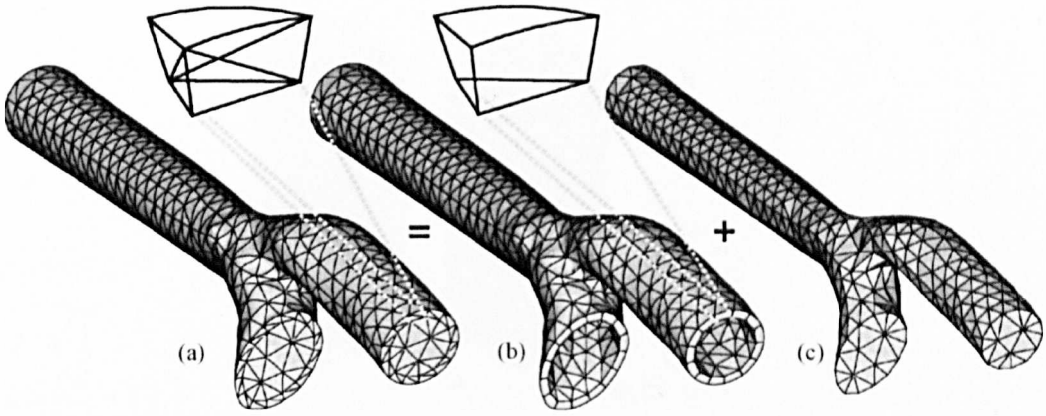

Figure 2.11: Mesh generated on an arterial bypass graft. (a) The boundary layer consists of prismatic elements divided into three tetrahedra. Equally, the boundary layer can be a layer of prismatic elements (b) which surrounds a mesh of linear tetrahedra (c). (After Sherwin and Peiró, 2002).

2.3 Image-based computational modelling

Over the past decades, medical modalities such as the magnetic resonance imaging (MRI) and computerised tomography (CT) have been proved powerful imaging and diagnostic techniques offering detailed medical images of the body and internal organs. An advantage of MRI over CT is the avoidance of ionising radiation. The demand for fast acquisition of images, automated data analysis and diagnosis, which can reduce the time spent in the hospital or the operating theatre, has driven the technology forward. Ongoing research in the field of medical physics attempts to improve the characteristics of these techniques and the quality of the images they produce.

Computational techniques have been more recently introduced to the field with the scope to reconstruct and produce automatically models of anatomical geometries appropriate for computational fluid dynamics (CFD) simulations. The technology is still under development. A major obstacle is that the automation of the image segmentation process with the current MRI and CT technology is still user-dependent. Here, we briefly present a semi-automated process (freeware) by Giordana (2004); Giordana et al. (2005b); and Peiró et al. (2002a, 2007), which can successfully re-

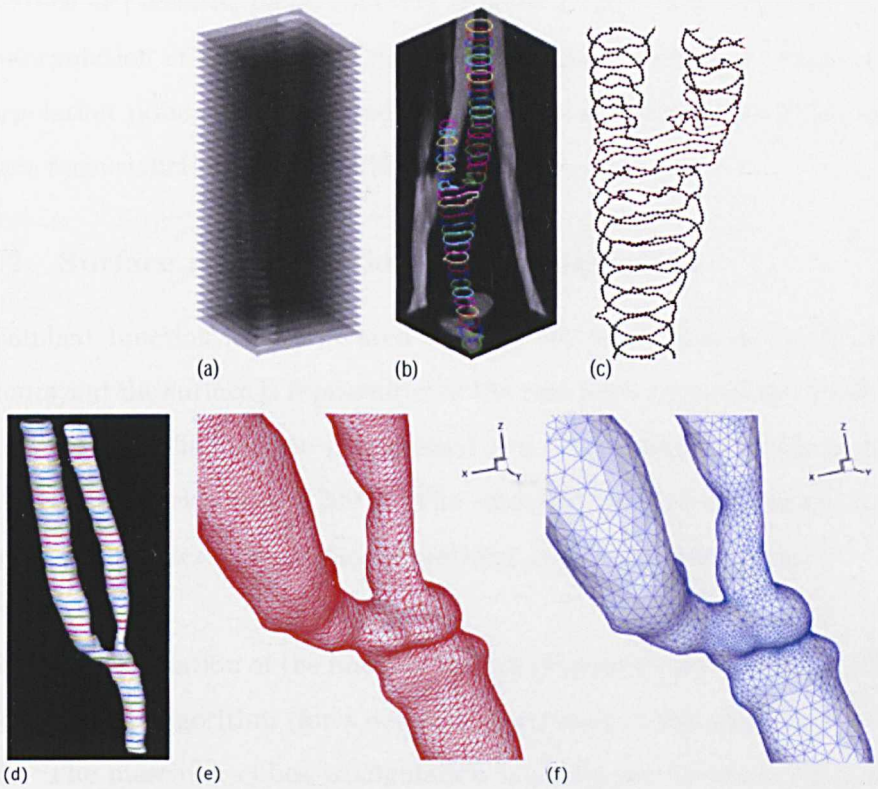

Figure 2.12: Image-based vascular modelling: (a) MRI or CT stack of medical images. (b) Image segmentation and the resulting two-dimensional contours. (c) Generation of interpolation points. (d) Interpolated implicit surface. (e) Marching cubes triangulation. (f) Curvature-based triangulation. (After Peiró et al., 2007).

construct three-dimensional anatomically correct vascular geometries from MRI or CT medical data. The process is summarised in Figure 2.12 where a femoral bypass graft is used as an example (after Peiró et al., 2007).

2.3.1 Image segmentation

MRI or CT produce stacks of two-dimensional cross-sectional slices like that shown in Figure 2.12a. Each slice is expressed as a matrix of pixels, each of which has an intensity value on a grayscale. Image segmentation, in other words the partitioning of the image into the region of interest and the background, is performed using *thresholding*. An intensity value on the boundary of the vessel wall on the slice plane is set as the *threshold criterion* and the vessel wall boundaries are segmented

as a stack of pixelated plane contours (Figure 2.12b). The contours are smoothed by interpolation of spline curves using a least-square technique (Peiró et al., 2007). Interpolation points are generated, which serve as constraints during the implicit surface reconstruction (Figure 2.12c).

2.3.2 Surface reconstruction and triangulation

An implicit function is interpolated through the interpolation points of the plane contours and the surface is represented as the zero iso-contour of the implicit function (Figure 2.12d). The function is expressed as a combination of radial basis functions as described in Peiró et al. (2007). The choice of the radial function can influence the end result in terms of surface smoothing and convergence rates.

An initial triangulation of the implicit surface (Figure 2.12e) is achieved by using the marching cubes algorithm (for a detailed description of the method, see Peiró et al., 2007). The marching cubes triangulation is useful for visualisation purposes, but the quality of the mesh it produces is inadequate for computational fluid dynamics solutions. Peiró et al. (2007) proposed a *curvature-based* triangulation technique to improve the quality of the surface mesh (Figure 2.12f). The mesh quality is further enhanced by smoothing, using a non-shrinking algorithm (modified Taubin's smoothing algorithm, Giordana, 2004; Giordana et al., 2005b). The smoothing process is applied locally and does not alter significantly the local geometry of the boundaries.

Other commercial packages, such as Gambit—a mesh generation software—can also be used for re-triangulation of the surface. Finally, Amira® is a commercial package which can also perform the image segmentation and surface reconstruction process.

Idealised models of intercostal arteries, which are presented in Chapter 3, were constructed with the high-order mesh generation methodology described in Section 2.2 and the flow simulations were performed with the spectral/*hp* flow solver *Nεκταr*, as

discussed in Section 2.1. An anatomically correct rabbit geometry was reconstructed from micro-CT images with the commercial packages Amira® and Gambit. The flow solution in this latter geometry was obtained with the commercial flow solver Fluent® 6.3. Anatomically correct mouse aortic arch geometries, which are presented in Chapter 4, were reconstructed with the techniques discussed in Section 2.3. Steady flow solutions were obtained with the commercial flow solver Fluent® 6.3. In all geometries considered in this thesis, the walls were assumed to be rigid and no wall movements were incorporated into the models. Detailed information on each of the geometries studied, including information on MRI and CT image data, are presented separately in Chapters 3 and 4.

Chapter 3

Flow near side branches in the descending thoracic aorta

This chapter presents an investigation of wall shear stress patterns around the origins of intercostal arteries in the descending thoracic aorta, under both steady and pulsatile flow conditions. Section 3.1 begins with an introduction to this work. The model geometries, governing equations and boundary conditions considered for this study are described in Section 3.2. Section 3.3 presents wall shear stress patterns under steady flow. Effects of Reynolds number and side branch flow partition, as well as effects of arterial geometry, are examined. Instantaneous wall shear stress (WSS), time-averaged WSS and oscillatory shear index patterns under unsteady flow conditions are presented in Section 3.4. The chapter finishes with a discussion of the obtained results, in Section 3.5. Streamline patterns and flow fields for the cases studied are presented in that section.

3.1 Introduction

Atherosclerosis, the disease underlying most heart attacks and strokes, is characterised by the focal accumulation of lipid, cells and connective tissue components within the arterial wall. The non-uniform distribution of these lesions in areas of branching and curvature is consistent with a controlling influence of stresses imposed on the wall by the flow of blood. The current consensus is that lesions occur most frequently in regions of low and fluctuating haemodynamic wall shear stress

(WSS). However, there are differences in the distribution of lesions between species, and between ages within a species, that challenge this consensus. Here we report an investigation of whether the pattern of WSS is sensitive to factors such as Reynolds number (Re), flow division and reversing flow and hence could vary with species and age, or whether it is invariant, implying that the consensus may not apply to all the observed lesion distributions.

Differences in the distribution of lesions between species and ages have been most completely documented for the origins of intercostal arteries within the descending thoracic aorta (see Chapter 1; Weinberg, 2002). In human fetuses, neonates and infants, fatty streaks occur around the downstream margins of these branch ostia (Sinzinger et al., 1980). At later ages, however, they occur at the lateral and then the upstream margins (Sloop et al., 1998), whilst advanced disease tends to completely surround the ostium (Mitchell and Schwartz, 1965). Spontaneous and diet-induced lesions in immature and mature rabbits show the first two patterns (Barnes and Weinberg, 1998, 1999) whereas lesions completely surround intercostal ostia regardless of age in knockout mice lacking the low density lipoprotein receptor and apolipoprotein E (McGillicuddy et al., 2001).

Numerous previous studies using analytical techniques, physical models or computational methods have investigated patterns of flow or WSS in the vicinity of arterial branch points. More recently, allometric studies have examined variations in WSS between species, proposing various scaling laws (Greve et al., 2006; Cheng et al., 2007; Weinberg and Ethier, 2007). However, only a few have systematically studied the effects on WSS of varying Re or flow division between parent and daughter vessel (Cheer et al., 1998) and we are not aware of any that have attempted to explain the age- and species-dependent differences in lesion pattern. In addition, although pulsatile flows have been previously examined around arterial branches (Buchanan Jr. et al., 1999), we are not aware of any study that has investigated effects of reversing flow on WSS patterns. The present study used high-order spectral/hp element methods (see Chapter 2, Section 2.1; Karniadakis and Sherwin, 2005) to compute flow fields and wall shear stresses in the vicinity of model intercostal branch ostia using a range of these parameters. The range includes values appropriate for human

subjects and for the smaller animals that are widely used as models of the human disease. For the majority of computations, a number of simplifying assumptions were made, but the work nevertheless gives insight into the patterns of wall shear stress (WSS) to be expected in vivo, the flow fields that explain them, and the possibility that changes in these parameters might account for different patterns of disease.

3.2 Computational models

3.2.1 Geometries

3.2.1.1 Idealised geometries

In people, rabbits and mice, intercostal arteries originate from the dorsal surface of the descending thoracic aorta in pairs. Effects of varying Re and flow division were first examined on a single branch and subsequently on a pair of branches. For most computations, the geometry of the single branch was approximated as a cylindrical tube, representing the intercostal artery, emerging perpendicularly from a flat surface, representing the dorsal wall of the descending thoracic aorta (Figure 3.1a); similar models of intercostal branches have previously been used by Sobey (1977a,b) and Tutty (1988). The assumption of a flat aortic wall is justified because the diameter of the intercostal artery (D_b) is substantially smaller than that of the thoracic aorta (D_a). Based on previous estimates (Sobey, 1977a,b; Tutty, 1988; Pedley, 1980) and in vivo measurements (Caro et al., 1978; Cornhill and Roach, 1976; Nichols and O'Rourke, 1998), D_b:D_a was assumed to equal 0.1.

Taking D_b (hereafter D) as the unit of length, a segment of aortic wall near the branch was approximated by a rectangular channel $26D$ long in the axial (x) direction, $10D$ wide in the crossflow (y) direction and $5D$ high in the z direction (Figure 3.1a). The cylindrical tube representing the intercostal artery had length $5D$. It was located on the longitudinal centreline of the aortic wall segment and its upstream lip was $10D$ from the upstream edge of the aortic segment.

In studies to assess the sensitivity of the solution to geometric assumptions, the

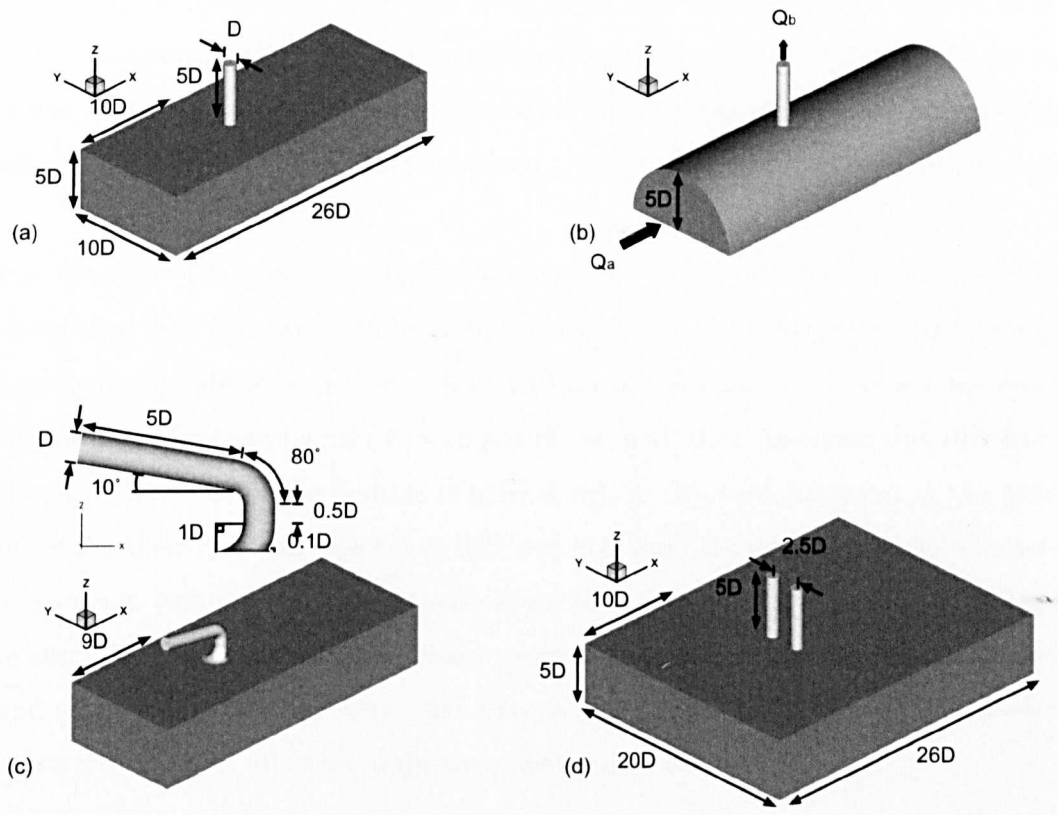

Figure 3.1: Computational domains representing intercostal arteries branching from the thoracic aorta: (a) Simple model of one intercostal artery emerging perpendicularly from the thoracic aorta. (b) More realistic aortic geometry. (c) More realistic geometry of the aorto-intercostal junction. (d) Pair of branches at the same streamwise position. Dimensions in (b) and (c), other than those shown, are the same as in (a). The unit of length, D, is the diameter of the intercostal artery. The flow direction is shown in (b) and is the same for all models.

width of the aortic channel was doubled and the sharp edge of the aorto-intercostal junction was replaced with a rounded lip with radius of curvature $0.1D$. In a further study, the aorta was modelled as a half cylinder of diameter $10D$ and the branch junction as the intersection of two perpendicular cylinders (Figure 3.1b). Flow was also computed for a more realistic model (Figure 3.1c) in which the inflow tract

and flow divider had geometries approximating those seen in histological sections (e.g. Sebkhi and Weinberg, 1994, 1996) and the side branch curved back toward the heart, as observed in corrosion casts (Nier and Weinberg, unpublished data, 2005; Abrahams, 2001). The aim was neither to reconstruct an actual branch nor to define an average geometry but to determine whether the patterns of WSS seen in the simpler model are likely also to apply to geometries of the broad type seen in vivo.

For the case of a pair of intercostal arteries, the width of the domain was again doubled to $20D$ and two cylindrical tubes of the radius and height used previously were symmetrically situated about the longitudinal centreline with a centre-to-centre separation of $2.5D$ and were (a) both positioned with their upstream lips $10D$ from the upstream edge of the domain (Figure 3.1d), or (b) were staggered in the axial direction, their upstream lips being $10D$ and $11D$ from the upstream edge. The separation approximates the minimum observed in en face images of rabbit aortas fixed in situ at physiological pressure (Bond personal communication). Both unstaggered and staggered geometries were used since stagger tends to increase with distance down the aorta. In all cases, walls were assumed to be rigid.

3.2.1.2 Anatomically correct geometry

In addition to the idealised geometries of Figure 3.1, another model was considered, which captures correctly the anatomical features of a pair of intercostal arteries branching from the thoracic aorta.

A corrosion cast was prepared by hand-injection of resin (Batson's No. 17 methyl methacrylate) through the thoracic aorta of a mature rabbit (Harlan Interfauna strain, male, 87 weeks old, 4.1kg) at physiological pressure (100 mmHg) and room temperature (Nier and Weinberg, unpublished data 2005). After solidification of the resin and tissue removal (by Nier and Weinberg, unpublished data 2005), the cast was carefully extracted from the thoracic tract. Figure 3.2 shows a cast from another mature rabbit (45 weeks old) with six pairs of intercostal arteries, prepared under the same conditions. A specimen, which included the third pair of intercostal arteries from the 87-week-old rabbit cast, was prepared by cutting an 11-mm-long section of the thoracic aorta around the pair. The specimen was placed in front

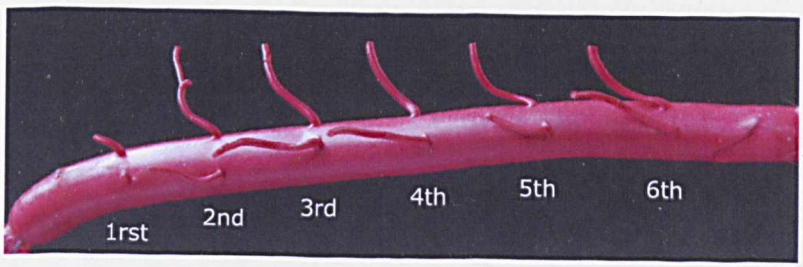

Figure 3.2: Corrosion cast of the thoracic aorta of a mature rabbit with six pairs of intercostal arteries. The aortic flow is from left to right (Nier and Weinberg, unpublished data, 2005).

of a 40kV X-ray beam (at 1000μA) of a micro-CT scanner (Skyscan-1074). Projections were acquired every 0.9^o when rotating the sample between 0^o and 185.4^o, using an exposure time of 120ms. High-resolution two-dimensional images of size 736x736 pixels were constructed by a back-projection algorithm (included in the Skyscan-1074 software) with a voxel size of $20.91\mu m^3$. In total, a data set of 511 cross-sectional images was obtained which was then imported into Amira®, a commercial image segmentation software.

Segmentation of the arterial lumen was performed on every slice in a semi-automated way based on *thresholding*, with the available tools. A three-dimensional representation of the arterial geometry, including an initial surface triangulation, was produced, which subsequently was imported into Rhinoceros® and Gambit for mesh editing. The geometry was smoothed over 500 iterations using an in-house non-shrinking algorithm (modified Taubin's smoothing algorithm, Giordana, 2004; Giordana et al., 2005b) and its ends were opened with the use of in-house cutting tools. Figure 3.3 displays the reconstructed arterial geometry in lateral and proximal to distal views. The geometry was 10.43mm long and had a proximal (inflow) aortic area of approximately $15.05mm^2$, a distal (outflow) aortic area of approximately $14.61mm^2$, while the outflow areas of the proximal and distal branches were approximately $0.19mm^2$ and $0.18mm^2$, respectively (measured with Rhinoceros®). The ratio of diameters between each intercostal artery and the upstream (proximal) end of the thoracic aorta was 0.113 for the proximal intercostal artery and 0.109 for the distal artery,

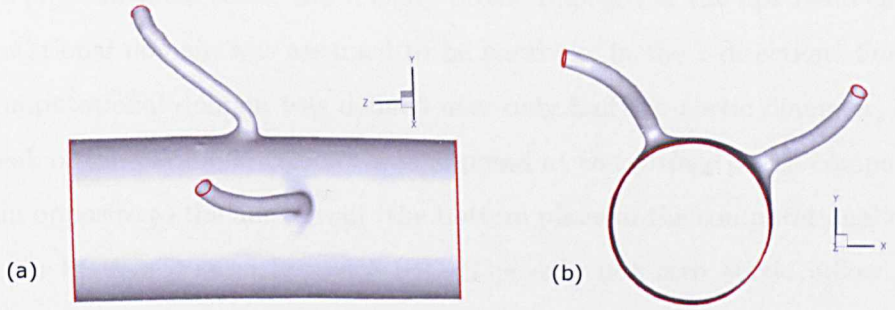

Figure 3.3: Anatomically correct reconstructed geometry of a pair of intercostal arteries from a mature rabbit corrosion-casted at physiological pressure. (a) Lateral view. The mean aortic flow is from left to right. (b) Proximal to distal view. Mean aortic flow is away from the observer.

which verifies our earlier assumption of D_b:$D_a = 0.1$ for the idealised models. The walls were again assumed to be rigid.

3.2.2 Governing equations and boundary conditions

The flow was assumed to be governed by the Newtonian incompressible Navier-Stokes equations:

$$\rho\frac{\partial \mathbf{u}}{\partial t} + \rho(\mathbf{u}\cdot\nabla)\mathbf{u} = -\nabla\mathbf{p} + \mu\nabla^2\mathbf{u} \tag{3.1}$$

$$\nabla\cdot\mathbf{u} = \mathbf{0} \tag{3.2}$$

where $\mathbf{u}$=$[u, v, w]$ is the velocity vector, ρ the fluid density, p the static pressure and μ the dynamic viscosity.

3.2.2.1 Steady flow

The flow is characterised by the Reynolds number defined as $Re = \rho\overline{u}_a D_a/\mu$, where $\overline{u}_a$ is the average velocity of the fluid in the aorta of diameter $D_a = 10D$.

The near branch region was approximated as a channel in most simulations rather

than a pipe. In these cases, the velocity profile imposed at the upstream end of the computational domain was assumed to be parabolic in the z-direction. Further, as the computational domain was defined over only half the aortic diameter, i.e. $5D$, the peak of the parabolic velocity was imposed at the surface of the computational domain opposite to the aortic wall (the bottom plane of the computational domains shown in Figures 3.1a, 3.1c and 3.1d). The only non-zero aortic inflow velocity component was therefore $u_a = u_a(z)$, which in non-dimensional form can be written (assuming $z = 0$ is the channel centerline) as:

$$\frac{u_a}{\overline{u}_a}(z) = \frac{3}{2}\left(1 - \frac{z^2}{25D^2}\right) \tag{3.3}$$

For the geometry of Figure 3.1b, the fully-developed pipe flow condition was considered, which in non-dimensional form can be expressed as

$$\frac{u_a^{pipe}}{\overline{u}_a^{pipe}}(y,z) = 2\left[1 - \frac{(y-y_{a0})^2}{25D^2} - \frac{z^2}{25D^2}\right] \tag{3.4}$$

where $y_{a0} = 5D$, and $\overline{u}_a^{pipe} = \overline{u}_a$.

For the anatomically correct geometry of Figure 3.3, the fully-developed pipe flow was considered again, which for this case can be written as:

$$\frac{u_a^r}{\overline{u}_a^r}(r) = 2\left[1 - 4\left(\frac{r}{D_a^r}\right)^2\right] \tag{3.5}$$

where r is the aortic radius, $D_a^r \approx 9.1 D_b^r$ is the proximal aortic diameter, and $D_b^r \approx 0.48$ is the average intercostal artery diameter.

In the simple idealised geometries, the aortic flow rate, Q_a, was defined as:

$$Q_a = \overline{u}_a A_a = \overline{u}_a 100D^2 \tag{3.6}$$

where A_a is the full height channel inflow area $100D^2$. Clearly if the aorta had been modelled as a pipe the cross sectional area would have been ${A_a}^{pipe} = \pi {D_a}^2/4 \cong 0.8 \times 100D^2$ and so the equivalent pipe flow rate is 80% of that considered in the

following.

The outflow velocity, $w_b(x, y)$, at the side branch (where $u_b = v_b = 0$) can be written in non-dimensional form as:

$$\frac{w_b}{\overline{w}_b}(x, y) = 2\left[1 - 4\left(\frac{x - x_0}{D}\right)^2 - 4\left(\frac{y - y_0}{D}\right)^2\right] \tag{3.7}$$

where $\overline{w}_b$ is the side branch average velocity, A_b is the branch cross sectional area, and $x_0 = 10.5D$, $y_0 = 5D$. Finally the side branch pipe flow rate, Q_b, is defined as:

$$Q_b = \overline{w}_b A_b = \overline{w}_b \pi D^2/4. \tag{3.8}$$

3.2.2.2 Time-periodic flow

Time-periodic flow is characterised by the mean Reynolds number defined as $Re_m = \rho \overline{u}_a^m D_a/\mu$, where $\overline{u}_a^m$ is the temporal average velocity of the fluid in the aorta of diameter $D_a = 10D$. To fully describe the flow, another non-dimensional parameter is required. Here, we adopt the reciprocal of the Strouhal number, St, which is known as the reduced velocity parameter and is defined as (Sherwin and Blackburn, 2005):

$$U_{red} = \frac{\overline{u}_a^m T}{D_a} \tag{3.9}$$

The Womersley number, $\alpha = D_a/2\sqrt{\omega/\nu}$, which is commonly used in describing pulsatile flows, does not include information about axial length scales. Instead, U_{red} can be seen as the convective length in diameters that the mean flow progresses within a temporal period T. It is related to the Womersley and Reynolds numbers according to: $U_{red} = \pi Re/(2\alpha^2)$.

A Womersley-type solution for two-dimensional flow driven between two parallel plates by a pulsating pressure gradient (Landau and Lifshitz, 1959; Loudon and Tordesillas, 1998) was applied at the inlet velocity profile. This is written in complex form as [see Appendix A.1, Equation (A.6), for an analytical derivation]:

$$u_{osc}(z, t) = \frac{A_p}{i\omega\rho}\left[1 - \frac{\cosh\left(\alpha i^{1/2}\frac{z}{5D}\right)}{\cosh\left(\alpha i^{1/2}\right)}\right] e^{i\omega t} \tag{3.10}$$

where A_p is the amplitude of the pulsating pressure gradient $\frac{\partial p}{\partial x} = -A_p e^{i\omega t}$, ω is the angular frequency, and $5D$ is the channel half-height. The real part of the Equation (3.10) is analytically evaluated in Section A.1.1 of the Appendices [Equation (A.11)]. The analytical solution for the velocity gradient can be found in Loudon and Tordesillas (1998).

The sectionally averaged oscillatory component of the inflow velocity (over $A_a = 100D^2$) is:

$$\overline{u}_{osc}(t) = \frac{A_p}{i\omega\rho}\left[1 - \frac{1}{\alpha i^{1/2}}\tanh\left(\alpha i^{1/2}\right)\right]e^{i\omega t} \tag{3.11}$$

which has a zero temporal average, resulting in zero net flow [see Equation (A.7) and Section A.1.2 of the Appendices for an analytical derivation of the above expression and evaluation of the real part].

The temporal waveform of the sectionally averaged inflow was described by a steady component plus a single sinusoidal harmonic. This is valid due to the linearity of the Navier-Stokes equations in the case of two-dimensional fully developed channel flow (Loudon and Tordesillas, 1998). The only non-zero aortic inflow velocity component was $u_a^p = u_a^p(z,t)$, which in non-dimensional form can be written (assuming $z = 0$ is the channel centerline) as:

$$\frac{u_a^p}{\overline{u}_a^p}(z,t) = \frac{3}{2}\left(1 - \frac{z^2}{25D^2}\right) + \frac{3\omega\rho}{A_p\alpha^2}\Re\left\{u_{osc}(z,t)\right\} \tag{3.12}$$

where $\overline{u}_a^p$ is the sectional average, and $\Re\{\}$ denotes the real part of the complex function. Equation (3.12) was imposed additionally at the computational domain opposite to the aortic wall (the bottom plane of the computational domains shown in Figures 3.1a, 3.1c and 3.1d).

The unsteady aortic flow rate is $Q_a^p = Q_a + A_q e^{i\omega t}$, where $Q_a = \overline{u}_a A_a = \overline{u}_a 100D^2$ is the steady flow component and A_q is the amplitude of the pulsating volume flow

rate. In general, there is a phase lag between the volume flow rate and the driving pressure gradient waveforms. In addition, the amplitude of the former decreases with increasing Womersley number (Loudon and Tordesillas, 1998). The oscillatory component of the aortic volume flow rate is analytically expressed in Equation (A.12) of the Appendices (Section A.2).

For simplicity, the outflow side branch velocity, $w_b^p(x, y, t)$ (where $u_b^p = v_b^p = 0$), was expressed as a product of a fully developed Hagen-Poiseuille profile and a sinusoidal waveform of the same angular frequency, ω, as the aortic pulse. This can be written in non-dimensional form as:

$$\frac{w_b^p}{\overline{w}_b^p}(x, y, t) = 2\left[1 - 4\left(\frac{x - x_0}{D}\right)^2 - 4\left(\frac{y - y_0}{D}\right)^2\right] \cdot [1 + A\sin(\omega t + \phi)] \qquad (3.13)$$

where $\overline{w}_b^p$ is the side branch sectional average, A is the amplitude of the sinusoidal wave, ϕ is the phase shift between the branch and the aortic waveforms, and $x_0 = 10.5D$, $y_0 = 5D$. The side branch pipe flow rate is $Q_b^p = \overline{w}_b A_b \cdot [1 + A\sin(\omega t + \phi)]$, where $A_b = \pi D^2/4$ is the branch cross sectional area.

It is noted that the oscillatory components of the aortic and branch flow rates have a zero average in the above analysis, that is, the oscillating fluid volume alone results on average in zero net flow. The flow of fluid is driven by the steady components. Hence, in Section 3.4, where results under unsteady flows are discussed, the flow rate ratio between the branch and the aorta refers to the average flow rates (Q_b:Q_{a_m}), which can be simply found from the steady components. Clearly, instantaneous variations of the flow division [Q_b:$Q_a(t)$] may vary and a phase shift of $\phi = 0$ between the branch and the aorta does not necessarily correspond to in-phase sinusoidal waveforms (see Section A.2 of the Appendices for an analytical expression of the oscillatory component of the aortic waveform).

Time-averaged wall shear stress

The time-averaged wall shear stress magnitude can be expressed as:

$$\tau_{av} = \frac{1}{T}\int_0^T |\vec{\tau}_w|\, dt \tag{3.14}$$

where $|\vec{\tau}_w|$ is the magnitude of the wall shear stress vector.

Oscillatory Shear Index

A haemodynamic parameter that is often used to describe temporal oscillations of the wall shear stress is the oscillatory shear index or OSI (e.g. Buchanan Jr. et al., 1999), defined according to He and Ku (1996) as:

$$\mathrm{OSI} = \frac{1}{2}\left(1 - \frac{\left|\frac{1}{T}\int_0^T \vec{\tau}_w dt\right|}{\frac{1}{T}\int_0^T |\vec{\tau}_w|\, dt}\right) \tag{3.15}$$

where $\vec{\tau}_w$ is the instantaneous wall shear stress vector. The oscillatory shear index is a measure of the deviation of the wall shear stress vector from the axial direction of flow over the cycle. It takes values in the range of 0 to 0.5, with 0 corresponding to unidirectional wall shear stress, and 0.5 to zero time-averaged wall shear.

3.2.3 Computational methods

For the idealised geometries, non-propriety software was used to create a hybrid mesh of body-conforming prismatic and unstructured tetrahedral elements (Peiró et al., 2002a; Sherwin and Peiró, 2002). A prismatic boundary layer mesh was used at the wall to enhance the modelling of viscous flows (Papaharilaou et al., 2002); in all cases of Figure 3.1, it had a thickness of $0.3D$. For the simple, single-branch geometry, a mesh of 452 prismatic and 2116 tetrahedral elements was generated. To test that this was sufficient, a mesh with 908 prismatic and 6536 tetrahedral elements was also created. The increase in the total number of mesh elements from 2568 to 7444 changed the streamwise force on the aortic wall by $< 0.01\%$. For the geometry of Figure 3.1b a mesh of 7034 elements (902 prisms, 6132 tetrahedra) was used. The mesh for the more realistic branch geometry (Figure 3.1c) contained 25391 elements (1950 prisms and 23441 tetrahedra), while those for the staggered

and unstaggered pairs of branches contained 13446 (1668 prisms, 11778 tetrahedra) and 13523 (1664 prisms, 11859 tetrahedra) elements, respectively.

The solution was computed using a spectral/hp element method described by Karniadakis and Sherwin (2005) (see Chapter 2). The code has previously been used in various applications (Sherwin et al., 2000b; Giordana et al., 2005a). An increase in the order of the polynomial expansion within each element from 4 to 6 produced an approximately 2% decrease in the streamwise force. Hence the computations were performed at a polynomial order of 6, which for the main mesh of the simple geometry corresponds to 266 336 local degrees of freedom per variable.

For the anatomically correct geometry of Figure 3.3, surface re-triangulation was performed in Gambit. A prismatic boundary layer of thickness 0.1mm was added internally to the geometry, before the generation of a volume mesh of unstructured tetrahedral elements. The mesh contained 1 155 250 hybrid elements. The solution was computed using Fluent® 6.3 and a second-order upwind discretisation scheme with a second-order pressure scheme.

3.3 Steady flow

The main results of this study are summarised in Figure 3.4, which shows aortic WSS magnitude around the ostium of the simple model for a range of Re and flow divisions (Q_b:Q_a). (Because some features show better in grayscale, Section A.3 of the Appendices shows grayscale versions of some of the figures in this chapter.) Surface streamlines indicating flow direction immediately above the wall are also shown. WSS was normalised by the inflow WSS (equivalent to the local shear rate relative to the inflow shear rate). Effects of holding Q_b:Q_a at its lowest value and varying Re (top row of Figure 3.4) are considered first, effects of varying Q_b:Q_a at the lowest value of Re (left hand column of Figure 3.4) are considered next, and lastly effects of changing Re and Q_b:Q_a together are described.

3.3.1 Effect of Reynolds number at constant flow partition

The top row of Figure 3.4 shows results for Q_b:Q_a held at 0.08%. At Re = 30, the lowest value examined, normalised WSS (WSS_n) was comparatively uniform around the ostium, with only slightly elevated values on the ostial lip, and the surface streamlines were everywhere almost parallel to the longitudinal axis. At Re = 150, WSS_n was slightly elevated immediately upstream and downstream of the branch orifice and the upstream streamtraces converged towards the ostium. As Re was further increased to 500, the upstream and downstream regions of high WSS_n enlarged, the downstream region taking on the shape of a streak, and WSS_n decreased at the lateral margins of the orifice. These trends in WSS_n were exaggerated when Re was at its maximum of 1500. Streamlines in the upstream region converged more sharply towards the orifice (suggesting local acceleration of fluid particles) and diverged in the downstream region (suggesting local deceleration). In all cases, the streamlines were symmetrical about the centre line although this was not explicitly imposed by the numerical algorithm (see Discussion and Figure 3.16a for an analysis of the flow features underlying these patterns).

3.3.2 Effect of flow partition at constant Re

The left hand column of Figure 3.4 shows WSS_n patterns and surface streamlines calculated for Re = 30. At the lowest side branch flow partition (Q_b:Q_a = 0.08%), WSS_n was almost uniform except for slightly increased values on the ostial lip, and the streamlines were almost straight, as noted above. As Q_b:Q_a increased, a region of higher WSS_n developed upstream of the ostium, where the surface streamlines converged towards the branch, suggesting acceleration of the near-wall fluid. Increases in Q_b:Q_a also reduced WSS_n in a circumscribed region immediately downstream of the branch, except on the lip itself where it remained elevated. Streamlines diverged in this area. (Effects of increasing flow partition on the flow field underlying these patterns are presented in the Discussion and Figures 3.15 and 3.16b).

3.3.3 Effects of changing Re and Q_b:Q_a together

The remainder of Figure 3.4 shows WSS_n patterns and surface streamlines for other combinations of these values of Re and Q_b:Q_a. In all rows, increasing Re led to a

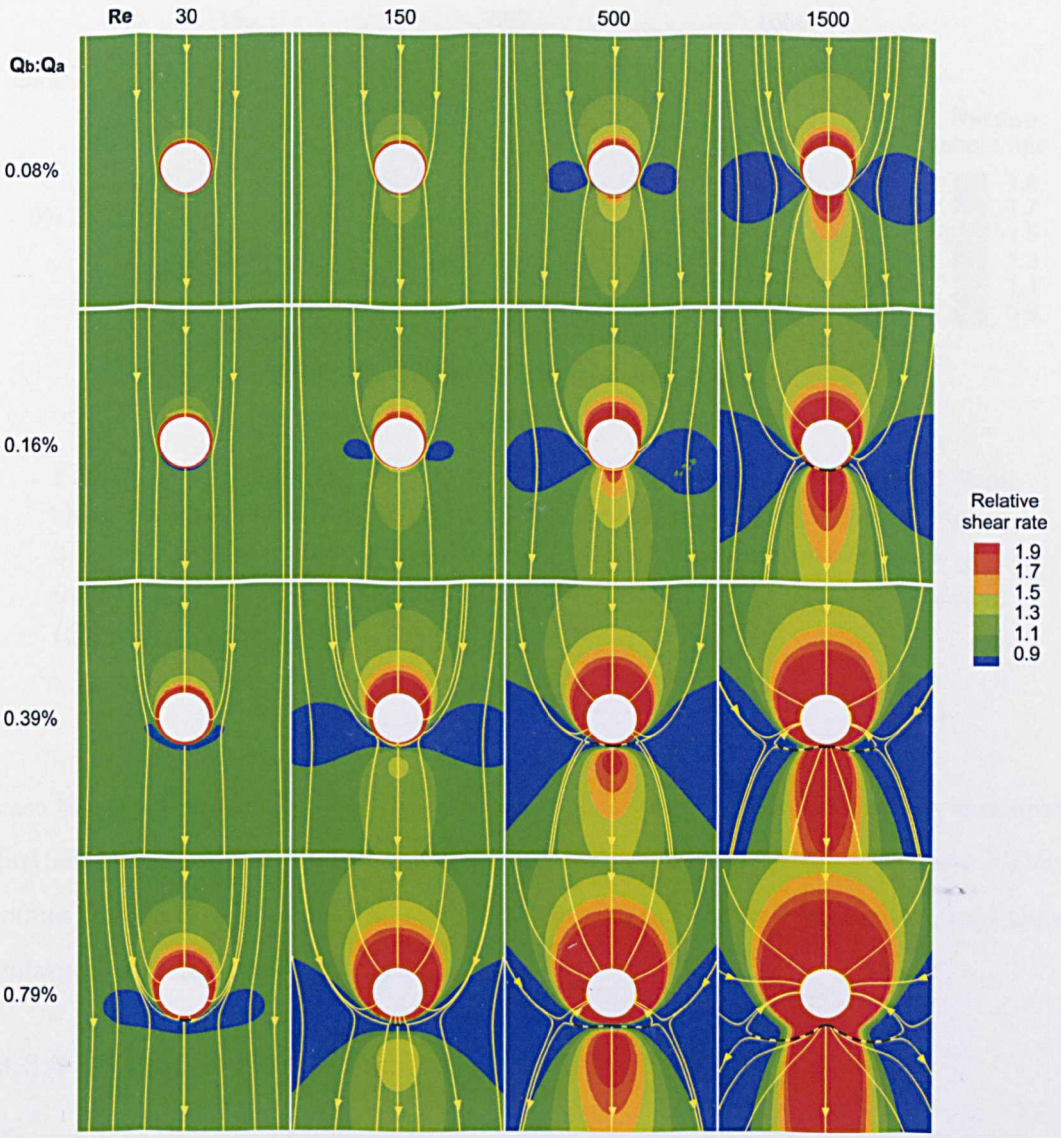

Figure 3.4: Magnitude and direction of non-dimensionalised aortic wall shear stress around the ostium of the simple intercostal junction of Figure 3.1a. Mean aortic flow is from top to bottom. The simulations were performed at a range of Reynolds numbers and flow partitions to account for different species and ages within a species. Dashed lines indicate flow stagnation.

decrease of WSS_n at the sides of the branch and an increase upstream and downstream. In all columns, increasing Q_b:Q_a enlarged the areas where WSS_n was altered and intensified the differences in its magnitude. It also moved the low-shear side lobes downstream and extended the downstream region of reversed flow. In every

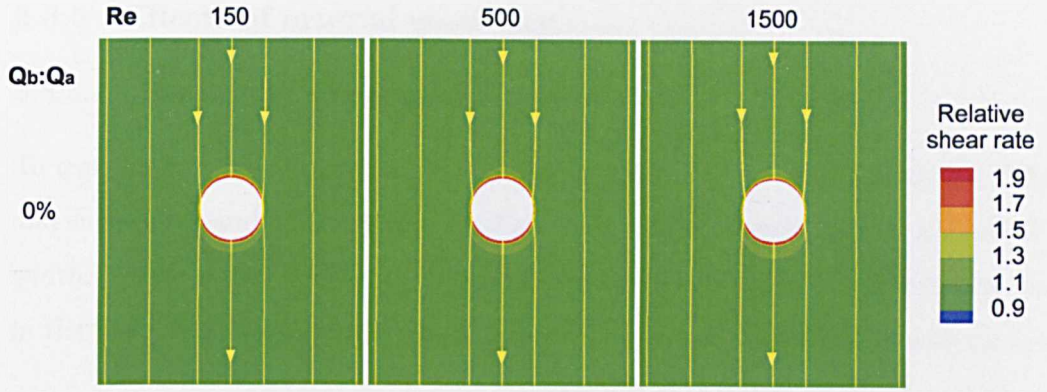

Figure 3.5: Magnitude and direction of non-dimensionalised aortic wall shear stress around the ostium of the simple intercostal junction of Figure 3.1a. Mean aortic flow is from top to bottom. The simulations were performed at a range of Reynolds numbers for the case of ligated side branch ($Q_b = 0$).

case the upstream region was characterized by elevated WSS_n; this region extended further upstream and around the orifice at higher Re and Q_b:Q_a. At these higher values, stagnation lines were observed downstream of the branch ostium, and they enlarged with increasing Re and Q_b:Q_a.

3.3.4 Ligated side branch: $Q_b = 0$

To simulate the case of ligation of intercostal arteries, which is a common practice during animal experiments or surgical operations of, for example, thoracoabdominal aortic aneurysms (TAAAs), the side branch flow was set to zero. Figure 3.5 shows WSS_n patterns and surface streamlines for three moderate Reynolds values. For $Re = 150$, WSS_n was slightly elevated on the ostial lip and surface streamlines were everywhere almost parallel to the longitudinal axis. For $Re = 500$ and 1500, the patterns were indistinguishable from those at lower Re values. The effect on WSS_n of increasing Reynolds number for zero side branch flow appeared to be negligible.

3.3.5 Effects of arterial geometry

3.3.5.1 Sensitivity to geometric assumptions

To test the possibility that the side boundary conditions affected the results, WSS_n and surface streamlines were examined after the aortic channel had been doubled in width. At $Re = 500$ and $Q_b{:}Q_a = 0.79\%$, there was an approximately 3% increase in the mean WSS in a square region of size $3D$ centred around the branch ostium.

The effect of rounding the sharp edges of the aorto-intercostal junction with a rounded lip with radius of curvature $0.1D$ was also investigated at $Re = 500$ and $Q_b{:}Q_a = 0.79\%$. There was an approximately 1.7% decrease in the streamwise-acting force.

3.3.5.2 Paired intercostal branches

The two configurations for paired branches—ostia at the same and at staggered streamwise positions—were tested at $Re = 500$ and $Q_b{:}Q_a = 0.79\%$. In both cases (Figure 3.6), the pattern of WSS_n around each ostium was broadly similar to that observed for a single branch under the same conditions (third image in bottom row of Figure 3.4). Differences were restricted to the region between the two ostia, where the areas of low WSS_n seen to the sides and slightly downstream of individual ostia were truncated and merged. The WSS_n pattern was symmetrical about the axial midline when the ostia were at the same streamwise position, but not when they were staggered. Interestingly, no fluid flowing close to the wall between the two ostia appeared able to move downstream of the ostia; rather, the flow turned towards one or other of them. In the staggered case, there was a more complex pattern which maintained many of the topological features of the unstaggered case. However, the downstream centreline stagnation point in the unstaggered case split into two stagnation points in the staggered configuration.

3.3.5.3 Realistic aortic geometry

Modelling the aorta as a half cylinder (Figure 3.1b), with the junction being the intersection between two perpendicular cylinders, did not qualitatively alter the pattern of WSS around the branch ostium at $Re = 500$ and $Q_b{:}Q_a = 0.79\%$ (Figure

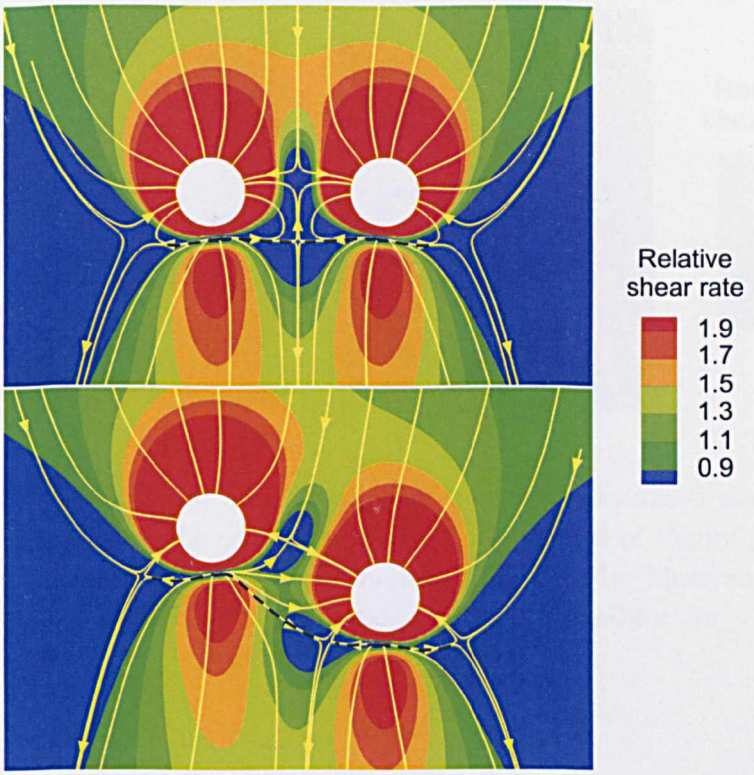

Figure 3.6: Magnitude and direction of non-dimensionalised aortic wall shear stress around a pair of intercostal ostia at the same streamwise position (top, Figure 3.1d) and at staggered positions (bottom). Mean aortic flow is from top to bottom. The simulations were performed for $Re = 500$ and Q_b:$Q_a = 0.79\%$. Dashed lines indicate flow stagnation.

3.7a). The high WSS_n region upstream and around the ostial lip was reduced slightly in magnitude.

3.3.5.4 Realistic branch geometry

Using the more realistic geometry of Figure 3.1c, again at $Re = 500$ and Q_b:$Q_a = 0.79\%$, the WSS_n pattern (Figure 3.7b) appeared nearly identical in character to the equivalent obtained for the simple geometry. WSS_n remained elevated upstream of the ostium despite the gently curving inflow tract.

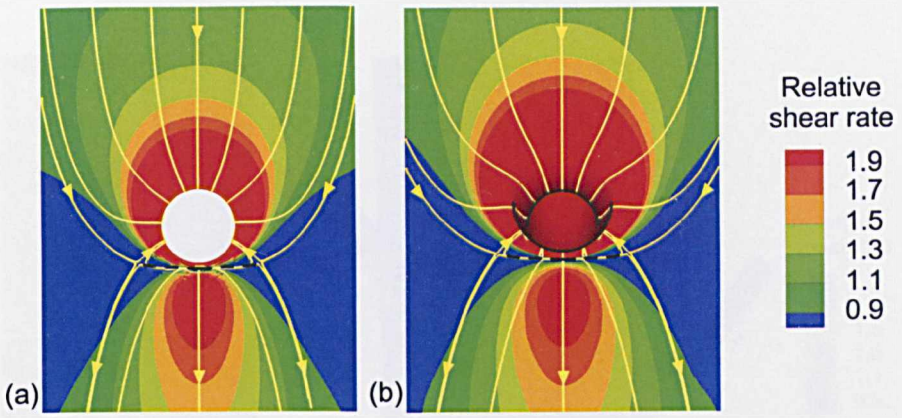

Figure 3.7: Magnitude and direction of non-dimensionalised aortic wall shear stress around the ostium of (a) the aortic model of Figure 3.1b and (b) the realistic aorto-intercostal junction of Figure 3.1c. Mean aortic flow is from top to bottom. The simulations were performed for $Re = 500$ and $Q_b{:}Q_a = 0.79\%$. Dashed lines indicate flow stagnation.

3.3.5.5 Anatomically correct geometry

Computation of the relative shear rate in the anatomically correct geometry of Figure 3.3, for $Re_{D_a^r} = 500$ and $Q_b^r{:}Q_a^r = 0.79\%$, resulted in the pattern shown in Figure 3.8. WSS was normalised in this case by the value that corresponds to a straight tube of diameter equal to that of the proximal aortic diameter, D_a^r, at the same mean flow rate; which can be expressed as $8\mu^2 Re_{D_a^r}/(\rho D_a^{r2})$, or $32\mu Q_a^r/(\pi D_a^{r3})$. The same colour and contour levels as those for the patterns of the idealised geometries were used to allow comparison.

The localised WSS_n pattern around the origin of each intercostal artery was characterised by elevated values upstream and downstream of the ostia and low values at the sides. It resembled in character the pattern seen in the idealised geometry for the same flow conditions (third image in the bottom row of Figure 3.4). However, the two patterns differed in that the high-shear region seen upstream and around the ostial lip in the idealised geometry, was less extended in the anatomically correct geometry. In addition, in the anatomically correct geometry, WSS_n had higher values in the downstream region than in the immediate upstream region; the opposite was observed in the idealised case. Surface streamlines converged upstream and

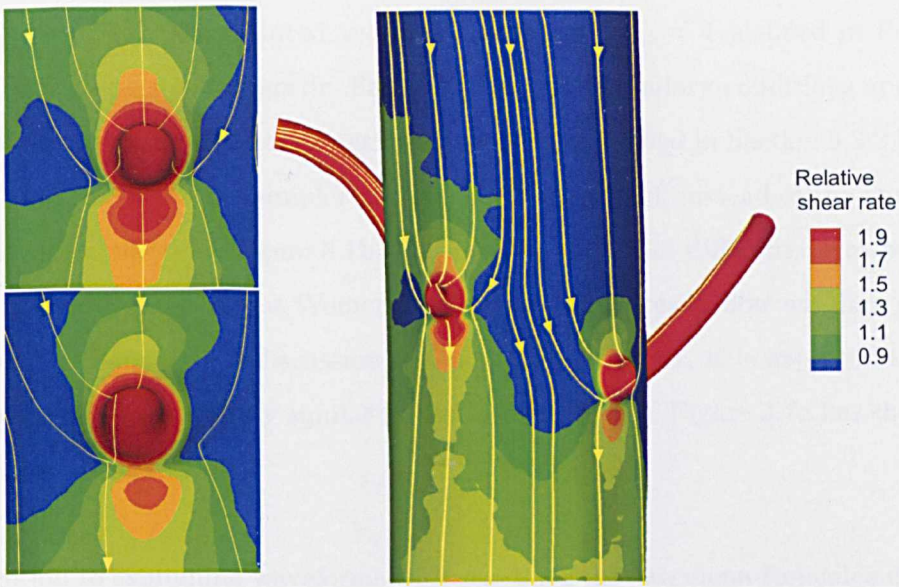

Figure 3.8: Magnitude and direction of non-dimensionalised aortic wall shear stress in the anatomically correct geometry of Figure 3.3. Mean aortic flow is from top to bottom. On the left, images show enlargements of the regions around the proximal (top) and the distal (bottom) branches. The simulations were performed for $Re_{D_a^r} = 500$ and $Q_b^r{:}Q_a^r = 0.79\%$.

diverged downstream of both branch ostia. Near-wall fluid between the two ostia was able to move downstream of them, unlike the result for the staggered idealised geometry (bottom image of Figure 3.6). This seems reasonable since the streamwise distance and the centre-to-centre separation between the two ostia was larger than in the idealised staggered geometry (approximately $1.7D_b^r$ centre-to-centre distance in the streamwise direction and $3.7D_b^r$ centre-to-centre separation in the crossflow direction). Surface streamlines between the two ostia first slightly deviated toward the proximal branch, then changed direction toward the distal branch, and finally ran almost parallel to the longitudinal axis downstream of both branches.

3.4 Time-periodic flow

Effects of unsteady flow on the aortic wall shear stress magnitude around the ostium of the simple model of Figure 3.1a were examined for two moderate mean Reynolds

numbers, Re_m = 150 and 500, at the same average side branch flow partition, Q_b:Q_{a_m} = 0.79%, and reduced velocity parameter, U_{red} = 4 [defined in Equation (3.9), with respect to the aortic diameter D_a]. The boundary conditions applied at the aortic inlet and side branch outflow have been described in Section 3.2.2.2. (It is noted that the use of the simpler geometry of Figure 3.1a, instead of the more realistic aortic geometry of Figure 3.1b, may involve somewhat different development of the flow due to the different Womersley solutions of unsteady flow within a circular tube and a channel—see discussion in Chapter 1. However, it is expected that the flow pattern is qualitatively similar in both geometries, as Figure 3.7a has shown for the case of steady flow.)

In addition to examining waveforms with $\phi = 0$ for the two mean Reynolds numbers (presented in Figures 3.9a for Re_m = 150 and 3.10b for Re_m = 500), effects of different phase lag and side branch peak-to-mean value were considered for Re_m = 150 (Figures 3.9b and 3.9c), and effects of changing the aortic peak-to-mean value were considered for Re_m = 500 (Figure 3.10a). Patterns of time-averaged WSS and oscillatory shear index follow in Figures 3.11 - 3.14.

3.4.1 Effects of side branch flow waveform characteristics at Re_m=150

3.4.1.1 Flow waveforms with $\phi = 0$

Figure 3.9a displays instantaneous WSS_n patterns at four discrete times through the cycle for Re_m = 150, average Q_b:Q_{a_m} = 0.79%, U_{red} = 4 (equivalent to St = 0.25 or $\alpha \approx 7.7$), and an aortic peak-to-mean flow ratio of approximately 1.11 (quasi-steady bulk flow). A sinusoidal waveform, with a phase shift of $\phi = 0$ with the aortic inflow waveform and with an amplitude of 0.5, was assigned to the branch outflow. Regions of high WSS_n around the ostial lip, as well as upstream and downstream of it, were greatest in size during mid-deceleration, and lowest in size during mid-acceleration (second and fourth images of Figure 3.9a, respectively). At the same time points, the lateral low WSS_n regions were also most and least extensive, respectively. During the rest of the cycle, the patterns were intermediate. However, the changes in WSS_n pattern over the cycle were small; the main features remained qualitatively similar to the steady-flow case for the equivalent mean Re and Q_b:Q_a (second image in the

bottom row of Figure 3.4). In all cases, surface streamlines in the upstream region converged towards the branch (suggesting local acceleration of fluid particles) and diverged in the downstream region (suggesting local deceleration).

3.4.1.2 Flow waveforms with $\phi \neq 0$

Introducing a phase shift of $\phi = \pi$ in the side branch flow waveform with respect to the aortic waveform, produced the instantaneous WSS_n patterns shown in Figure 3.9b. The rest of the flow conditions were unchanged [$Re_m = 150$, Q_b:$Q_{a_m} = 0.79\%$, $U_{red} = 4$ (or St = 0.25, or $\alpha \approx 7.7$), aortic peak-to-mean$\approx$1.11, and side branch peak-to-mean=1.5]. Regions of high and low WSS_n were most extensive during late deceleration/early acceleration (third image of Figure 3.9b), and least extensive during late acceleration/early deceleration (peak aortic flow, first image of Figure 3.9b). Hence, the greatest effects on the WSS_n pattern appeared one-quarter of the time-period later than that for the previous case ($\phi = 0$, Figure 3.9a), despite the 180^o phase shift between the side branch and aortic waveforms. Again, changes in WSS_n over the cycle were small and the basic pattern was similar to the steady-flow result. Streamline patterns were similar to the previous and steady-flow cases, converging in the upstream region and diverging in the downstream region.

3.4.1.3 Reversing side branch flow waveform ($\phi \neq 0$)

Assigning a peak-to-mean flow ratio of 2.75 to the side branch flow waveform, and thus making the side branch flow reverse for approximately one third of the cycle, while still with a phase shift of $\phi = \pi$ with the aortic flow, generated the instantaneous WSS_n patterns of Figure 3.9c. The rest of the flow conditions were again unchanged [$Re_m = 150$, Q_b:$Q_{a_m} = 0.79\%$, $U_{red} = 4$ (or St = 0.25, or $\alpha \approx 7.7$), and aortic peak-to-mean$\approx$1.11]. Initiation of side branch flow reversal, at peak aortic flow (first image of Figure 3.9c), resulted in a new WSS_n pattern. A localised semi-circular region of low WSS_n appeared immediately upstream of the ostium. WSS_n values remained elevated on the ostial lip. Surface streamlines diverged in the upstream and lateral regions (indicating local deceleration of the aortic flow particles) and were almost parallel to the longitudinal axis downstream of the branch. During the middle of the deceleration phase (second image of Figure 3.9c), the previously formed low WSS_n values upstream of the branch decreased in size and moved fur-

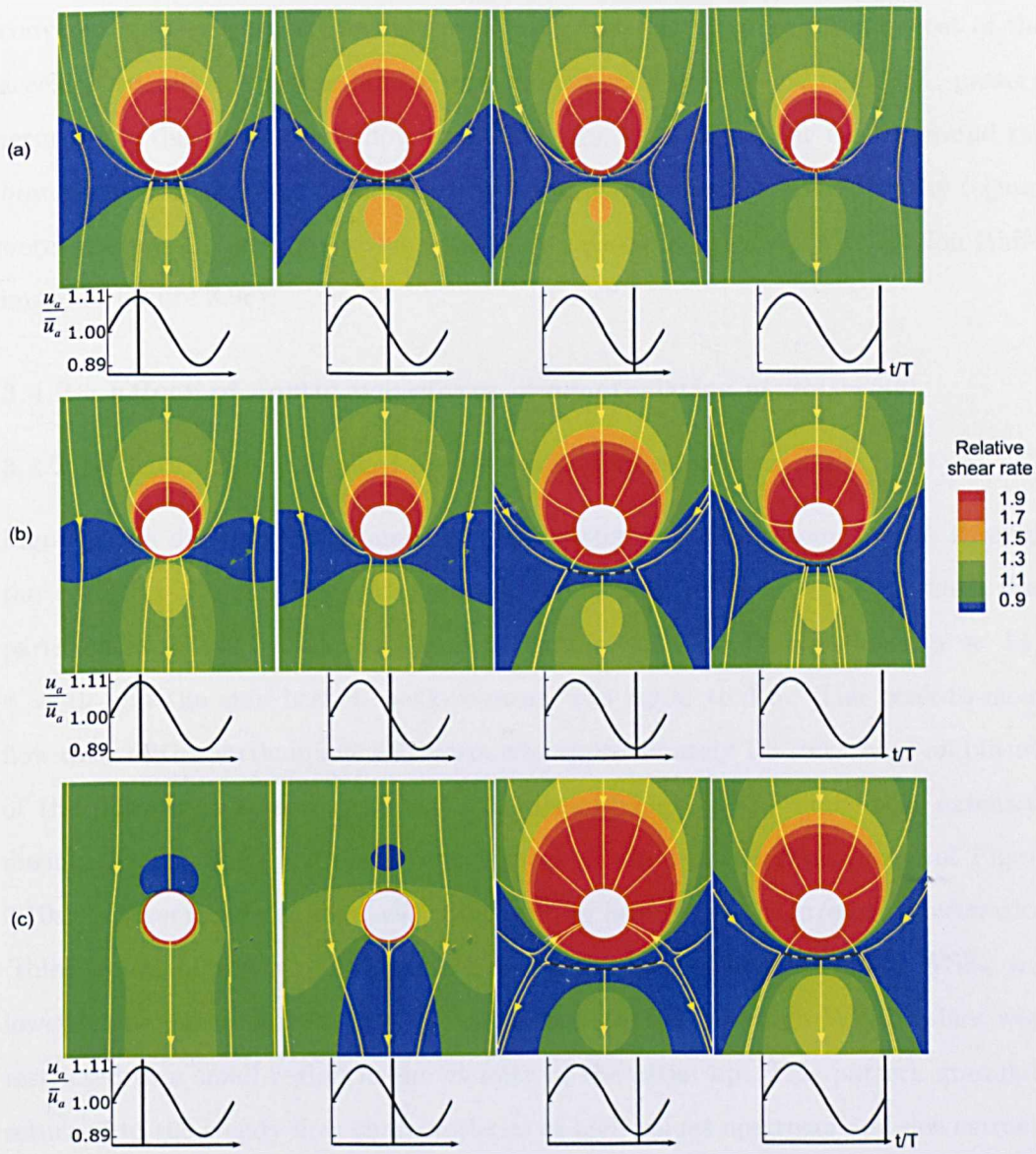

Figure 3.9: Magnitude and direction of non-dimensionalised instantaneous aortic wall shear stress for the simple geometry of Figure 3.1a. The simulations were performed for $Re_m = 150$, $Q_b{:}Q_{a_m} = 0.79\%$ and $U_{red} = 4$ (St $= 0.25$ or $\alpha \approx 7.7$). The side branch flow waveform had a phase shift with the aortic waveform of (a) $\phi = 0$, (b-c) $\phi = \pi$. In (c) the side branch flow was reversing for about one third of the cycle. Mean aortic flow is from top to bottom. Dashed lines indicate flow stagnation.

ther upstream. In addition, a streak of low WSS_n values appeared immediately downstream of the ostium, and the high values surrounding the lip were shifted laterally. Surface streamlines slightly diverged in the upstream and lateral regions, and

converged in the downstream region. During late deceleration and for most of the acceleration phase, the side branch flow was forward-moving and the WSS_n pattern returned to the quasi-steady flow characteristics, with high-shear values around the branch, as well as upstream and downstream, and low values laterally. The regions were substantially enlarged in size during late deceleration/early acceleration (third image of Figure 3.9c).

3.4.2 Effect of aortic waveform characteristics at Re_m=500

3.4.2.1 More physiological aortic peak-to-mean flow ratio

Figure 3.10a displays instantaneous WSS_n patterns at four discrete times through the cycle for a mean Reynolds number of 500 and an average side branch flow partition of 0.79%. U_{red} was equal to 4 (equivalent to St = 0.25 or $\alpha \approx 14$), $\phi = 0$, and the side branch peak-to-mean was equal to 1.5. The peak-to-mean flow ratio of the aortic inflow waveform was approximately 1.5 (increased amplitude of the pulsating pressure gradient). Regions of high WSS_n were most extensive during the middle of the deceleration phase of the cycle (second image of Figure 3.10a). Reversal of the near-wall fluid during late deceleration/early acceleration (third image of Figure 3.10a) produced a different pattern, in which WSS_n was lowest in regions upstream and downstream of the ostium; high WSS_n values were restricted to a small region in the vicinity of the ostial lip. This pattern gradually returned to the steady flow characteristics of high values upstream and downstream of the branch, and low values at the sides, late in the acceleration phase (left-hand image in Figure 3.10a). During most of the cycle, the upstream surface streamlines converged towards the branch and diverged downstream. However, during reversal of the aortic near-wall fluid, at the end of the deceleration phase, the streamline pattern was reversed. Streamlines converged towards the branch but in the opposite direction. Flow stagnation lines were observed downstream of the ostium during late acceleration and mid-deceleration but were absent during late deceleration/early acceleration.

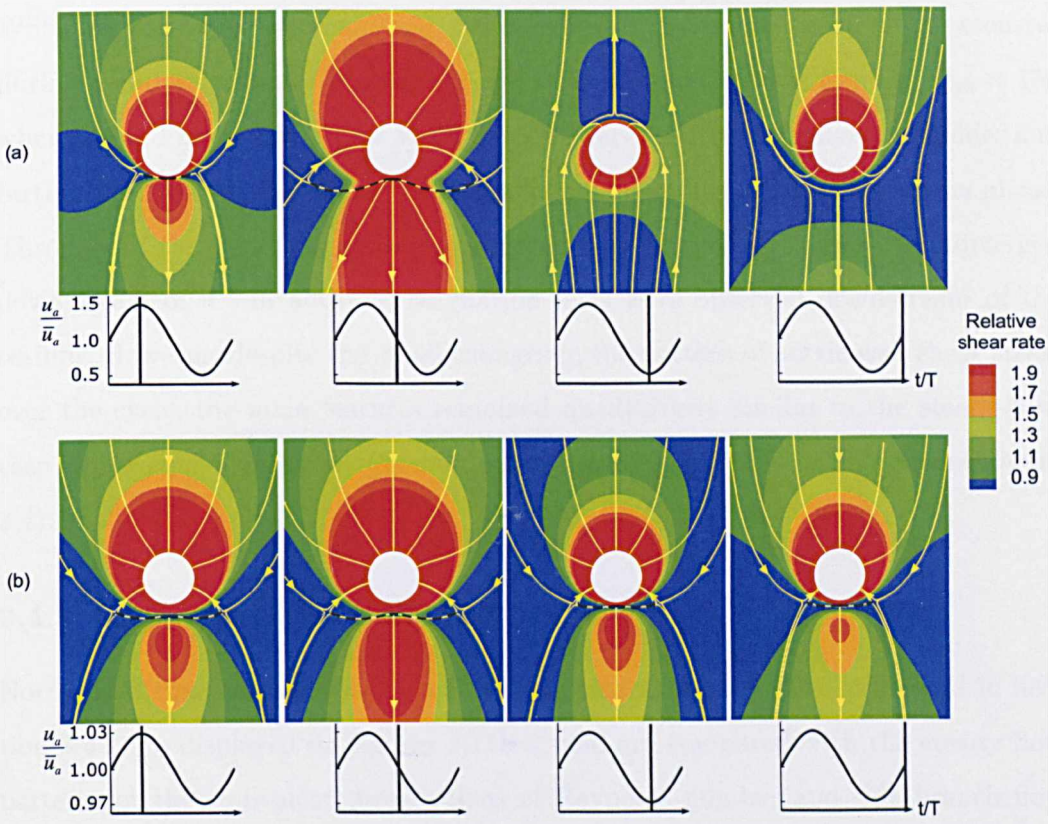

Figure 3.10: Magnitude and direction of non-dimensionalised instantaneous aortic wall shear stress for the simple geometry of Figure 3.1a. The simulations were performed for $Re_m = 500$, $Q_b{:}Q_{a_m} = 0.79\%$, $U_{red} = 4$ (St = 0.25 or $\alpha \approx 14$) and $\phi = 0$. The aortic waveform had a peak-to-mean of (a) 1.5 and (b) 1.03. Mean aortic flow is from top to bottom. Dashed lines indicate flow stagnation.

3.4.2.2 Reduced aortic peak-to-mean flow ratio

By reducing the aortic peak-to-mean flow ratio to approximately 1.03 (same pressure gradient as for Re_m=150), the WSS_n patterns were modified as shown in Figure 3.10b. The other flow conditions were held at the same values as in the previous case, that is, $Re_m = 500$, $Q_b{:}Q_{a_m} = 0.79\%$, $U_{red} = 4$ (or St = 0.25, or $\alpha \approx 14$), $\phi = 0$, and side branch peak-to-mean=1.5. Regions of high WSS_n upstream and around the ostium were lowest in size during the late deceleration/early acceleration phase of the cycle (third image of Figure 3.10b), however regions of high shear downstream of the ostium were lowest during mid-acceleration (fourth image of Figure 3.10b). High

WSS_n regions both upstream and downstream of the branch were most extensive during mid-deceleration. (Similar effects at this time-point were seen for $Re_m = 150$ when $\phi = 0$, Figure 3.9a.) Low WSS_n regions were greatly extended at the sides and further upstream at the end of the deceleration/beginning of the acceleration phase. Throughout the cycle, streamlines converged upstream of the branch, and diverged downstream of it. In addtion, stagnation lines were observed downstream of the ostium. However, despite the small changes in the pattern of aortic wall shear stress over the cycle, the main features remained qualitatively similar to the steady-flow case for the equivalent mean Re and Q_b:Q_a (third image in the bottom row of Figure 3.4).

3.4.3 Time-averaged wall shear stress

Normalised time-averaged wall shear stress patterns for the cases presented in Section 3.4.1 are displayed in Figures 3.11b-d, and are compared with the steady flow pattern for the equivalent mean values of Reynolds number and side branch flow partition (Figure 3.11a). The time-averaged WSS_n patterns were similar in character to the steady flow result, with elevated WSS_n values around the ostial lip and upstream; and low values laterally to the orifice. The patterns of Figures 3.11b and 3.11c were almost identical to the steady-flow result, and were only slightly different from the pattern for reversing side branch flow (Figure 3.11d). In the latter, the high shear region downstream of the branch was absent.

For the cases examined in Section 3.4.2, normalised time-averaged wall shear stress patterns are presented in Figures 3.12b-c. Figure 3.12a shows the steady flow pattern for $Re = 500$, Q_b:$Q_a = 0.79\%$. The time-averaged WSS_n results were similar in character to the steady flow pattern. For an aortic peak-to-mean ratio of 1.5 (Figure 3.12c), there were slightly more extended regions of high WSS_n upstream and downstream of the branch, while the streamline patterns were indistinguishable from the steady-flow result.

The results of Figures 3.11d and 3.12c demonstrate that the instantaneous changes in the WSS pattern during the cycle (in particular, the occurrence of low WSS_n regions upstream and downstream of the branch ostium during reversal of aortic or

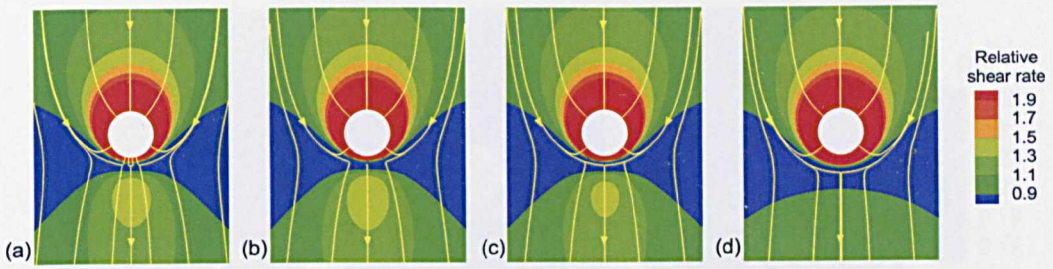

Figure 3.11: Magnitude and direction of non-dimensionalised time-averaged aortic wall shear stress for $Re_m = 150$, $Q_b{:}Q_{a_m} = 0.79\%$ and $U_{red} = 4$, corresponding to the instantaneous patterns of Figure 3.9. (a) Steady flow result at the same mean flow values. The side branch flow waveform had a phase shift, with respect to the aortic waveform, of (b) $\phi = 0$, (c-d) $\phi = \pi$ and in (d) it was reversing for about one third of the cycle. Mean aortic flow is from top to bottom.

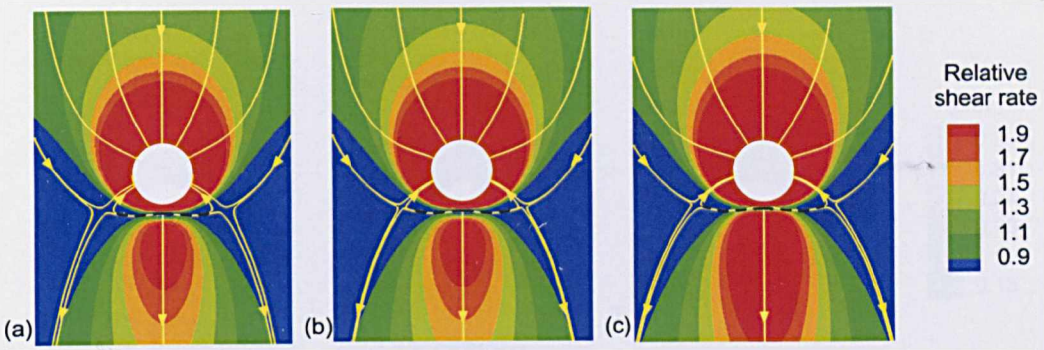

Figure 3.12: Magnitude and direction of non-dimensionalised time-averaged aortic wall shear stress for $Re_m = 500$, $Q_b{:}Q_{a_m} = 0.79\%$, and $U_{red} = 4$ ($\phi = 0$), corresponding to the instantaneous patterns of Figure 3.10. (a) Steady flow result at the same mean flow values. The aortic waveform had a peak-to-mean of (b) 1.03 (Figure 3.10b) and (c) 1.5 (Figure 3.10a). Mean aortic flow is from top to bottom.

side branch flow) had little influence on the time-averaged WSS_n patterns. This is explained by the magnitude of the lower WSS_n values (which characterise the low shear regions during reversing flow) being proportionally small compared to the much higher WSS_n values seen upstream and downstream of the branch for non-reversing flow.

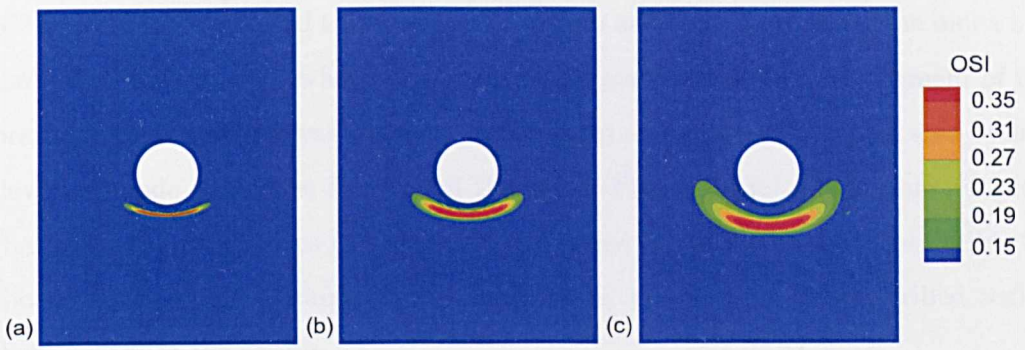

Figure 3.13: Oscillatory shear index for $Re_m = 150$, Q_b:$Q_{a_m} = 0.79\%$ and $U_{red} = 4$, corresponding to the instantaneous and time-averaged WSS patterns of Figures 3.9 and 3.11. The side branch flow waveform had a phase shift, with respect to the aortic waveform, of (a) $\phi = 0$, (b-c) $\phi = \pi$ and in (c) it was reversing for about one third of the cycle. Mean aortic flow is from top to bottom.

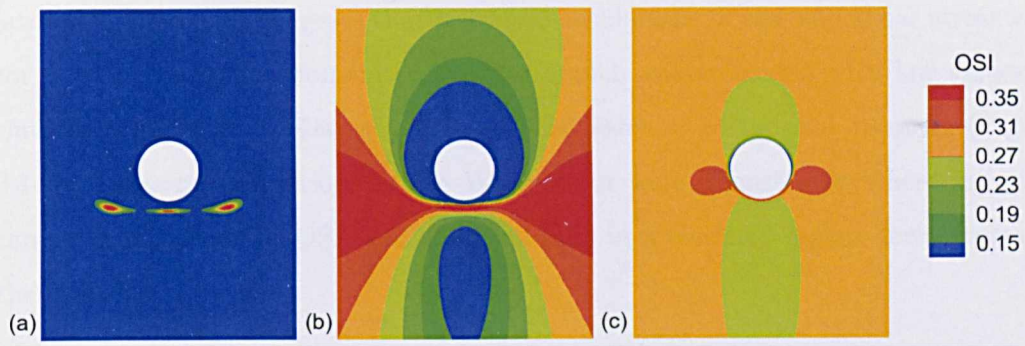

Figure 3.14: Oscillatory shear index for $Re_m = 500$, Q_b:$Q_{a_m} = 0.79\%$ and $U_{red} = 4$ ($\phi = 0$), corresponding to the instantaneous and time-averaged patterns of Figures 3.10 and 3.12, respectively. The aortic waveform had a peak-to-mean of (a) 1.03 (Figure 3.10b) and (b) 1.5 (Figure 3.10a). (c) Oscillatory shear index for a lower average flow division Q_b:$Q_{a_m} = 0.08\%$ (at $Re_m = 500$, aortic peak-to-mean=1.5, side branch peak-to-mean=1.5 and $\phi = 0$; instantaneous and time-averaged results are not shown). Mean aortic flow is from top to bottom.

3.4.4 Oscillatory shear index

Maps of oscillatory shear index (OSI) for the cases of Section 3.4.1 are displayed in Figures 3.13a-c. OSI, defined in Equation (3.15), is a description of the oscillation

of the wall shear rate and takes values between 0 and 0.5. In all cases, the index had low values almost everywhere except in a circumscribed region downstream of the branch ostium where it was elevated. This region was greatest when the side-branch flow was made to reverse for part of the cycle (Figure 3.13c). The results suggest that temporal oscillations of the wall shear stress vector were largely negligible for the flow conditions examined in all three cases, except in a circumscribed region downstream of the ostium.

Figures 3.14a and b show patterns of oscillatory shear index for the results presented in Section 3.4.2. For an aortic peak-to-mean of approximately 1.5 (Figure 3.14b), for which there was reversal of the near-wall fluid during the late deceleration/early acceleration phase of the cycle, the oscillatory shear index had a pattern which was almost the negative image of the time-averaged result (Figure 3.12c), with low values around the branch, upstream and downstream, and elevated values laterally. The result suggests that temporal oscillations of the wall shear stress vector were greatest in regions lateral to the branch and coincided with low values of time-averaged WSS_n. However, for a reduced value of aortic peak-to-mean (Figure 3.14a), temporal oscillations of the WSS vector were almost everywhere insignificant. Slightly elevated OSI values existed only in a confined region downstream of the branch.

Figure 3.14c presents the oscillatory shear index pattern for a lower average flow division of Q_b:Q_{a_m} = 0.08% (at Re_m = 500 and with an aortic peak-to-mean of 1.5, a side branch peak-to-mean of 1.5 and $\phi = 0$; instantaneous and time-averaged results are not shown). OSI remained elevated lateral to the branch and reduced upstream and downstream of it. However, its overall magnitude was reduced and the lateral regions of elevated OSI moved next to the branch mouth (compared to the slightly downstream lateral regions at Q_b:Q_{a_m} = 0.79%). This can be understood from the steady flow results of Figure 3.4 (third column, for Re=500), where decrease of the branch flow partition resulted in reduction or cancellation of the stagnation region downstream of the branch, allowing thus the lateral regions of elevated OSI (in the unsteady case) to move upstream, adjacent to the ostial lip.

3.5 Discussion

We used computational fluid dynamic techniques to examine the effect of Reynolds number, Re, and flow partition, Q_b:Q_a, on aortic WSS around the origins of intercostal arteries. The study was motivated by the observation that the pattern of atherosclerosis, putatively a shear-dependent disease, varies between species and with age at this site. We wished to determine whether patterns of WSS can also vary. The values of Re that we studied are appropriate for species ranging from mice to people (Buchanan Jr. et al., 1999; Feintuch et al., 2007; Shahcheraghi et al., 2002). Flow partitions have not been measured accurately at intercostal branch sites in any species. Further, there is disagreement as to whether flow in general partitions according to the square or the cube of the ratio of vessel diameters (Cheng et al., 2007), which would correspond to Q_b:Q_a = 1% or 0.1%, respectively, for the models examined in the present study. Partitions will certainly vary with physiological demand and may also depend on species and ages. We therefore investigated a wide range encompassing or closely approaching these values. Our main finding was that the pattern of WSS is highly dependent on Reynolds number and flow partition.

The fundamental features of the flow underlying the different patterns of WSS_n shown in Figure 3.4 can be elucidated by computing streamlines along the midplane of the aortic channel (Figure 3.15) and by computing streamtubes of fluid moving into the branch (Figure 3.16). To obtain the streamtubes, a ring of fluid particles at a distance $2D$ down the branch and with a diameter of $0.8D$ was traced backwards into the aorta to examine its origins (Coppola et al., 2001). (Figure 3.16 includes simulations at higher values of Re and Q_b:Q_a than in Figure 3.4 to confirm the trend in their effects on the streamtube. Perspective views of the streamtubes are shown on the right side of the figure.)

These figures show that increasing Reynolds number causes fluid to enter the branch from regions closer to the aortic wall, where it will be flowing relatively slowly. For example, the streamline which divides the fluid entering the branch from that continuing down the aorta moves towards the aortic wall (Figure 3.15). At the higher Re, fluid particles in the mainstream have too much inertia to enter the branch; in-

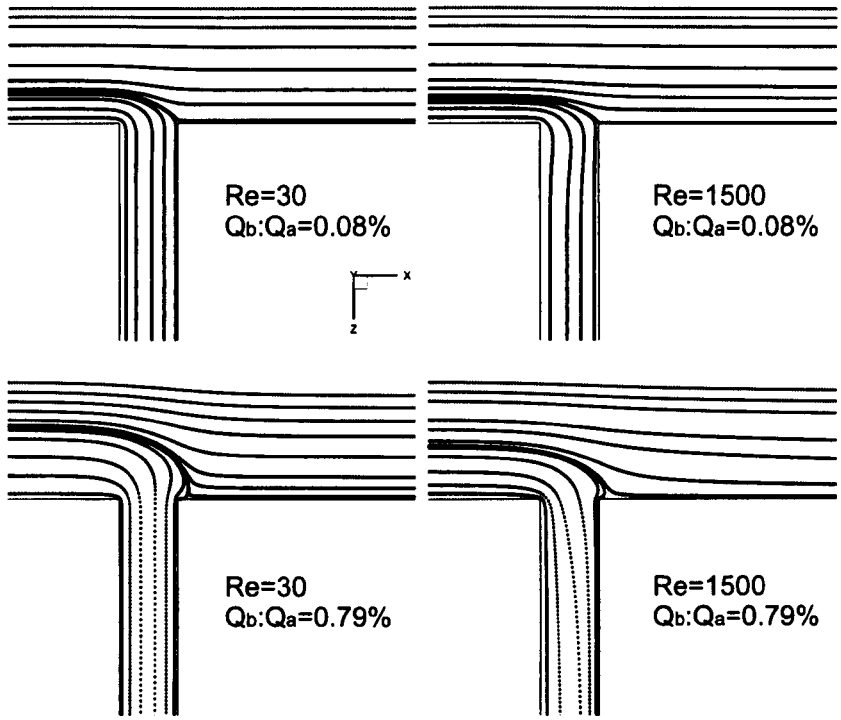

Figure 3.15: Streamlines along the mid-plane of the domain for the simple model of Figure 3.1a (Steady flow). The four panels correspond to the four combinations of highest and lowest Re and Q_b:Q_a in Figure 3.4. Mean aortic flow is from left to right.

stead, particles nearer the wall and from a wider area do so (Figure 3.16a), leading to a greater influence of the branch on WSS around the ostium. The inability of mainstream fluid particles to enter the branch explains the development of a stagnation line downstream of the ostium at higher values of Re and Q_b:Q_a (see last two rows of Figure 3.4).

Increasing the flow partition Q_b:Q_a necessarily increases the cross-sectional area of the streamtube in the aorta. However, these streamtubes remain similar in shape to the smaller ones seen at lower Q_b:Q_a (Figure 3.16b), explaining why greater flow into the branch intensifies and enlarges some features of the WSS patterns (columns of Figure 3.4) but does not fundamentally alter the flow physics. Additionally, the need for more fluid to enter the branch changes streamlines along the midline: fluid particles overshoot the branch mouth before entering it (Figure 3.15), explaining

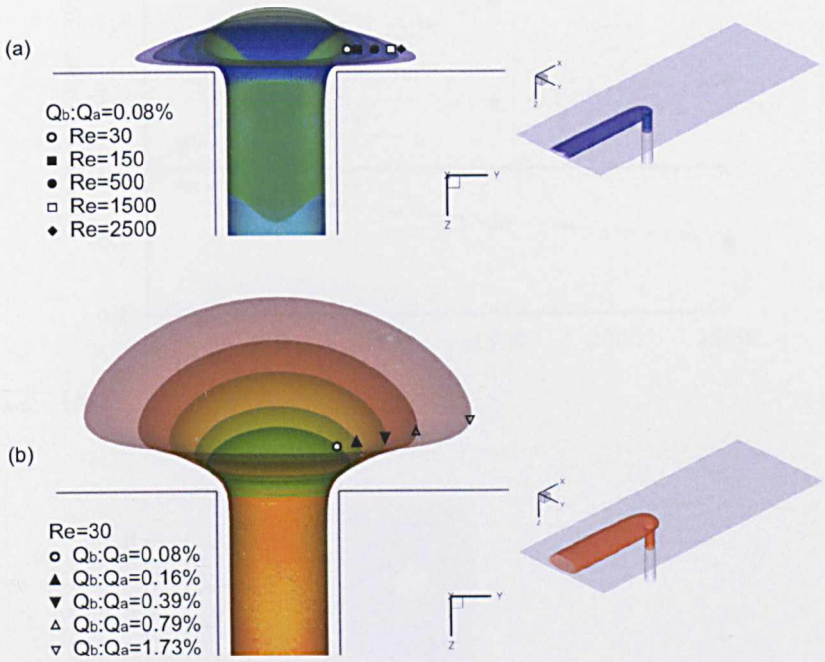

Figure 3.16: Computed streamtubes of fluid entering the branch (Steady flow). (a) Effect of increasing Re at Q_b:Q_a = 0.08% (Re = 30, 150, 500, 1500, and 2500). (b) Effect of increasing Q_b:Q_a at Re = 30 (Q_b:Q_a = 0.08%, 0.16%, 0.39%, 0.79%, and 1.73%). Perspective views of the streamtubes are shown on the right.

why the stagnation line (and probably also the lateral areas of low WSS_n) move downstream as Q_b:Q_a increases (columns of Figure 3.4). Although seemingly of minor importance, this property can lead to a shift from an increase to a decrease in WSS_n in regions immediately downstream of the ostium.

Figure 3.17 is a line graph showing the changes in WSS_n observed with increasing Re at Q_b:Q_a = 0.08% (Figure 3.17a), and with increasing Q_b:Q_a at Re = 30 (Figure 3.17b) in the simple geometry (Figure 3.1a). Maps of WSS_n are shown for these conditions in the top row and left column of Figure 3.4, respectively. In Figure 3.17, WSS_n is instead shown for three locations on the aortic wall: one side-branch

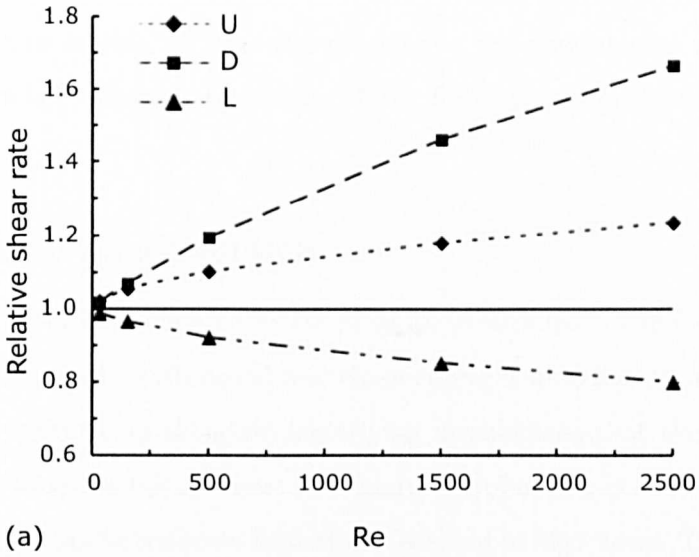

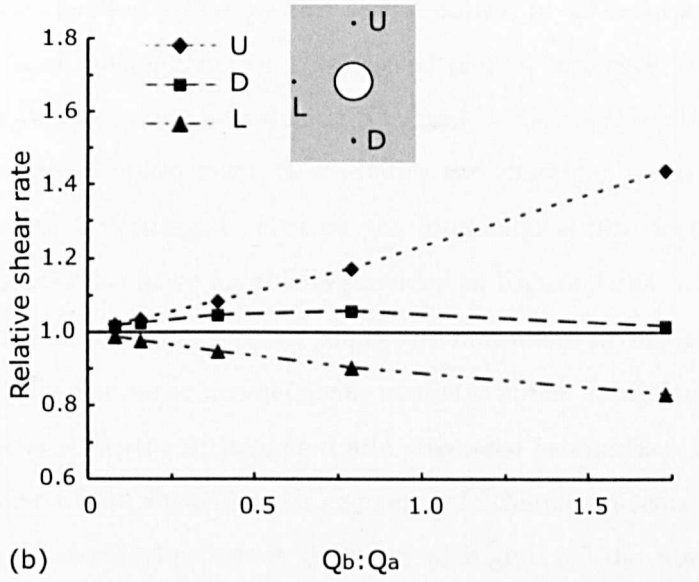

Figure 3.17: Change in normalised wall shear stress (WSS_n) with (a) Reynolds number (for Q_b:Q_a = 0.08%) and (b) flow partition (for Re = 30), measured at three locations on the aortic wall for the simple geometry of Figure 3.1a (Steady flow): at distances $1D$ upstream (U) of the ostial lip, $1D$ downstream (D) of it, and $1D$ lateral (L) to it (inset).

diameter (D) upstream of the ostial lip, $1D$ downstream of it, and $1D$ lateral to it. At the lowest Re and Q_b:Q_a, WSS_n was almost uniform around the branch and had a magnitude close to the inflow normalised value of 1 at all three locations. WSS_n

rose more rapidly downstream than upstream with increasing Re, but the opposite was seen with increasing Q_b:Q_a, where values in the downstream region rose only slightly before falling again. Increasing either Re or Q_b:Q_a decreased WSS_n lateral to the lip.

3.5.1 Simplifying assumptions

Re and Q_b:Q_a were systematically varied in an idealisation of the aorto-intercostal junction consisting of a cylindrical branch emerging from a flat plate. Using an idealised geometry can help elucidate underlying mechanisms that would be obscured or attributed to geometric features in a more complex model, but may also introduce artefacts or fail to replicate important facets of in vivo flows. The effects of the simplification were examined by computing flows at some combinations of Re and Q_b:Q_a after the idealised geometry had been modified by (i) incorporating a second branch to form an unstaggered or a staggered pair of branches, (ii) rounding the corners of the junction, (iii) introducing a curved aortic wall, or (iv) incorporating a realistically curved inflow tract, flow divider and daughter vessel. None of these modifications had a significant effect on the fundamental flow features or pattern of WSS. Additional evidence for this is provided in Figure 3.18a, which shows that similar patterns of streamlines occur along the mid-plane of the aortic channel in the simplified and the more geometrically realistic model of a single branch. The streamline patterns for the unstaggered and staggered geometries (Figures 3.18b-c) were also similar to the single branch geometry. It therefore seems reasonable that the use of the anatomically correct geometry of Figure 3.3 did not alter the main conclusions (Figure 3.8).

The model was additionally simplified by assuming Newtonian rheology. This assumption is widely used and has only modest quantitative effects on patterns of WSS at branches of large arteries; qualitative features of the pattern and of the fundamental flow are not affected (Perktold et al., 1991). Secondary flows emerging from the left ventricle or arising from the curvature and branches of the aortic arch were also ignored; they will have only a minor effect in the descending aorta, most likely by slightly skewing the branch-dependent effects.

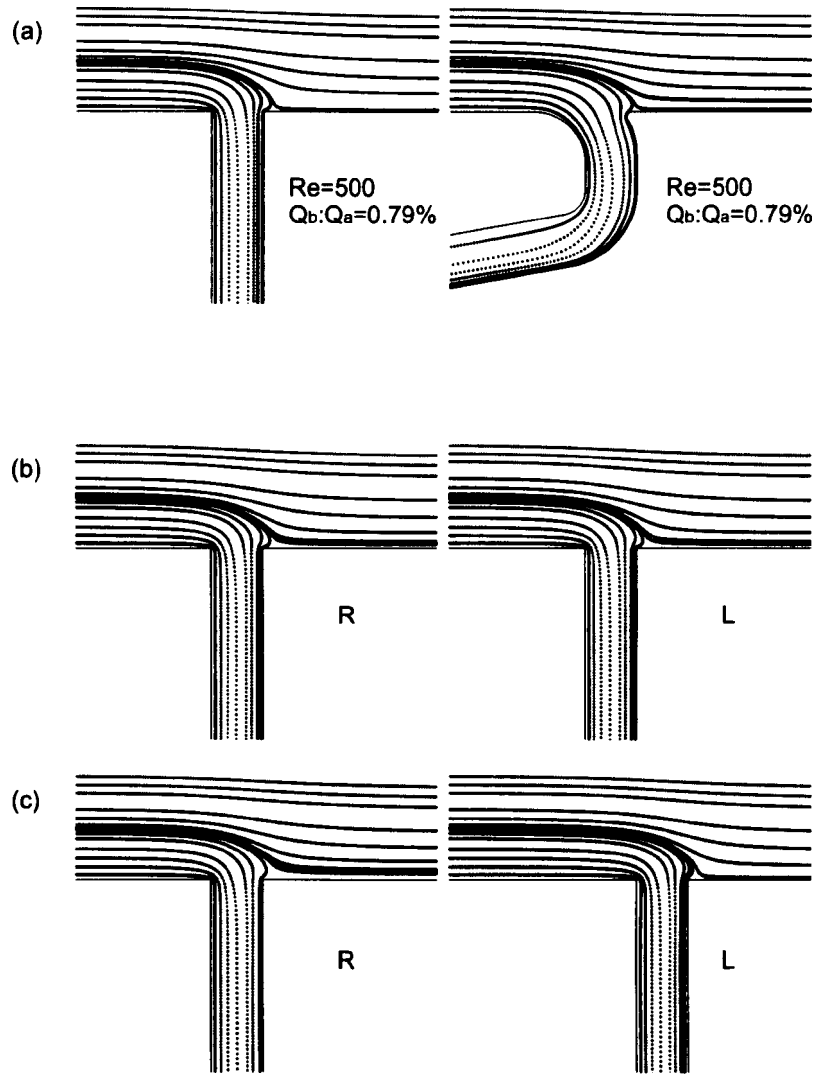

Figure 3.18: (a) Streamlines along the mid-plane of the domain in the simple model of Figure 3.1a (left) and the more realistic model of Figure 3.1c (right). Streamlines along planes crossing the centres of each of the side branches in (a) the unstaggered (Figure 3.1d) and (b) the staggered geometries. Right (R) and left (L) branches are given with respect to their anatomical position in a top-to-bottom direction of mean aortic flow. In all cases, simulations were performed for $Re = 500$ and $Q_b{:}Q_a = 0.79\%$ (Steady flow). Mean aortic flow is from left to right.

The most important simplification in the results of Section 3.3 was the assumption of steady flow. Some effects of unsteadiness are not considered significant. First, because of the long wavelength of pressure waves within the aorta (5-10 m; Milnor,

1979) and the small deformation of the aortic wall over each cardiac cycle (<10% change of aortic diameter), the velocity of radial wall motion is small compared to the radial flow components caused by the branch, and can be ignored. (This may be particularly true for intercostal branch points since they are situated in the dorsal thoracic aorta, which is tethered to the posterior chest wall. See Section 3.5.2.1 for a further discussion.) Second, changes in mean velocity during the cardiac cycle are sufficiently slow that the flow can be considered quasi-steady at each time point. This is best understood by using the Strouhal number, St, or its reciprocal, the reduced velocity parameter, U_{red}, as defined in Equation (3.9) (Sherwin and Blackburn, 2005). For people ($Re \approx 1500$, $\alpha \approx 15$) and rabbits ($Re \approx 500$, $\alpha \approx 8$), U_{red} is equivalent to $\sim$10 aortic diameters, or $\sim$100 intercostal branch diameters. Hence, flow near the branch is not dominated by unsteady phenomena and its character can be approximated by the steady flow result obtained at a value of Re appropriate for each part of the cardiac cycle.

However, some effects of unsteadiness could be significant. For example, the inlet velocities should be spatially distributed with a time-varying Womersley profile rather than the Poiseuille profile appropriate for fully-developed steady flow. The different distribution of inertia would affect the origin of the streamtube flowing into the branch. We therefore conducted an investigation of unsteady flow in the simple model geometry of Figure 3.1a, which was presented in Section 3.4. This investigation demonstrated that despite alterations in the pattern of WSS during the cardiac cycle, *mean* WSS_n patterns (Figures 3.11 and 3.12) are not significantly affected by the assumption of steady flow, at least for $U_{red} = 4$ (physically interpreted as the mean flow moving 40 intercostal diameters during one cardiac cycle, and equivalent to a Womersley parameter value of approximately 7.7 for $Re_m = 150$, and 14 for $Re_m = 500$). These values represent an upper bound of unsteadiness for the species and ages considered here.

Of course, endothelial cells may respond not only to mean WSS but also to derivatives of WSS. Several parameters of potential importance have been proposed, including the oscillatory shear index (OSI) and wall shear stress (spatial) gradient (WSSG) (Buchanan Jr. et al., 1999). We therefore investigated patterns of oscil-

latory shear index (Figures 3.13 and 3.14). It was demonstrated that for relatively small oscillations of the aortic waveform, the temporal oscillations of the wall shear stress vector became important only within a restricted region downstream of the branch, while upstream and lateral regions experienced almost unidirectional wall shear stress throughout the cycle. Reversal of the side branch flow did not alter significantly this pattern (Figure 3.13c). However, for larger peak-to-mean values of the aortic waveform, which resulted in reversal of the near-wall fluid within the aorta for part of the cycle, the oscillatory shear index was profoundly altered (Figure 3.14b). Temporal oscillations of the WSS vector were important almost everywhere around the branch. However, it was lateral to the branch that OSI was highest. The lowest values appeared upstream and downstream of the ostium. This pattern was almost the negative image of the time-averaged result (Figure 3.12c), suggesting that locations of lowest time-averaged WSS coincide with locations of highest OSI, and vice versa. Further understanding for this can be gained by examining pathlines along the mid-plane of the aortic channel at instantaneous time-points through the cycle, which will be discussed in the next section (see Figure 3.20).

3.5.2 Instantaneous variations

The effects of reversing side-branch and aortic near-wall flows on WSS were examined in the simple geometry of Figure 3.1a. These investigations were motivated by the work of Sloop et al. (1998), who measured Doppler ultrasound tracings of flow waveforms in the lower thoracic aorta and posterior intercostal arteries in human subjects of different ages. They demonstrated the existence of reversing (retrograde) flow in late systole/early diastole in both the thoracic aorta and intercostal arteries of healthy young men. This retrograde flow progressively vanished with age, and in subjects over the age of 36 both the thoracic aorta and posterior intercostal arteries were characterised by continuously forward-moving (antegrade) flow. The amplitude and frequency of the flow waveforms differed among the subjects of their study, but no detailed report was given for each subject. We are not aware of any other work reporting reversing flow in intercostal arteries. Here, we assumed aortic and side-branch flow waveforms oscillating at the same frequency at two moderate Reynolds numbers. We examined several cases, in which the aortic and side-branch flow waveforms had a phase shift of either $\phi = 0$ or $\phi \neq 0$, and either the side-branch

or the aortic near-wall flow waveform was reversing for part of the cycle.

Our main finding was that the instantaneous pattern of aortic WSS around intercostal ostia is greatly influenced by the existence of reversing side branch flow (Figure 3.9c) or reversing aortic near-wall flow (Figure 3.10a). For non-reversing flow, the effect of pulsatility was small and WSS_n only slowly fluctuated over the cycle. The patterns (Figures 3.9a-b and 3.10b) resembled in character those seen with steady flow at the equivalent mean Reynolds and flow partition values.

To understand the mechanisms underlying the WSS_n patterns obtained under reversing flow, lines along the mid-plane of the aortic channel were computed at instantaneous time-points through the cycle. Figure 3.19 displays lines tangent to the instantaneous velocity vectors for the case of reversing side branch flow ($Re_m = 150$, Q_b:$Q_{a_m} = 0.79\%$, $\phi = \pi$, and $U_{red} = 4$). A jet of fluid particles from the branch (first image of Figure 3.19) entered the aorta impeding the upstream flow from moving downstream. This explains the formation of the low WSS_n region seen immediately upstream of the ostium (first image of Figure 3.9c). At the next time-point, the jet protruded further toward the core aortic flow. As a result, the upstream low shear region was shifted further upstream, and another low WSS_n region was formed downstream of the branch which extended into a streak of low values (second image of Figure 3.9c). For forward-moving side-branch flow (last two images of Figure 3.19), the line patterns resembled those seen for steady flow for equivalent mean Reynolds number and flow partition.

The patterns of lines tangent to the instantaneous velocity vectors for partially backward-moving aortic near-wall flow are shown in Figure 3.20 ($Re_m = 500$, Q_b:$Q_{a_m} = 0.79\%$, $\phi = 0$, and $U_{red} = 4$). From early- to mid-deceleration (first two images of Figure 3.20), aortic flow moved into the branch from regions away from the wall. Despite the significant difference in the size of the instantaneous high WSS_n regions around the ostium between these two times (first two images of Figure 3.10a), the line patterns were almost identical; the line which divides the fluid entering the branch from that continuing down the aorta moved further away from the aortic wall but by a negligible amount. During the end of the deceleration/be-

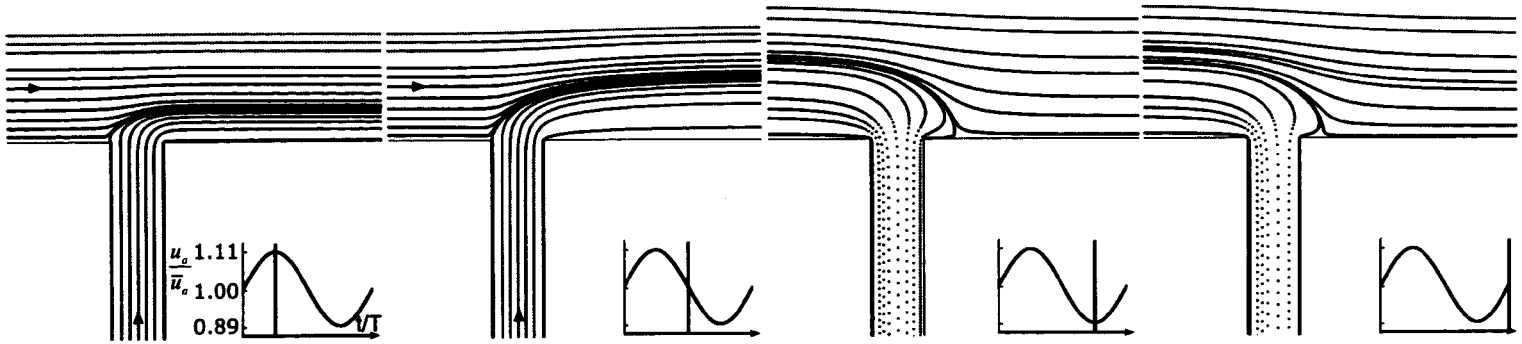

Figure 3.19: Lines tangent to the instantaneous velocity vectors along the mid-plane of the simple single-branch domain for continuously forward-moving aortic flow and partially backward-moving side branch flow (gray lines). $Re_m = 150$, Q_b:$Q_{a_m} = 0.79\%$, $\phi = \pi$, and $U_{red} = 4$. Arrows indicate flow direction. Mean aortic flow is from left to right.

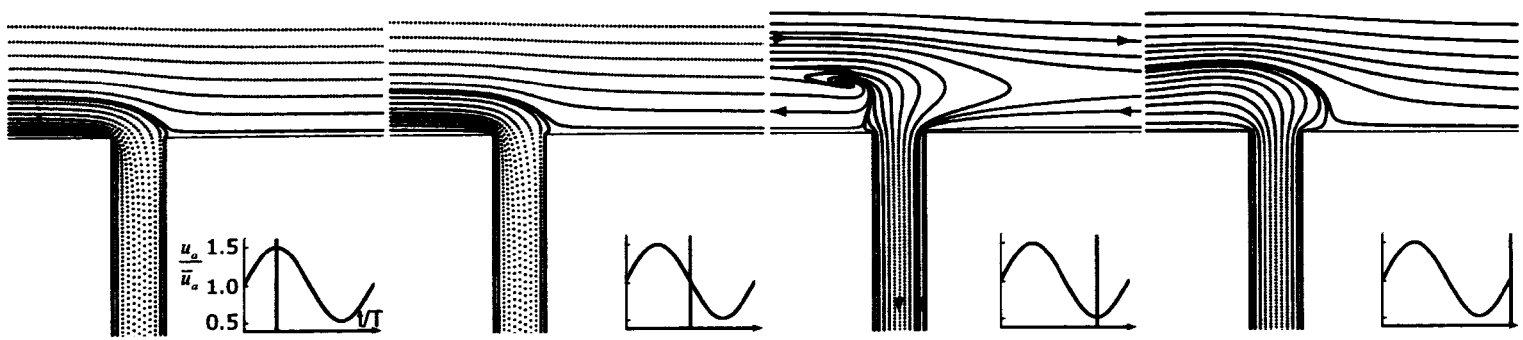

Figure 3.20: Lines tangent to the instantaneous velocity vectors along the mid-plane of the simple geometry (Figure 3.1a) for partially backward-moving aortic near-wall flow (gray lines) and continuously forward-moving side branch flow. $Re_m = 500$, Q_b:$Q_{a_m} = 0.79\%$, $\phi = 0$, and $U_{red} = 4$. Arrows indicate flow direction. Mean aortic flow is from left to right.

ginning of the acceleration phase (third image of Figure 3.20), the line pattern was profoundly altered. Aortic fluid particles near the wall were flowing in the opposite direction to fluid particles further away from the wall. In the region downstream of the branch (with respect to the direction of the core aortic flow), reversing near-wall fluid moved in the upstream direction and entered the branch. Upstream of the branch, fluid particles close to the wall also moved further upstream (in the opposite direction to adjacent particles of the bulk flow) causing the formation of a small vortex at a location above and upstream of the branch mouth where particles from the bulk aortic flow deviated from the axial direction to enter the branch. Aortic flow entered the branch from regions away from the wall. During the middle of the acceleration (last image of Figure 3.20), aortic near-wall flow moved again downstream and into the branch, but the line pattern was slightly deformed.

Returning to the discussion of the previous section on the pattern of oscillatory shear index for this case (Figure 3.14b), it can be seen that despite the reversal of the near-wall fluid during late deceleration/early acceleration, the aortic flow continued to enter the side branch at all times. The need for flow to enter the branch required fluid to be drawn from regions downstream of and lateral to the ostium, in addition to regions further away from the wall (from the bulk aortic flow). The deviation of the WSS vector from the axial direction lasted for longer time during the cycle in the lateral regions rather than in the downstream and upstream regions (as seen from the orientation of the instantaneous surface streamlines in Figure 3.10a). Temporal oscillations of the WSS vector were, therefore, greater lateral to the ostium (elevated OSI) than upstream and downstream of it (reduced OSI).

A number of simplifications were made in our simulations and analyses: we assumed simplified pulsatile flow waveforms, a Newtonian fluid and a flat, rigid, and fixed aortic wall. Further, we limited our investigation of the effects of unsteady flow to a moderate range of average Reynolds numbers and flow partitions, and examined only a few flow waveform characteristics. Clearly, relaxing these assumptions would increase complexity. However, some fundamental features of the flow which underlie the disparate patterns of WSS were explained, particularly those for reversing side-branch and aortic near-wall flows. More complex systems are expected to include

such features.

3.5.2.1 Oscillating walls

In all models presented in this work, the walls were assumed to be rigid and fixed. Under physiological flow conditions, however, the aortic walls undergo some degree of deformation. Secomb (1978) has analysed the two-dimensional flow in a channel of infinite ends whose walls are rigid and oscillate sinusoidally normal to their surface. For the simple single-branch geometry that we examined here, this motion could be expressed as:

$$z(t) = \pm 5D(1 + \epsilon \cos \omega t) \tag{3.16}$$

where $\epsilon \ll 1$. Assuming that the transverse velocity (for our case w_a^w) is independent of x (the axial direction), Secomb (1978) showed that the axial velocity u_a^w is linear in x (the pressure gradient is quadratic), that is:

$$u_a^w(x, z, t) = u_a^o(z, t) + x u_a^1(z, t) \tag{3.17}$$

where u_a^o is the axial flow which, although influenced by u_a^1 and w_a^w, is driven by a longitudinal pressure gradient; u_a^1 is the flow driven by the oscillatory motion of the walls. The non-dimensional instantaneous volume flux across a cross-section (due to the wall motion alone) can be expressed as (Hydon and Pedley, 1993):

$$Q_a^1(x, t) = \frac{2\epsilon}{5D} x \sin \omega t \tag{3.18}$$

Secomb (1978) examined various Womersley numbers for a small displacement of the wall. By choosing a frame of reference in which the channel walls were fixed, the variables were expanded in powers of ϵ. Secomb (1978) examined this type of flow also within an axisymmetric tube, while O'Dea and Waters (2006) extended this analysis to include circumferential oscillations. The effects of such wall motions on the profile of the mean axial streaming velocity appeared to be restricted to the near-wall region, although for high values of Womersley numbers and large displacements the effects extended further across the channel (or tube). For the flow regimes studied in this work and particularly for the thoracic aorta, which is tethered to the posterior chest wall, we expect these effects to be small, at least for time-averaged WSS patterns.

3.5.3 Comparison with other studies

A number of authors, in seeking to explain the particularly frequent occurrence of lesions downstream of aortic side branches in cholesterol-fed animals (Fry, 1969; Cornhill and Roach, 1976), or the low frequency of human atherosclerosis at these locations (Caro et al., 1971), have speculated that this is an area of particularly high WSS. However, Sobey (1977a,b) and Tutty (1988), under the assumption of Stokes flow, showed for the two- and three-dimensional case, respectively, that WSS is elevated upstream of small branch orifices as well as downstream of them. Our results are in good agreement with their analyses at similar values of Re and Q_b:Q_a but at other values we found different patterns, involving the occurrence of relatively low WSS at the sides of branches when Re is elevated and downstream of branches when Q_b:Q_a is elevated.

WSS has also been computed in models of the origin of the coeliac artery (Buchanan Jr. et al., 1999; Cheer et al., 1998). This branch is not strictly analogous to the one studied here, since the daughter vessel is comparable in size to the aorta (with a flow partition approaching 50%) and does not form part of a pair. Furthermore, although effects of Re and Q_b:Q_a have been investigated individually (Cheer et al., 1998), their interactions have not been studied. Nevertheless, a number of the features and trends we identified can be discerned in the maps they present for this site.

Concerning results under the influence of pulsatile flow, Tuck (1970) and DeMestre and Guiney (1971) have previously examined unsteady flow through an orifice in a wall, which could also be applied to intercostal arteries. DeMestre and Guiney (1971) found that the flow is approximately quasi-steady for low Reynolds numbers. We have given evidence that in general is in agreement with their result by showing that the time-averaged WSS_n patterns, produced for moderate Reynolds numbers (namely 150 and 500), differed very little from the equivalent steady flow results.

Although the effect of pulsatile aortic inflow waveform on WSS has been previously investigated (e.g. Buchanan Jr. et al., 1999, for the coeliac artery), reversing side branch flow and its effect on aortic WSS distribution has not been studied. We have

demonstrated the existence of some new features in the wall shear stress patterns during side branch flow reversal, involving low WSS values upstream and downstream of the origin of the branch, and elevated values at the sides. During reversal of aortic near-wall fluid, other WSS features were observed. Most interestingly, the pattern of oscillatory shear index obtained for the case with reversing near-wall flow was very similar in character with the one presented by Buchanan Jr. et al. (1999) (whose model had a ratio of diameters ≈ 0.6, $Re_m \approx 220$, $Q_b{:}Q_{am} \approx 43\%$).

3.5.4 Physiological and pathological relevance

This study is part of a larger research programme to determine whether the differences in lesion distribution that occur between species and between ages within a species can be explained by differences in the pattern of WSS (or its spatial or temporal derivatives). Evidence for age- and species-related differences in WSS patterns has been obtained by examining endothelial morphology around branches. Endothelial cells and their nuclei align with the predominant flow direction and elongate with increasing shear. In young rabbits, endothelial nuclei are more elongated downstream of branches than upstream, but the reverse pattern is seen in mature rabbits (Al-Musawi et al., 2004). Nuclear shape is approximately the same upstream and downstream of branches in both immature and mature mice (Bond and Weinberg, 2006).

Figures 3.21a-c show patterns of aortic lesion frequency around intercostal ostia in apolipoprotein E/low density lipoprotein receptor double knockout mice (McGillicuddy et al., 2001), immature cholesterol-fed rabbits, and mature cholesterol-fed rabbits (Barnes and Weinberg, 1999), respectively. The comparatively uniform pattern of WSS_n we found for the lowest values of Re and $Q_b{:}Q_a$ (Figure 3.4, top left) correlates with the approximate circumferential uniformity of lesion frequency seen in mice of all ages (Figure 3.21a). Similarly, the WSS_n pattern found at relatively high values of Reynolds number and flow partition (e.g. for $Re = 500$, $Q_b{:}Q_a = 0.79\%$ in Figure 3.4) correlates with some features of the lesion pattern observed in mature rabbits (Figure 3.21c). This lesion map (for mature rabbits) can also be correlated with the oscillatory shear index pattern obtained for reversal of the aortic near-wall flow (Figure 3.14b), at $Re_m = 500$ and $Q_b{:}Q_{am} = 0.79\%$, although the lateral regions of

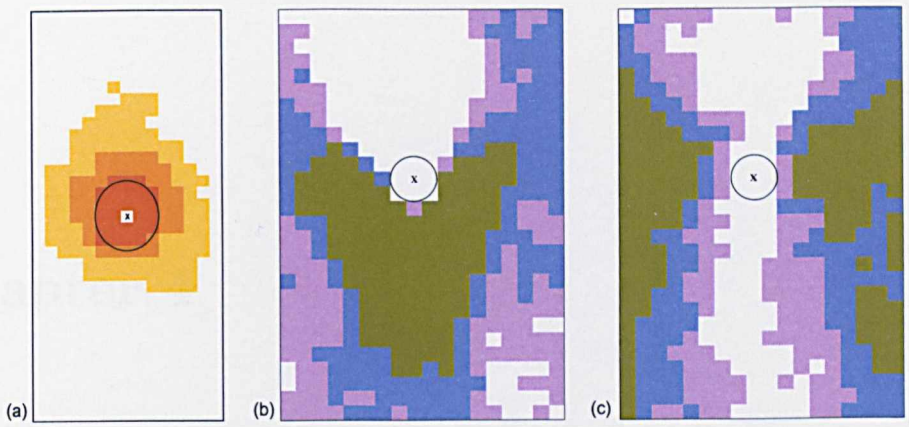

Figure 3.21: Patterns of lesion frequency around intercostal ostia (a) from 6 mice aged 16 to 20 weeks (after McGillicuddy et al., 2001), (b) from 6 young rabbits, 6 weeks old, and (c) from 5 mature rabbits of average age 27 months (after Barnes and Weinberg, 1999). Frequency increases with shading. Mean aortic flow is from top to bottom and X marks the centre of the ostium.

elevated OSI occur slightly downstream of the ostium. Reduction of the average flow partition to Q_b:$Q_{am} = 0.08\%$ moved these regions upstream, next to the lateral lips of the branch mouth (Figure 3.14c), but the OSI pattern was slightly decreased in magnitude and the lateral regions were reduced in size. Increase of Reynolds number (at this low flow partition) would increase OSI in the lateral regions and reduce it upstream and downstream of the branch (effect of Re, as it was seen in the opposite fashion in steady flow for WSS), and hence the pattern would possibly correlate better with the lesion pattern of mature rabbits. This also implies that regions of low WSS are associated with regions of increased oscillations of the WSS vector (elevated OSI), which both correlate with lesion locations around intercostal ostia of mature rabbits. However, we failed to find a pattern of WSS_n that correlates with the downstream pattern of lesions seen in immature rabbits (Figure 3.21b). Despite an apparent consensus, this work showed that many aspects of the relation between WSS and lesion occurrence remain obscure.

Chapter 4

Wall shear stress in the aortic arch

In this chapter, patterns of wall shear stress in the aortic arch and the proximal major branches are investigated within three anatomically correct geometries of wild-type mice and two approximated human geometries. An introduction for this study is given in Section 4.1. Section 4.2 briefly describes the reconstruction of the image-based models, the governing equations and boundary conditions used. Patterns of haemodynamic wall shear stress (WSS) for each geometry are presented in Section 4.3. Finally, Section 4.4 gives a discussion of the obtained results. The flow within the aortic arch is analysed in that section.

4.1 Introduction

Atherosclerotic lesions, which are distributed non-uniformly around curved regions and branching points in the arterial system, are thought to develop by mechanisms dependent on haemodynamic parameters, particularly shear stresses developed on the arterial wall. The current consensus relates atherosclerotic plaque localisation to low and/or oscillating wall shear stress. The large curvature and non-planarity of the aortic arch, and in addition the branching of three major arteries from its outer surface (greater curvature), makes the aortic arch one of the most susceptible to atherosclerosis arterial sites in mice (Nakashima et al., 1994) and humans (Mitusch et al., 1997). Its size makes it also experimentally accessible. The recent use

of genetically modified mice as models of atherosclerosis has contributed toward an understanding of the development of the disease in the aortic arch. However, there is no clear correlation—in terms of haemodynamics—between the two species, and a full characterisation of the haemodynamic environment of the mouse aortic arch is needed. Here, we investigate distributions of wall shear stress (WSS) in the mouse aortic arch and the proximal major branches in an attempt to clarify some of the above issues.

Nakashima et al. (1994) have reported the occurrence of lesions near the origins of major branches in apolipoprotein E-deficient mice, the lesions sharing many of the features seen in human plaques (see line graph of Figure 1.2 in Chapter 1). In addition, Johnson and Jackson (2001); McAteer et al. (2004) and Schneider et al. (2004) have demonstrated the development of vulnerable atherosclerotic plaques within the brachiocephalic (innominate) artery of apoE knockout (apoE-/-) mice. Won et al. (2007) have added to evidence for the development of lesions at the outer wall of the brachiocephalic artery with observations made in lipoprotein receptor-deficient (ldlr-/-) mice, in which lesions were also seen at the inner (lesser) curvature of the aortic arch.

Numerous studies, using experimental, analytical or computational methods, have attempted to analyse the haemodynamic environment in the aortic arch, or flow within curved pipes with application to the aortic arch; for example Shahcheraghi et al. (2002); Mori and Yamaguchi (2002); Jin et al. (2003); Suo et al. (2007); Feintuch et al. (2007), and Farthing (1978); Pedley (1980); Siggers and Waters (2008) (see also Chapter 1). However, there are several discrepancies among the results obtained from these studies, attributable to variability among geometries and subject-specific models or haemodynamic conditions, and only a few solid conclusions can be drawn; primarily that the distribution of shear stresses within the aortic arch is spatially heterogeneous. In this study, we used computational fluid dynamics methods to compute wall shear stresses in the aortic arch of the wild-type mouse (free of disease) and compare them with WSS distributions in the human arch. The simulations were performed assuming steady flow, since time-varying effects have recently shown insignificant differences between steady and time-averaged WSS for

Reynolds numbers characteristic of the mouse (Feintuch et al., 2007). Although the assumption of steady flow is a simplification, mouse-to-mouse anatomical differences and varying physiological conditions were examined for their effects on patterns of WSS in the neighbourhood of the aortic arch and the three major branches. The results complement to the characterisation of the haemodynamic environment in the mouse and human aortic arch, and contribute to the analysis of atherosclerotic plaque localisation in that arterial site.

4.2 Image-based computational models

4.2.1 Geometries

Three anatomically correct mouse geometries (Figure 4.1), which were reconstructed from magnetic resonance (MR) images, were used to study patterns of haemodynamic wall shear stress in the aortic arch (the MR images were generously provided by M.A. McAteer, J.E. Schneider, R.P. Choudhury, and K.M Channon, John Radcliffe Hospital, Oxford). The geometries included a portion of the ascending aorta, the aortic arch with the three major branches, and the proximal part of the descending thoracic aorta. Wild-type C57BL/6 mice (approximately ten weeks old) were imaged using an 11.7 T (500 MHz) MR system (vertical magnet - Bruker, Rapid Biomedical) as described in McAteer et al. (2004); Schneider et al. (2004); and Lygate et al. (2006), as part of control groups.

Geometry 1 (Figure 4.1a) is from a wild-type mouse (ten weeks old) perfusion-fixed after sacrifice with 4% paraformaldehyde in phosphate-buffered saline via the left ventricle (McAteer et al., 2004; Schneider et al., 2004). The aortic segment, attached to the heart and spine, was perfused with perflouropolyether via the left ventricle and was removed and placed in a 13-mm glass MR tube including agarose. The subject was scanned using high-resolution, multi-contrast MR imaging (MRI) with a three-dimensional (3D) multiecho sequence. The resulting high-resolution T_2-weighted images had a voxel size of 23 x 23 x 31 μm^3. A stack of 256 two-dimensional (2D) MR images (tiff, 16 bit) of size 512x512 pixels was obtained for the reconstruction of a 3D computational model.

Geometries 2 and 3 (Figures 4.1b and 4.1c, respectively) are from wild-type mice (24±3g body weight) from the control group of a study by Lygate et al. (2006). The mice were anaesthetised with isoflurane and imaged repeatedly within 24 hrs in a supine position using high-resolution in vivo cardiac MRI. The mice were maintained under anaesthesia at 1.5-2% isoflurane and their temperature and respiration were controlled (Schneider et al., 2003). For Geometry 2, the resulting stack of 64 2D MR images (bright-blood) had an in-plane resolution of 33.3 x 33.3 μm^2 and a thickness of 93.8 μm. For Geometry 3, the mid-ventricular, end-diastolic MR images had a voxel size of 33 x 89 x 33 μm^3 (192 slices).

Three-dimensional anatomically-correct computational models of the arterial geometries were generated using in-house reconstruction tools. The process is summarised in Figure 4.2 for Geometry 2 (for a detailed description of the methodologies, see Section 2.3 of Chapter 2). The vessel lumen was segmented on each slice plane using thresholding, and the resulting pixelated contours were smoothed by interpolation of least-square spline curves. For Geometry 1 (black-blood MR images), segmentation was performed using the Scion Image 1.63 (Scion) software. The zero iso-contour of an implicit function, interpolated through the spline curves, was used to represent the surface. An initial surface triangulation was carried out using the marching cubes algorithm, and the surface was smoothed using a non-shrinking algorithm (modified Taubin's smoothing algorithm, Giordana, 2004; Giordana et al., 2005b).

Segmentation of Geometry 3 originally included only short lengths of the proximal parts of the three major branches and the descending thoracic aorta. To avoid any influence of the outflow boundary conditions on the computed WSS patterns, straight flow extensions were added to the branches and the descending aorta using Rhinoceros®. The ascending aorta was also extended (by $2.5D_0$) and slightly enlarged (by D_e=$1.25D_0$) to ensure fully developed and non-reversing inlet flow (for Geometry 3, D_0 is the hydraulic diameter above the aortic root, measured at the point shown in Figure 4.1c, and is equal to approximately 1.6mm). Extensions were omitted in the other two geometries since the branches were sufficiently long (except for the left common carotid and left subclavian arteries in Geometry 1 which were left as segmented).

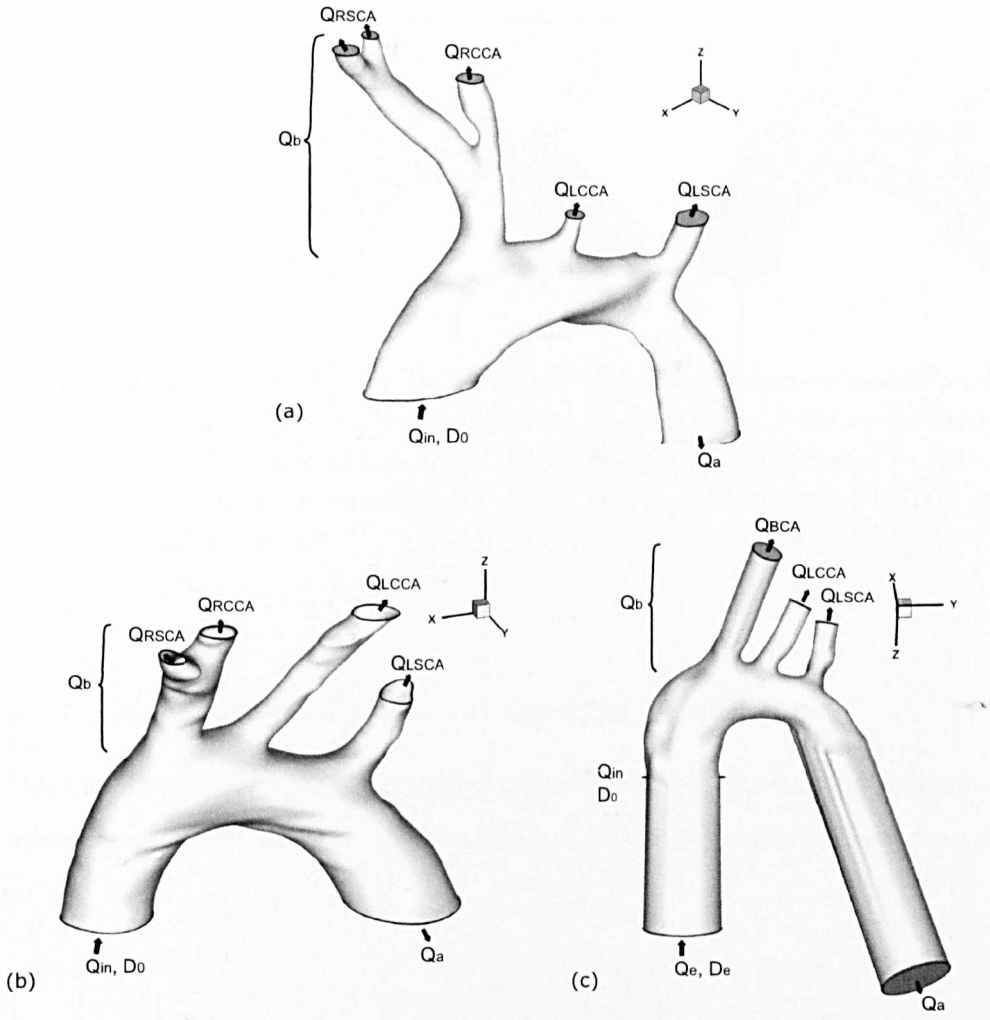

Figure 4.1: Image-based computational models of three wild-type mice scanned (a) ex vivo and (b-c) in vivo using high-resolution magnetic resonance imaging (MRI). In the latter geometry (c), straight flow extensions were added to the flow boundaries. In Geometry 1 (a), a crease on the surface around the bifurcation of the left subclavian artery and the descending aorta was an artefact due to local loss of the MRI signal (see Discussion). Q_{in} is the inlet blood flow rate, Q_b is the *combined* branch flow rate, and Q_a is the flow rate in the descending thoracic aorta. D_0 is the diameter of the ascending aorta above the aortic root. (Q_e, D_e in Geometry 3 are the flow rate and diameter, respectively, at the end of the aortic extension—see document). Q_{BCA}, Q_{LCCA} and Q_{LSCA} denote the flow rates in the brachiocephalic, left common carotid and left subclavian arteries, respectively. Q_{RSCA} and Q_{RCCA} denote flow rates in the right subclavian and right common carotid arteries, respectively.

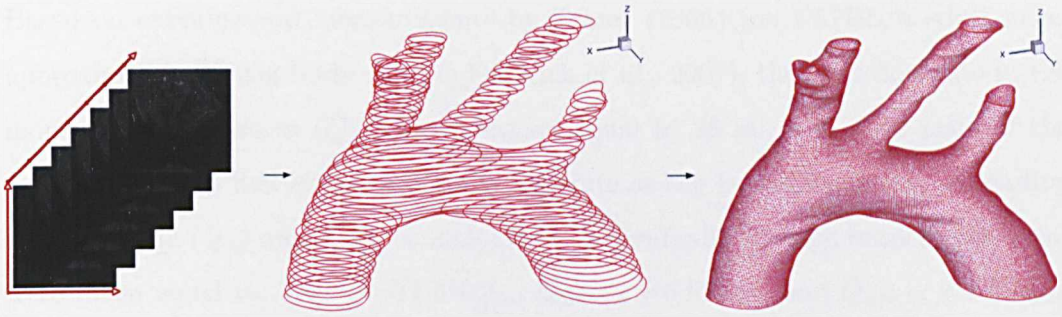

Figure 4.2: Reconstruction process of an anatomically correct mouse aortic arch (Geometry 2). The process involves segmentation of the vessel lumen from a stack of MR images (left), interpolation of spline curves (middle), and interpolation of an implicit surface (after smoothing and surface re-triangulation - right).

4.2.2 Numerical methods and boundary conditions

The time-independent Navier-Stokes equations of a Newtonian and incompressible flow were assumed. The flow is characterised by the Reynolds number, here defined as:

$$Re_{D_0} = \frac{\rho U D_0}{\mu} = \frac{4\rho Q_{in}}{\pi \mu D_0} \tag{4.1}$$

where U is the average inlet velocity, Q_{in} is the blood flow rate in the ascending aorta, and D_0 is the diameter of the ascending aorta above the aortic root. The fluid density, ρ, was assumed equal to 1030 kg/m^3 and the dynamic viscosity, μ, equal to 0.004 kg/m sec (Nguyen et al., 2008).

A plug (blunt) velocity profile was assumed to describe the blood flow at the aortic inlet of all three geometries (Shahcheraghi et al., 2002; Suo et al., 2007; Feintuch et al., 2007). Geometry 3 was additionally tested with a fully developed (parabolic) velocity profile. In all geometries, the aortic walls were assumed to be rigid and the no-slip condition was applied. Finally, a zero traction boundary condition was imposed on the outlet of the descending aorta.

Based on experimental measurements by Ethier (2005) (on C57BL/6 adult mice, approximately 20-25g body weight; Feintuch et al., 2007), the inlet flow rate in the mouse ascending aorta (Q_{in}) was assumed equal to 26 ml/min. The ratio of the *combined* branch flow rate (Q_b) to the flow rate at the boundary of the descending thoracic aorta (Q_a) was Q_b:Q_a = 22.8 : 77.2. Individually for each branch, flow rates were taken equal to: Q_{BCA} =11.4%Q_{in}, Q_{LCCA} =6.9%Q_{in} and Q_{LSCA} =4.5%Q_{in} (Ethier, 2005). For Geometries 1 and 2, the brachiocephalic artery split into 6.9%Q_{in} for the right subclavian artery (with equal splits into the two daughter branches for Geometry 1) and 4.5%Q_{in} for the right common carotid artery (RCCA). Geometry 3 was also examined for a different flow division, Q_b:Q_a = 30 : 70, in which Q_{BCA} : Q_{LCCA} : Q_{LSCA} = 15 : 8 : 7%Q_{in} (Feintuch et al., 2007). Effects of varying Reynolds number on the wall shear stress pattern were investigated for Geometry 3 by changing Q_{in}(=Q_e).

Furthermore, the two in vivo-scanned mouse geometries (Geometries 2 and 3) were scaled to an aortic diameter of D_0=30mm, which is typical for people (Feintuch et al., 2007), in order to examine effects of scaling of the Reynolds number. This is justified, knowing the various existing scaling laws that correlate WSS variations between the two species (Greve et al., 2006; Cheng et al., 2007; Weinberg and Ethier, 2007); however, it does not imply that direct scaling of a mouse geometry can approximate a real human geometry and the underlying flow features. The average inlet velocity (at D_0) was assumed equal to 17.5cm/s (Feintuch et al., 2007) for the approximated human geometry, resulting in an inlet flow rate of approximately 7.4 litres/min (slightly higher than the average 5 litres/min for healthy adults) and a Reynolds number (according to D_0) of approximately 1352.

For all geometries, hybrid meshes of prismatic and unstructured tetrahedral elements were created in Gambit, after surface re-triangulation. Prismatic boundary layer meshes were used at the walls of the geometries to enhance the modelling of viscous flows. A mesh of 518528 hybrid elements (156120 nodes) was used for Geometry 1. The mesh for Geometry 2 included 595027 tetrahedral and prismatic elements (162912 nodes), while that for Geometry 3 contained 332300 elements (79125 nodes). The flow field was solved using Fluent® 6.3 and a second-order upwind momentum

discretisation scheme with a second-order pressure scheme.

4.3 Results

Haemodynamic wall shear stress distributions for three different mouse aortas are presented in Figures 4.3-4.5 assuming equal inlet flow rates (Q_{in}) and flow divisions (Q_b:Q_a). WSS was normalised by the value that corresponds to a straight tube of diameter equal to that of the ascending aorta above the aortic root at the same mean flow rate. This can be expressed as $8\mu^2 Re_{D_0}/(\rho D_0^2)$ or $32\mu Q_{in}/(\pi D_0^3)$. Effects of varying Reynolds number and flow division on the wall shear stress distribution were examined for Geometry 3 (Figures 4.6 and 4.7, respectively). The effect of a fully developed (parabolic) inlet velocity profile on WSS within Geometry 3 is presented in Figure 4.8. Finally, Figure 4.9 shows WSS distributions in two approximated human geometries (scaled Geometries 2 and 3).

4.3.1 Geometry 1

Figure 4.3 shows the distribution of normalised wall shear stress (WSS_n) in the aortic arch and major branches of the ex vivo-scanned mouse geometry of Figure 4.1a (the side, top and bottom views of the geometry are displayed from top to bottom). The simulations were performed for Re_{D_0}=181.9 (Q_{in}=26ml/min, D_0 ≈0.8mm) and Q_b:Q_a=22.8 : 77.2 (Q_{RSCA} =6.9%Q_{in} with equal splits into the two daughter branches, Q_{RCCA} =4.5%Q_{in}, Q_{LCCA} =6.9%Q_{in} and Q_{LSCA} =4.5%Q_{in}).

WSS_n was highly heterogeneous throughout the geometry. Variations in the magnitude of WSS_n were larger along the outer (greater) curvature of the aortic arch than along the inner (lesser) curvature. WSS_n on the lateral walls of the aortic arch was patchy and asymmetrical between the ventral and dorsal walls (the dorsal wall is not shown in the figure), but rather moderate in magnitude. Along the greater curvature of the arch, WSS_n was highest on the flow dividers of the three branching arteries and lowest on the proximal (outer) walls of the branches. The proximal wall of the brachiocephalic (innominate) artery (BCA), which has been described as a location prone to the development of vulnerable atherosclerotic plaques in apolipoprotein E knockout (apoE-/-) and lipoprotein receptor-deficient (ldlr-/-) mice (Johnson and

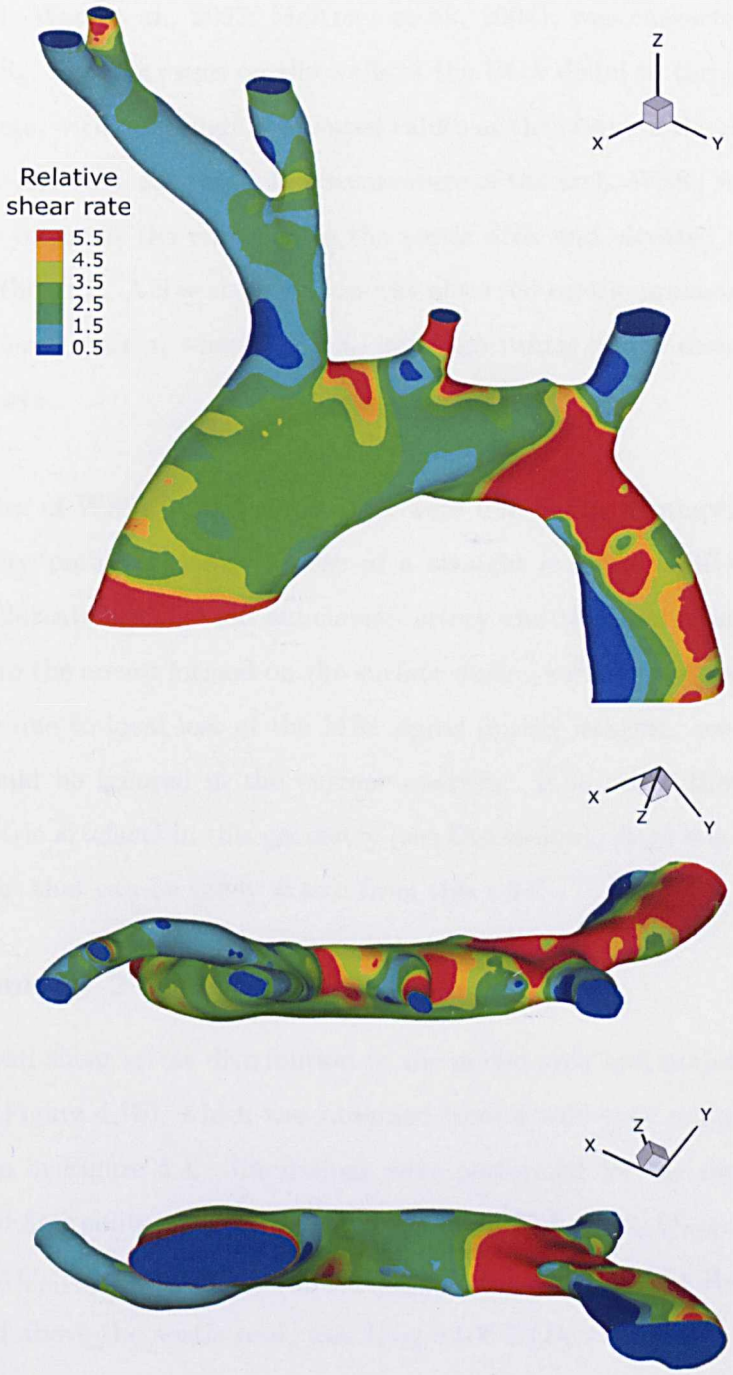

Figure 4.3: Magnitude of non-dimensionalised wall shear stress in the aortic arch and major branches of the ex vivo-scanned mouse geometry of Figure 4.1a (Geometry 1). The side, top and bottom views of the geometry are shown (from top to bottom). Mean aortic flow is from left to right. The simulations were performed for Re_{D_0}=181.9 (Q_{in}=26ml/min, D_0 ≈0.8mm) and Q_b:Q_a=22.8 : 77.2 (Q_{RSCA} =6.9%Q_{in} with equal splits into the two daughter branches, Q_{RCCA} =4.5%Q_{in}, Q_{LCCA}= 6.9% Q_{in} and Q_{LSCA} =4.5%Q_{in}).

Jackson, 2001; Won et al., 2007; McAteer et al., 2004), was characterised by low values of WSS_n. Shear stresses on the walls of the BCA distal to the junction were low to moderate, with only slightly elevated values at the origin of the right common carotid artery (RCCA). Along the lesser curvature of the arch, WSS_n was moderate, with few low values at the entrance to the aortic arch and elevated values at the distal end of the arch. A low shear region was observed on the proximal wall of the descending thoracic aorta, whereas WSS_n had high values on the distal wall of the descending aorta.

Elevated values of WSS_n at the aortic inlet were due to the assumption of a plug (blunt) velocity profile without the use of a straight extension. Elevated values around the bifurcation of the left subclavian artery and the descending aorta were possibly due to the crease formed on the surface during surface reconstruction (this is an artefact due to local loss of the MRI signal during imaging, see Discussion), and thus should be ignored in the current analysis. It is noted that due to the known geometric artefacts in this geometry (see Discussion), there is a limitation in the conclusions that can be safely drawn from this case.

4.3.2 Geometry 2

Normalised wall shear stress distribution in the aortic arch and major branches of Geometry 2 (Figure 4.1b), which was obtained from a wild-type mouse scanned in vivo, is shown in Figure 4.4. Simulations were performed for the same inlet flow rate (Q_{in}) and flow splits as for Geometry 1 (Q_b:Q_a=22.8 : 77.2, Q_{RSCA} =6.9%Q_{in}, Q_{RCCA} =4.5%Q_{in}; Q_{LCCA} =6.9%Q_{in} and Q_{LSCA} =4.5%Q_{in}). The Reynolds number, measured above the aortic root, was Re_{D_0}=106.7 (D_0 ≈1.3mm).

WSS_n was heterogeneous throughout the geometry, as in Geometry 1. Variations along the greater curvature of the aortic arch involved the occurrence of high shear stress values on the flow dividers (the highest being on the flow divider to the left common carotid artery—LCCA) and low on the proximal walls of the branches (except for LCCA where WSS_n was modestly low). A low shear region was observed at the proximal wall of the entrance to the brachiocephalic artery, similar to Geometry 1; however, in Geometry 2 this region was slightly more extended distally

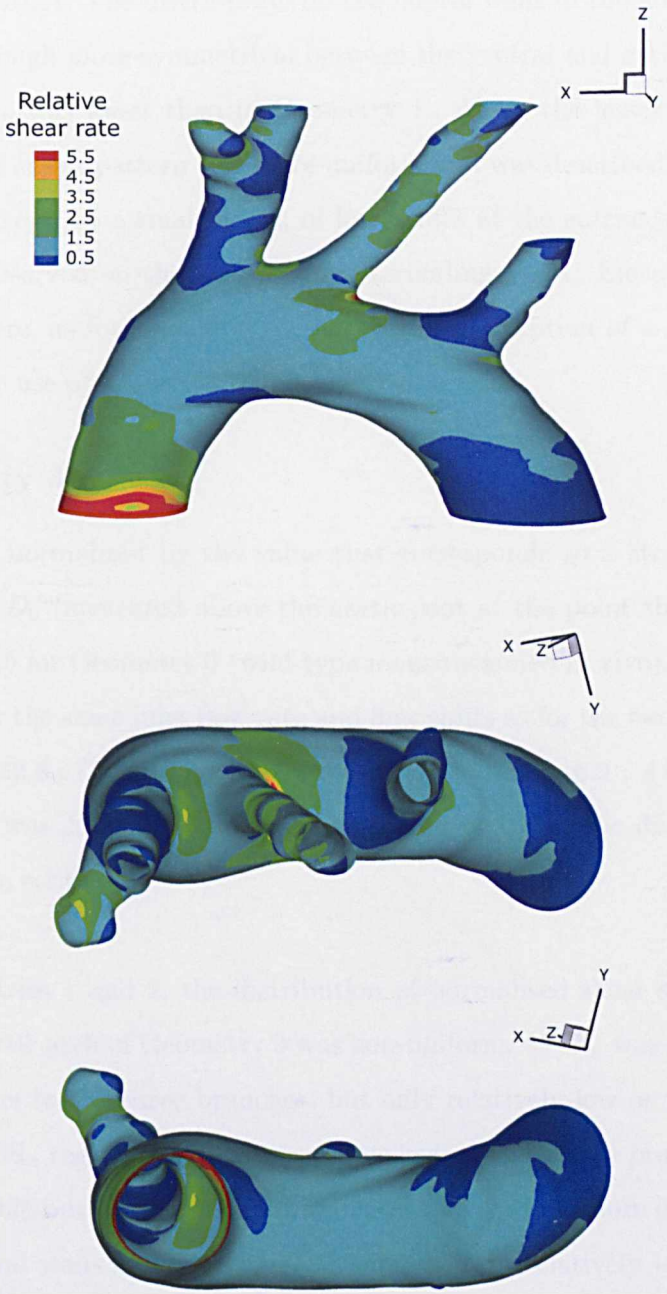

Figure 4.4: Magnitude of non-dimensionalised wall shear stress in the aortic arch and major branches of the in vivo-scanned mouse geometry of Figure 4.1b (Geometry 2). The side, top and bottom views of the geometry are shown (from top to bottom). Mean aortic flow is from left to right. The simulations were performed for Re_{D_0}=106.7 (Q_{in}=26ml/min, D_0 ≈1.3mm) and Q_b:Q_a=22.8 : 77.2 (Q_{RSCA} =6.9%Q_{in}, Q_{RCCA} = 4.5% Q_{in}, Q_{LCCA} =6.9%Q_{in} and Q_{LSCA} =4.5%Q_{in}).

to the junction of BCA. The distribution on the lateral walls of the aortic arch was again patchy, although more symmetrical between the ventral and dorsal walls (not shown), and WSS_n was lower than in Geometry 1. Along the lesser curvature of the arch, the shear stress pattern was more uniform and was described by relatively reduced values, except for a small region of low values at the entrance to the arch. Low WSS_n was observed on the walls of the descending aorta. Elevated values at the aortic inlet were, as for Geometry 1, due to the assumption of a plug velocity profile without the use of a straight extension.

4.3.3 Geometry 3

Wall shear stress, normalised by the value that corresponds to a straight tube of diameter equal to D_0 (measured above the aortic root at the point shown), is presented in Figure 4.5 for Geometry 3 (wild-type mouse scanned in vivo). Simulations were performed for the same inlet flow rate and flow splits as for the two previous geometries (Q_b:Q_a=22.8 : 77.2, $Q_{BCA} : Q_{LCCA} : Q_{LSCA} = 11.4 : 6.9 : 4.5\%Q_{in}$). The Reynolds number was Re_{D_0}=86.3, defined according to the aortic diameter above the aortic root ($D_0 \approx$1.6mm).

Similar to Geometries 1 and 2, the distribution of normalised shear stresses along the walls of the aortic arch of Geometry 3 was non-uniform. WSS_n was again highest on the flow dividers to the three branches, but only relatively low on the proximal walls. The low WSS_n region seen in the previous geometries at the proximal wall of BCA was still visible but greatly reduced in extent and located more on the ventral wall. On the lateral walls of the arch, WSS_n varied from relatively low values (at proximal locations) to moderate values (further distally) and was slightly asymmetrical between the ventral and dorsal walls (not shown). WSS_n had moderate values along the lesser curvature, except for two confined regions of relatively low values at proximal and middle locations. Aortic WSS_n downstream of the left common carotid bifurcation was elevated. A streak of low shear stresses was observed on the proximal wall of the descending aorta, whereas the distal wall was characterised by moderate WSS_n values. Finally, a significantly low shear region was observed at the entrance to the aortic arch along the greater curvature. This feature did not appear to such an extent in the previous two geometries, and may be due to the local

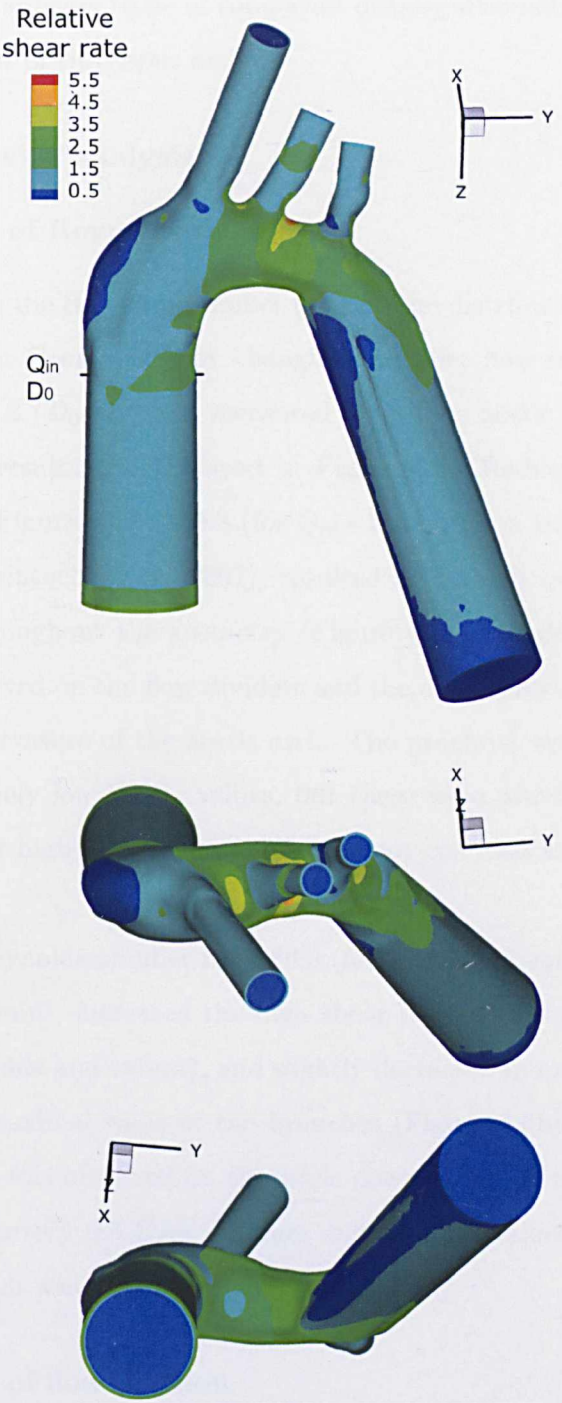

Figure 4.5: Magnitude of non-dimensionalised wall shear stress (WSS_n) for the in vivo-scanned mouse geometry of Figure 4.1c (Geometry 3). The side, top and bottom views of the geometry are shown (from top to bottom). Mean aortic flow is from left to right. The simulations were performed for Re_{D_0}=86.3 (Q_{in}=26ml/min; D_0 ≈1.6mm was measured above the aortic root, at the point shown in the figure). Q_b:Q_a=22.8 : 77.2 ($Q_{BCA} : Q_{LCCA} : Q_{LSCA} = 11.4 : 6.9 : 4.5\%Q_{in}$).

geometry, which appears to be of somewhat disproportionally larger cross-sectional area than the rest of the aortic arch.

4.3.4 Sensitivity analysis

4.3.4.1 Effect of Reynolds number

Effects of varying the Reynolds number (Re) on the distribution of normalised WSS were examined in Geometry 3 by changing the inlet flow rate (Q_{in}) for constant Q_b:Q_a=22.8 : 77.2 (D_0≈1.6mm, measured above the aortic root as shown in Figure 4.1c). The results are displayed in Figure 4.6. Reducing Re from 86.3 (for Q_{in}=26ml/min, Figure 4.5) to 39.8 (for Q_{in}=12ml/min, a value reported for anaesthetised mice; Feintuch et al., 2007), resulted in a small overall reduction of the WSS_n values throughout the geometry (Figure 4.6a). Moderately elevated WSS_n values were observed on the flow dividers and the distal portions of the lateral walls and the lesser curvature of the aortic arch. The proximal wall of BCA was characterised by relatively low WSS_n values, but these were distributed more uniformly for lower than for higher Re values, and were not confined in a specific location.

Increasing the Reynolds number from 86.3 (for Q_{in}=26ml/min, Figure 4.5) to 130.3 (for Q_{in} ≈39ml/min), increased the high shear regions downstream of the flow dividers (in magnitude and extent), and slightly decreased in magnitude the low shear regions on the proximal walls of the branches (Figure 4.6b). An extended region of highest WSS_n was observed on the walls downstream of the junction to the left common carotid artery (LCCA). A larger region of low values was seen at the outer wall of BCA which was slightly extended proximally.

4.3.4.2 Effect of flow division

Changing the ratio between the *combined* flow rate of the three branches and the flow rate in the descending aorta from Q_b:Q_a=22.8 : 77.2 (Figure 4.5) to 30:70 (Feintuch et al., 2007), while holding Q_{in} equal to 26ml/min (Re_{D_0}=86.3), had negligible effects on the WSS_n distribution (Figure 4.7a). The most notable differences were observed at the origins of the three branches where WSS_n was slightly increased in magnitude around the flow dividers, and the two low shear regions previously seen

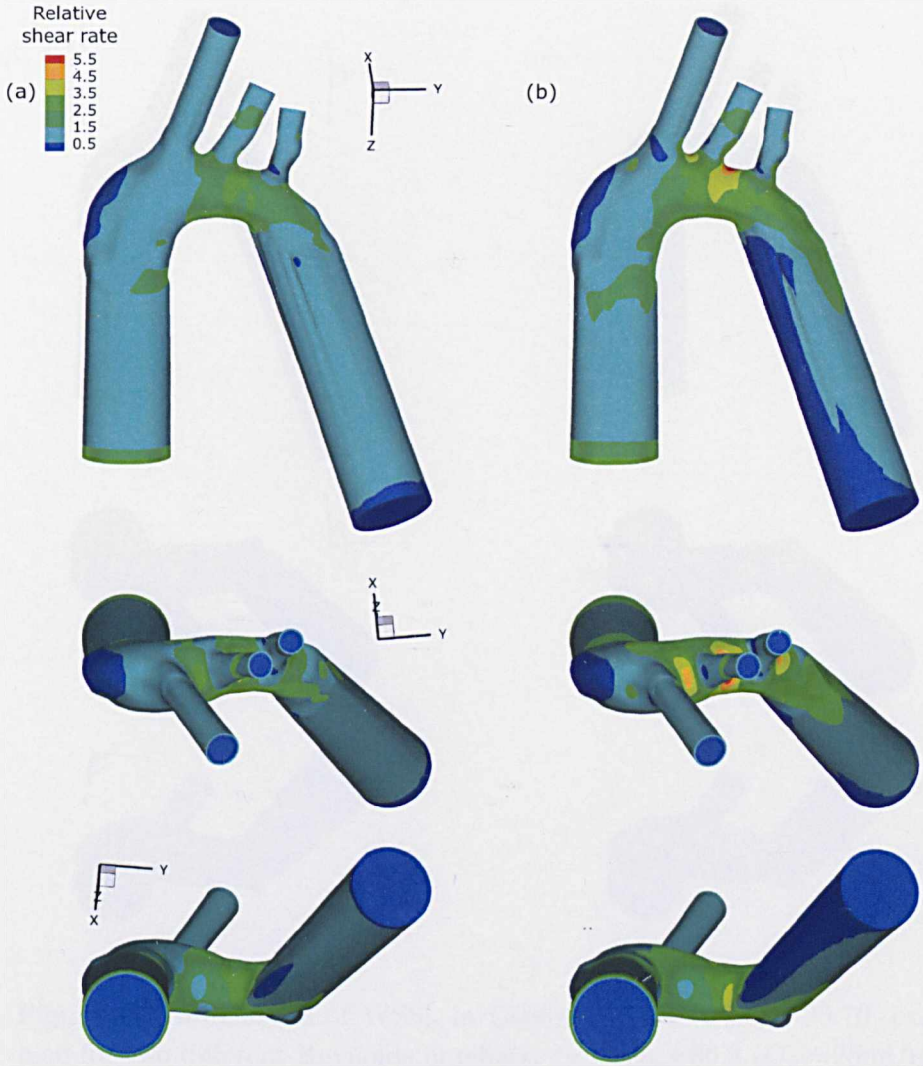

Figure 4.6: Magnitude of WSS_n in Geometry 3 for varying Re_{D_0}. (a) Re_{D_0}=39.8 (Q_{in}=12ml/min) and (b) Re_{D_0}=130.3 (Q_{in}≈39ml/min). D_0 ≈1.6mm, measured above the aortic root. Q_b:Q_a=22.8 : 77.2 (Q_{BCA} : Q_{LCCA} : Q_{LSCA} = 11.4 : 6.9 : 4.5%Q_{in}). The side, top and bottom views are shown (from top to bottom). Mean aortic flow is from left to right.

proximally to BCA and LSCA vanished. Elevated WSS_n values downstream of the LCCA junction were slightly reduced in extent. The individual flow rates for each branch were: Q_{BCA} =15%Q_{in}, Q_{LCCA} =8%Q_{in} and Q_{LSCA} =7%Q_{in}.

The WSS_n distribution for a lower Re, equal to 39.8 (Q_{in}=12ml/min), while holding the ratio Q_b:Q_a at 30:70, is shown in Figure 4.7b. As also shown in Figure 4.6a, de-

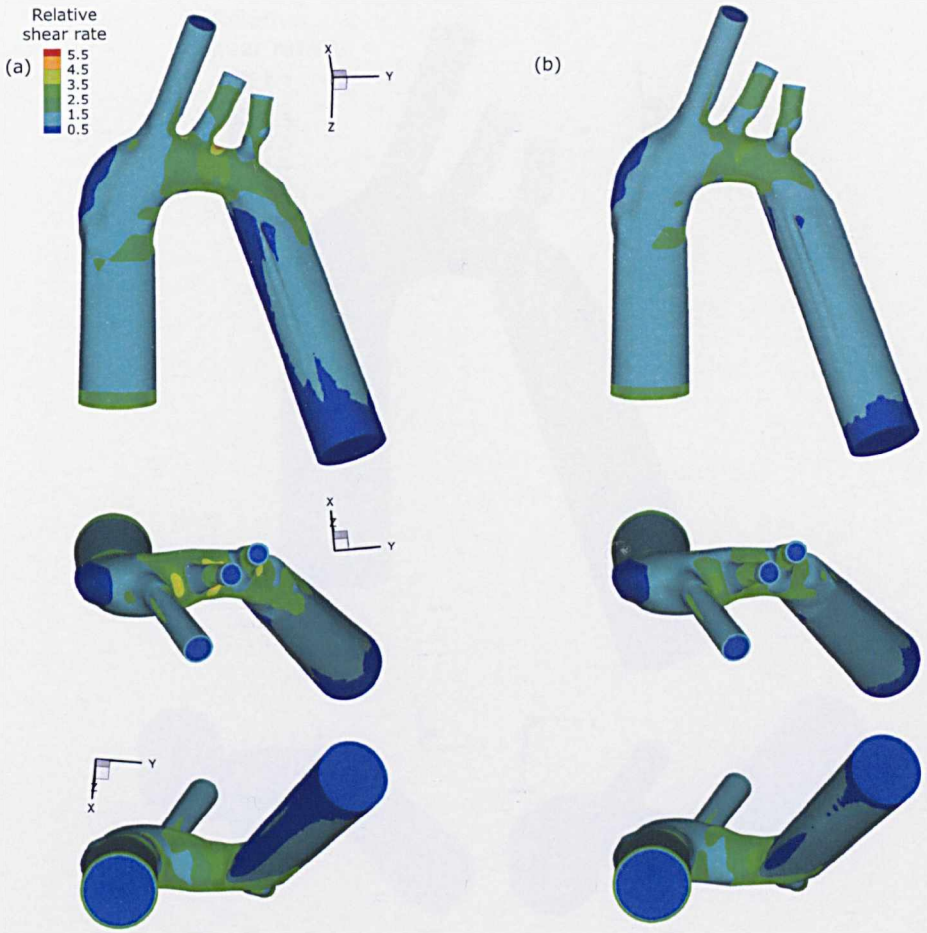

Figure 4.7: Magnitude of WSS_n in Geometry 3 for Q_b:Q_a=30:70, examined for two different Reynolds numbers: (a) Re_{D_0}=86.3 (Q_{in}=26ml/min) and (b) Re_{D_0}=39.8 (Q_{in}=12ml/min). In both cases, the individual branch flow splits were assumed as: Q_{BCA} =15%Q_{in}, Q_{LCCA} =8%Q_{in} and Q_{LSCA} =7%Q_{in} (Feintuch et al., 2007). The top and bottom views are shown below the side view for each case. Mean aortic flow is from left to right.

crease of the Reynolds number reduced the overall WSS_n throughout the geometry. With respect to the original distribution of Figure 4.5, simultaneous reduction of Re and increase of Q_b resulted in a distribution of WSS_n which was less heterogeneous. The low shear region on the proximal wall of BCA vanished and shear stresses had relatively low to moderate values. The high shear regions on the flow dividers were also greatly reduced in magnitude.

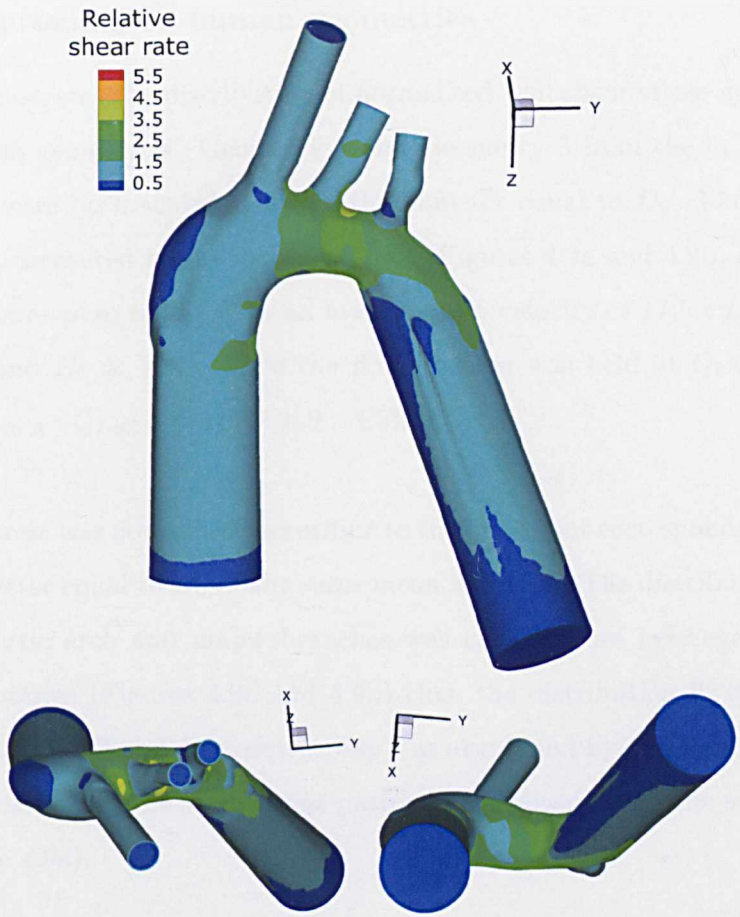

Figure 4.8: Magnitude of WSS_n in the mouse geometry of Figure 4.1c for a parabolic inlet velocity profile. Re_{D_0}=86.3 (Q_{in}=26ml/min), Q_b:Q_a = 22.8:77.2 ($Q_{BCA} : Q_{LCCA} : Q_{LSCA} = 11.4 : 6.9 : 4.5\%Q_{in}$). The top and bottom views are shown below the side view. Mean aortic flow is from left to right.

4.3.4.3 Effect of inlet velocity profile

Finally, using a fully developed (parabolic) velocity profile at the inflow boundary of Geometry 3, for the same average inflow velocity and Reynolds number as for the case of Figure 4.5, did not alter significantly the distribution of heamodynamic wall shear stress in the aortic arch (Figure 4.8). Lower WSS_n values were seen at the inflow region of the aortic extension, which was due to the use of a parabolic velocity profile. Regions of highest values of normalised WSS throughout the geometry were slightly reduced in size.

4.3.5 Approximated human geometries

Figure 4.9 illustrates the distribution of normalised wall shear stress in two approximated human geometries. Geometry 2 and Geometry 3 from the in vivo-scanned mouse data were both scaled to an aortic diameter equal to D_0=30mm (Feintuch et al., 2007), measured above the aortic root (Figures 4.9a and 4.9b, respectively). Both geometries were tested with an average inlet velocity of 17.5 cm/s (Q_{in} ≈7.4 litres/min) and $Re \approx 1352$, while the flow division was held at Q_b:Q_a=22.8:77.2 ($Q_{BCA} : Q_{LCCA} : Q_{LSCA} = 11.4 : 6.9 : 4.5\%Q_{in}$).

Wall shear stress was normalised according to the value that corresponds to a straight tube of diameter equal to D_0 at the same mean flow rate. The distribution of WSS_n along the aortic arch and major branches was clearly more heterogeneous in the human geometries (Figures 4.9a and 4.9b) than the distribution in the mouse geometries (Figures 4.4 and 4.5, respectively), as also found by Feintuch et al. (2007). Greatest variations in the shear stress pattern were observed for the scaled Geometry 2 (Figure 4.9a).

The overall low to moderate values of WSS_n, which characterised the mouse geometry of Figure 4.4, were replaced by moderate to high values in the approximated human geometry of Figure 4.9a. Regions of high WSS_n on the flow dividers to the three major branches were significantly intensified and enlarged. The low shear region at the entrance to the brachiocephalic artery remained low but was slightly shifted ventrally. The WSS_n was low on the proximal wall of LCCA (whereas WSS_n values at the equivalent location of the mouse geometry were only modestly low). The extended low shear region seen on the proximal wall of the left subclavian artery (in the mouse geometry) was split into two lateral low shear regions in the human geometry and was replaced by moderate shear values. The distribution on the lateral walls and the lesser curvature of the human aortic arch was highly patchy and more asymmetric, as compared with the relative uniformity of the distribution in the mouse aortic arch of Figure 4.4. WSS_n values were elevated on the lateral walls at the region around the junction to the left common carotid artery, and were reduced at the proximal and distal ends of the lesser curvature of the arch. Moderate shear

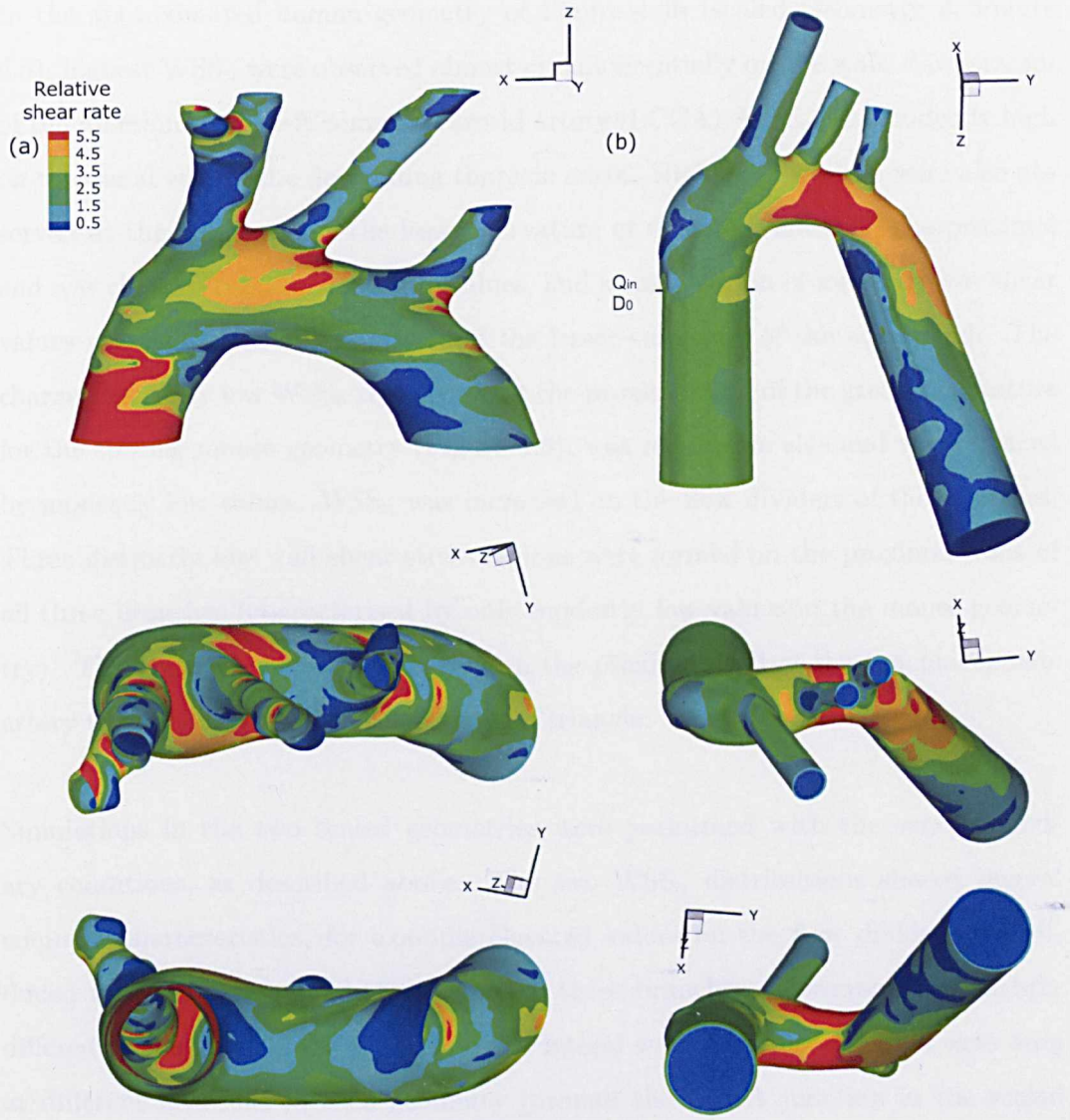

Figure 4.9: Magnitude of normalised WSS in two approximated human geometries with D_0=30mm: (a) scaled Geometry 2, (b) scaled Geometry 3. The simulations were performed for $Re_{D_0} \approx 1352$ (Q_{in} ≈7.4 litres/min, U= 17.5 cm/s; Feintuch et al., 2007), and Q_b:Q_a=22.8:77.2 ($Q_{BCA} : Q_{LCCA} : Q_{LSCA} = 11.4 : 6.9 : 4.5\%Q_{in}$). The side, top and bottom views are shown (from top to bottom). Mean aortic flow is from left to right.

values were seen on the distal walls of the descending aorta, whereas the region of elevated WSS_n values on the aortic inlet, due to the assumption of a plug velocity profile without the use of a straight extension, was significantly enlarged.

In the approximated human geometry of Figure 4.9b (scaled Geometry 3, Figure 4.5), highest WSS_n were observed almost circumferentially on the walls downstream of the junction to the left common carotid artery (LCCA). WSS_n was modestly high on the distal wall of the descending thoracic aorta. High WSS_n values were also observed at the distal end of the lesser curvature of the arch, however, the proximal end was characterised by moderate values, and a small region of modestly low shear values was developed at the middle of the lesser curvature of the aortic arch. The characteristically low WSS_n region seen at the proximal wall of the greater curvature for the specific mouse geometry (Figure 4.5), was reduced in size and was replaced by modestly low values. WSS_n was increased on the flow dividers of the branches. Three distinctly low wall shear stress regions were formed on the proximal walls of all three branches (characterised by only modestly low values in the mouse geometry). The low wall shear stress region on the proximal wall of the brachiocephalic artery took on the shape of a downstream triangle.

Simulations in the two scaled geometries were performed with the same boundary conditions, as described above. The two WSS_n distributions shared several common characteristics, for example elevated values on the flow dividers and reduced values on the proximal walls of the three branches. However, they slightly differed in that high shear regions on the lateral walls of the aortic arch were seen at different locations in each geometry (around the LCCA junction in the scaled Geometry 2, and upstream of the LSCA junction in the scaled Geometry 3). In addition, they differed in that the lesser curvature was characterised (following a proximal-to-middle-to-distal direction on the lesser curvature of the arch) by low-to-moderate-to-low values in the scaled Geometry 2, and by moderate-to-relatively low-to-high values in the scaled Geometry 3.

4.4 Discussion

We used computational tools to reconstruct and model the aortic arch and proximal major branches of three wild-type mice (free of disease), scanned ex vivo or in vivo with MRI. Furthermore, two of these geometries were scaled to an aortic diameter of 30mm, which is typical of men, to approximate the human aortic arch. The distribu-

tion of normalised wall shear stress within the arch of each geometry was computed assuming steady flow conditions, a uniform inlet velocity profile and branch flow splits within the physiological range of conscious or anaesthetised mice and healthy men (Shahcheraghi et al., 2002; Suo et al., 2007; Feintuch et al., 2007). Our main finding was that the distribution of wall shear stress varies significantly between the two species. Wall shear stresses had a more heterogeneous distribution in the human aortic arch than in the mouse arch, with elevated or reduced WSS values being intensified and enlarged in size in the human case. Other features, however, were similar in both species and the proximal wall of the brachiocephalic artery, a location susceptible to the development of atherosclerotic lesions, was characterised in most cases by low values of shear stress. Similar observations were published by Feintuch et al. (2007) whilst this work was being carried out.

Comparison of the magnitude of the normalising shear stress between the two species gives information about scaling effects. For the mouse of Geometry 2, the normalising shear stress—which corresponds to a straight tube of diameter equal to D_0 at the same mean flow rate—was approximately 74.77 dynes/cm^2, whereas for the equivalent approximated human geometry the normalising WSS was approximately 1.87 dynes/cm^2. In Geometry 3, this value was approximately 39.58 dynes/cm^2 for the mouse and 1.87 dynes/cm^2 for the equivalent approximated human geometry. This suggests that the non-normalised WSS was approximately 40 times higher in the mouse than in the human case for Geometry 2, and 21 times for Geometry 3. The latter result is in good agreement with existing scaling laws which give a theoretical prediction of an approximately 20-fold difference in the WSS between the two species (Weinberg and Ethier, 2007) and experimental data (Greve et al., 2006) which give the same result. This is further supported by the results of Feintuch et al. (2007) who have reported a normalising shear stress, estimated according to the same formula, of 58 dynes/cm^2 for a mouse and 1.63 dynes/cm^2 for an approximated human geometry, leading to an approximately 35-fold difference of WSS. It is noted that the normalising WSS value depends only on the Reynolds number and the diameter of the vessel lumen, which in turn depends on the location of measurement and may vary between different geometries.

Mouse-to-mouse anatomical variability showed that the WSS distribution is greatly influenced by the detailed anatomical geometry of the aortic arch and major branches. Nevertheless, some features of the distribution were common in all geometries, primarily the occurrence of elevated WSS_n values on the flow dividers to the three branches and reduced values on the proximal walls of the branches. Flow divisions in the three major branches may vary with physiological demand, however, we showed that their influence on WSS is relatively small within the mouse physiological range. Varying the Reynolds number had a significant influence on the distribution of stresses on the walls of the arch. Increasing Re produced greater variations in the pattern of wall shear stresses. These influences were tested only for one of the mouse geometries (Geometry 3) but are expected to hold true also for the other two geometries. Between the two approximated human cases, for which common inflow and boundary conditions were used (and the same aortic diameter), the distribution of WSS_n slightly differed, again implying the importance of the local three-dimensional anatomy.

The anatomy was similar in all cases examined, with three major branches emanating from the greater curvature of the aortic arch; however, the detailed anatomical characteristics, such as the angle of branching of the major arteries, or the curvature and/or twisting of the aortic arch, varied among the three subjects. Small differences in the geometries may also be attributable to artefacts arising during the imaging, segmentation or reconstruction processes. Geometry 1, in particular, differed from the other two geometries in that it was obtained from a mouse scanned ex vivo by MRI. For that, the mouse was placed within an MR tube which unavoidably imposed some degree of twisting on the aortic root and the ascending aorta, despite the fact that the mouse was perfusion-fixed in situ and the arteries were still attached to the spine during the placement in the MR tube. For this reason, the aortic root and proximal ascending aorta was excluded from the geometry and was slightly corrected during the surface reconstruction process. In addition, loss of the MRI signal during image acquisition resulted in an artefact around the bifurcation of the left subclavian artery and the descending thoracic aorta. The region was corrected manually during reconstruction, which resulted in a crease on the surface. The other two geometries did not contain any major artefacts. However, semi-automated segmentation in all

three geometries is inherently subjected to some degree of subjectivity and hence uncertainty.

A better understanding of the observed wall shear stress distributions can be gained by studying the flow field within the aortic arch and the three proximal branches. Through-plane velocities (contours) and in-plane streamlines were calculated on seven cross sections along the aortic arch and the major branches of Geometry 2, for the mouse and human cases (shown in Figures 4.10 and 4.11, respectively). The velocities were normalised according to the average inlet velocity. The cross sections were perpendicular to the medial lines of the aortic arch and each of the branches, obtained using an in-house skeletonisation (thinning) algorithm (Giordana et al., 2005b). The cross sections were considered at the same locations for both cases and are illustrated with successive numbers on the wall shear stress maps at the bottom of each figure. Aortic arch cross-sectional slices (top row of each figure) are oriented so that the top and bottom points correspond to points on the greater and lesser curvature of the arch, respectively. In addition, the left and right points of each cross section correspond, respectively, to points on the ventral and dorsal walls of the arch; i.e. the observer faces upstream, or—in other words—in a distal to proximal view, and the mean aortic flow is toward the observer. Cross sectional slices displayed at the middle row of each figure are oriented so that the top and bottom points correspond, respectively, to the proximal and distal walls of each arterial branch. The left and right points correspond again to points on the ventral and dorsal side of the geometry, respectively. The mean aortic flow is toward the observer, in a cranial to caudal view. The relative dimensions of the cross sections were maintained to show vessel diameter variation along the arch and arterial vessels.

At a location upstream of the junction to the brachiocephalic artery (slice 1 in the mouse geometry of Figure 4.10), axial flow was only slightly skewed in the cranioventral direction. The displacement generated secondary motion in the transverse plane in the form of a pair of counter-rotating vortices, similar to the *Dean* vortices for planar curved pipes. However, these vortices were asymmetrical; the right-handed clockwise vortex was larger in strength and size than the left-handed vortex. Downstream of the flow divider to BCA (slice 2), peak velocities were highly skewed toward

the greater curvature of the arch, taking on the shape of an asymmetric crescent. The pair of counter-rotating vortices was slightly more symmetrical than on the previous slice, and the centres of rotation for each vortex were rotated and shifted. Downstream of the flow divider to the left common carotid artery (LCCA, slice 3), the primary vortex pair was annihilated, while the peak flow was partly restored toward the axial centreline. At the entrance to the descending thoracic aorta (slice 4), that is, downstream of the flow divider of the left subclavian artery (LSCA), the bulk flow was only slightly skewed toward the top part of the cross-section. Two new counter-rotating vortices were generated, which were relatively symmetrical and whose centres of rotation were near the lateral walls of the aortic arch. Flow within the first major branch of the aortic arch (BCA, slice 5) was skewed toward the distal wall. Slices 6 and 7 show contours of axial velocity in the LCC and LSC arteries, respectively. In the former branch, the flow was relatively symmetrical, whereas in the latter branch the bulk flow was skewed toward the distal wall. No vortical structures were apparent in the flow within the three branches of the mouse geometry.

Figure 4.11 shows cross sections along the aortic arch and major branches in one of the approximated human geometries (scaled Geometry 2; see figure caption for boundary conditions used). Although the simulation was performed using a uniform velocity profile on the aortic inlet, by slice 1 of the geometry, which was located upstream of the junction to the BCA, the bulk of the aortic flow was already highly skewed in the cranioventral direction, and low velocities appeared near the lesser curvature of the aortic arch. A highly asymmetric pair of counter-rotating vortices was generated, with the right-handed vortex being much larger than the left-handed vortex. Distal to the BCA (slice 2), peak velocities were concentrated near the greater curvature of the arch, whereas at the opposite wall, near the lesser curvature of the arch, through-plane velocities were restricted to low values. The right-handed primary vortex dominated in the transverse plane, annihilating the left-handed vortex. A secondary vortex was generated at locations of slower-moving flow near the bottom of the section. By slice 3, which is located distal to the LCCA, the right-handed primary vortex was cancelled, although the smaller secondary vortex near the bottom persisted. The bulk of the flow occupied the top half of the cross section, closer to the greater curvature of the arch. Distal to the LSCA (slice 4), the flow was

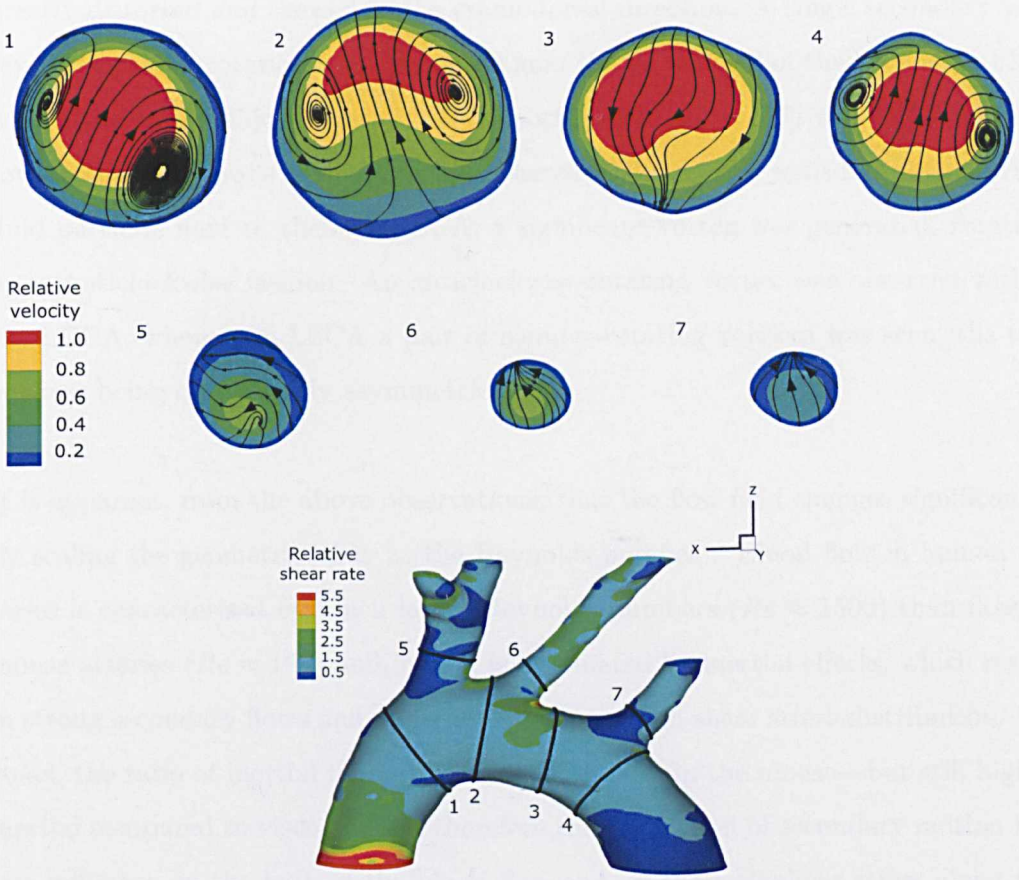

Figure 4.10: Non-dimensionalised through-plane velocities (contours) and in-plane streamlines at seven cross sections along the aortic arch and three major branches of the mouse Geometry 2 (top and middle rows). Each cross section is numbered and its location is illustrated on the non-dimensionalised wall shear stress map for this case (bottom row, Figure 4.4). The relative dimensions of the cross sections were preserved to show vessel diameter variation along the different arterial locations. Aortic arch cross sections (in the top row) are oriented so that the top and bottom points correspond to points on the greater and lesser curvature of the arch, respectively. Cross sections at the middle row are oriented so that the top and bottom points correspond to the proximal and distal walls of each arterial branch, respectively. Mean aortic flow is toward the observer (distal to proximal view for the top row, and cranial to caudal view for the middle row). The simulations were performed for Re_{D_0}=106.7 (Q_{in}=26ml/min, D_0 ≈1.3mm) and Q_b:Q_a=22.8 : 77.2 (Q_{RSCA} =6.9%Q_{in}, Q_{RCCA} =4.5%Q_{in}, Q_{LCCA} = 6.9% Q_{in} and Q_{LSCA} =4.5%Q_{in}).

greatly distorted and skewed in the craniodorsal direction. A single secondary vortex, of clockwise rotation, was generated near the dorsal wall of the geometry. Flow within the three major branches of the aortic arch (slices 5-7) was highly skewed toward the distal walls of the branches, whereas the proximal walls had slow-moving fluid particles next to them. In BCA, a significant vortex was generated, rotating in an anticlockwise fashion. An anticlockwise-rotating vortex was observed within the LCCA, whereas in LSCA a pair of counter-rotating vortices was seen, the two vortices being only slightly asymmetrical.

It is apparent, from the above observations, that the flow field changes significantly by scaling the geometry (that is, the Reynolds number). Blood flow in human arteries is characterised by much larger Reynolds numbers ($Re \approx 1500$) than flow in mouse arteries ($Re \approx 100$) and, hence, is dominated by inertial effects, which result in strong secondary flows and more heterogeneous wall shear stress distribution. Instead, the ratio of inertial to viscous forces is smaller in the mouse—but still highly inertial compared to viscous—and therefore the generation of secondary motion has less influence on the bulk of the blood flow and on the wall shear stress along the aortic arch.

In the mouse geometry of Figure 4.10, aortic flow was characterised by low inertia and could be easily displaced to follow the curvature of the aortic arch; hence, it preserved much of its axial direction, which also explains the moderate wall shear stress values seen in that region. Nevertheless, a small displacement of the faster moving fluid particles, toward the proximal wall of the aortic arch, was imposed due to the curvature and torsion of the arch. This is apparent from the generation of asymmetrical vortical structures in slice 1 of Figure 4.10. In the vicinity of the flow divider of the brachiocephalic artery, the faster moving flow, which was already displaced closer to the outer wall of the arch and accelerated in order to preserve the axial flow, split and entered the BCA. Pressure gradients, developed downstream of the junction to BCA, could not displace immediately the flow into the downstream axial directions and, hence, the flow was skewed toward the inner walls of the bifurcation (distal wall of BCA and greater curvature of the arch). This explains the occurrence of high shear stresses on the flow dividers to all three major

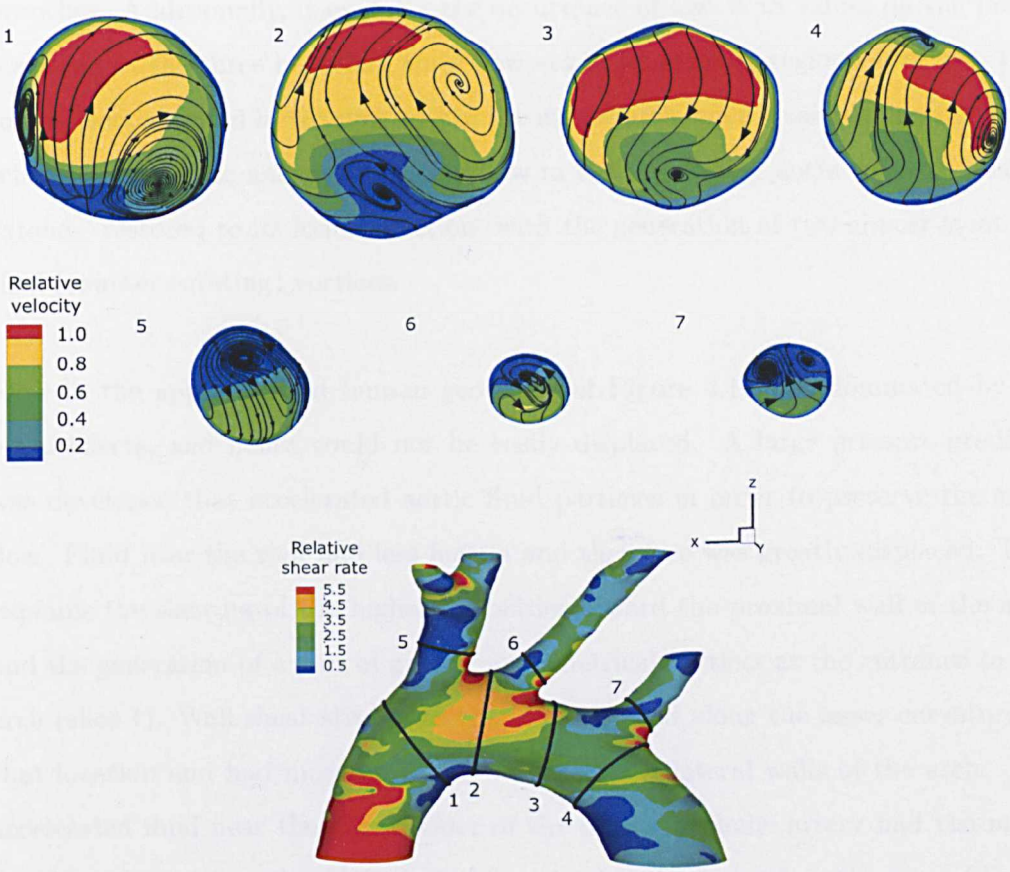

Figure 4.11: Non-dimensionalised through-plane velocities (contours) and in-plane streamlines at seven cross sections along the aortic arch and three major branches of the approximated human geometry (scaled Geometry 2, top and middle rows). Each cross section is numbered and its location is illustrated on the non-dimensionalised wall shear stress map for this case (bottom row, Figure 4.9a). The relative dimensions of the cross sections were preserved to show vessel diameter variation along the different arterial locations. Aortic arch cross sections (in the top row) are oriented so that the top and bottom points correspond to points on the greater and lesser curvature of the arch, respectively. Cross sections at the middle row are oriented so that the top and bottom points correspond to the proximal and distal walls of each arterial branch, respectively. Mean aortic flow is toward the observer (distal to proximal view for the top row, and superior to inferior view for the middle row). The simulations were performed for $Re_{D_0} \approx 1352$ (Q_{in}≈7.4 litres/min, U= 17.5 cm/s, D_0 =30mm) and Q_b:Q_a=22.8 : 77.2 (Q_{RSCA} =6.9%Q_{in}, Q_{RCCA} =4.5%Q_{in}, Q_{LCCA} =6.9%Q_{in} and Q_{LSCA} =4.5%Q_{in}).

branches. Additionally, it explains the occurrence of low WSS values on the proximal walls of the three branches, since flow velocities in those regions were low. Due to low inertial forces in the flow within the mouse arch, wall shear stresses remained relatively moderate and uniform, and flow in the descending aorta was—to a large extend—restored to its axial direction, with the generation of two almost symmetrical (counter-rotating) vortices.

Flow in the approximated human geometry of Figure 4.11 was dominated by inertial effects, and hence could not be easily displaced. A large pressure gradient was developed that accelerated aortic fluid particles in order to preserve the axial flow. Fluid near the wall had less inertia and therefore was greatly displaced. This explains the skewing of the highest velocities toward the proximal wall of the arch and the generation of a pair of greatly asymmetrical vortices at the entrance to the arch (slice 1). Wall shear stress was therefore reduced along the lesser curvature at that location and had more moderate values on the lateral walls of the arch. The accelerated fluid near the flow divider of the brachiocephalic artery had too much inertia and consequently the highest velocities remained closer to the inner (distal) walls of the bifurcation. As a result, high wall shear stresses were developed on the walls downstream of the junction. Blood flow velocities on the walls opposite to the junction, that is, the proximal wall of the BCA and the lesser curvature of the aortic arch, were low. However, lower velocities occurred slightly above the wall of the lesser curvature of the aortic arch resulting in relatively moderate (and not low) values of WSS at the middle of the lesser curvature of the arch. Flow within the descending aorta was highly skewed, rotated, and distorted due to its high inertia and the effect of the non-planar curvature and torsion of the arch.

Flow in the other geometries considered in this study was not analysed in detail; however, it is expected that it follows similar development to that presented for Geometry 2, for mouse and human haemodynamic conditions. The curvature, non-planarity, cross-sectional area variation and torsion of the aortic arch have certainly an important influence on the flow and wall shear stress distribution in the aortic arch. For example, the wider cross-sectional area of the entrance to the aortic arch in Geometry 3 may explain why wall shear stresses upstream of the junction to

BCA were more moderate in Geometry 3 than in Geometry 2. Similarly, the cross-sectional area downstream of the junction to LCCA in Geometry 3 was smaller, resulting in acceleration of the bulk flow and thus higher wall shear stresses almost circumferentially on the aortic wall. Geometry 2 had a more uniform cross-sectional area along sections of the aortic arch than Geometry 3; the largest cross-sectional area being downstream of the flow divider to BCA (as seen from the relative size of the slices in Figures 4.10 or 4.11).

Several simplifications were made in the above analysis, most importantly that of steady flow. Blood flow in people is certainly highly pulsatile and enforces the development of large blood flow velocities and secondary flows within the aortic arch during left ventricular contraction. Our results indicated rotation of the bulk flow through the approximated human aortic arch, which may be intensified and result in a swirl or helical-type flow under unsteady conditions. More important are, however, the local flow features, such as the development of new boundary layers, variations in the local Reynolds and Womersley numbers, and reversal of flow, which may influence the WSS distribution. In the mouse, unsteady flow is not expected to alter significantly the results. However, local flow features and retrograde flow previously observed in the aortic arch (Feintuch et al., 2007) may influence the wall shear stress and flow patterns, particularly the distribution along the lesser curvature. Furthermore, simulations in this study were performed in geometries with rigid walls, which is another important simplification. The proximity of the ascending aorta and the aortic arch to the heart certainly imposes significant wall displacements, which in turn may alter the instantaneous distributions of wall shear stress. Time-averaged results, however, are expected to share some common characteristics with the steady flow patterns observed here, at least for the mouse geometries. Finally, another major simplification was the inlet velocity profile, which is likely to be skewed and rotating in vivo.

4.4.1 Comparison with other studies

During the course of this study, two other independent studies by Suo et al. (2007) and Feintuch et al. (2007) were published, concerning flow and wall shear stress distribution in the mouse aortic arch. Our results are in good agreement with

their findings for equivalent blood flow conditions. Feintuch et al. (2007) studied wall shear stress in a mouse geometry with an aortic root diameter of 1.3mm, very close to the diameter measured above the aortic root for the mouse of Geometry 2. Although they used slightly different inflow conditions and branch flow splits in a geometry with a relatively steeper curvature and smaller, more elliptical, cross-sectional areas, the wall shear stress distribution was characterised, as in Geometry 2, by low to moderate and relatively uniform values. However, locations of elevated or reduced WSS were more distinct in the geometry presented here (Geometry 2), and flow velocities downstream of the BCA bifurcation were more skewed toward the greater curvature of the arch. WSS patterns in the mouse Geometry 3 showed similar characteristics. WSS distribution in Geometry 1 was in greater agreement with the results presented by Suo et al. (2007), where the variations of WSS along the arch were slightly larger, although they assumed higher Reynolds numbers in their simulations.

Concerning wall shear stress and flow patterns in the human aortic arch, our results are consistent—in general—with those of Feintuch et al. (2007). They showed an increase in the heterogeneity of the WSS distribution in the human arch and the development of stronger secondary flow motion (compared with WSS in the mouse arch) for a geometry scaled to an aortic root diameter of 30mm, similar to the results for the scaled Geometry 2. However, the significantly low wall shear stress region seen in their results along the lesser curvature of the arch was not apparent in the approximated human geometry presented here (scaled Geometry 2). This may be due to the smoother curvature of the arch in Geometry 2; a steeper curvature may have resulted in a similar low WSS region along the lesser curvature of the arch. However, flow velocities at cross sections along the human arch differed from those reported in Feintuch et al. (2007) in terms of velocity skewing and vortex generation. The flow development in the human arch was similar in character to the flow field reported by Shahcheraghi et al. (2002) during the forward-flow part of a periodic flow. Finally, more fundamental studies of flow in non-planar curved pipes (Mori and Yamaguchi, 2002) have shown asymmetrical vortical structures, as also presented here.

As previously discussed, variation between subject-specific models, and the use of different haemodynamic conditions, make difficult the comparison between different studies. Variations in the curvature, non-planarity, cross-sectional area and torsion of the aortic arch appear to be important geometrical parameters that influence the distribution of WSS. In addition, it was shown that the Reynolds number affects significantly the flow and WSS. The geometries studied here were within the physiological and anatomical range of mice and men, and hence the results complement in the characterisation of their environments.

4.4.2 Physiological and pathological relevance

Low WSS values found at the outer (proximal) wall of the BCA correlate well with locations of vulnerable atherosclerotic plaques in apoE-/- mice as previously observed in histopathological sections by McAteer et al. (2004) and Schneider et al. (2004). However, a study by Iiyama et al. (1999) showed high probability of mouse lesions on the inner curve of the ascending aorta (at the entrance to the aortic arch) and low probability on the outer wall. This cannot be explained by the results presented here, or by those published by Feintuch et al. (2007), but does correlate with changes in flow direction in the study by Suo et al. (2007). They observed co-localisation of low mean WSS values and increased expression of vascular cell adhesion molecule-1 (VCAM-1) and intracellular adhesion molecule-1 (ICAM-1) along the inner curvature of the mouse ascending aorta and aortic arch. Due to the high heart rate in the mouse, endothelial cells are subjected to large and rapid variations of WSS throughout the cardiac cycle. Furthermore, mean wall shear stresses are substantially larger than in the human aorta. However, Suo et al. (2007) suggest that because focal inflammatory changes are still observed, the relative change or direction of WSS may be more important than its absolute magnitude.

In the above analysis, we studied WSS and flow patterns in geometries of wild-type mice in an attempt to correlate these with lesions observed in diseased mice. It remains open to question, however, whether normal and diseased mice have similar haemodynamic environments. Hartley et al. (2000) have reported differences in the magnitude and shape of the velocity waveform within the aortic arch of wild-type and apoE knockout mice. The apoE-/- mice have higher cardiac outputs and stroke

volumes than wild-type mice (as well as lower hematocrits and higher ratios of heart weight to body weight), despite having normal heart rates and blood pressures. Nevertheless, with reference to the analysis presented here, it is expected that the differences in aortic velocity, and hence in Reynolds number, are not sufficiently large to fundamentally alter the flow characteristics and hence the wall shear stress patterns within the aortic arch.

Chapter 5

Conclusions and further work

5.1 Conclusions

This research aimed to investigate the wall shear stress (WSS) distributions and the underlying blood flow patterns near arterial branches of the descending thoracic aorta and the aortic arch, using computational methods for fluid dynamics. The objectives were, first, to address for the first time age- and species-related changes in the wall shear stress distribution, in relation to the initiation and localisation of atherosclerosis; second, to establish the flow characteristics within the two arterial sites; and third, to find correlations with in vivo lesion maps. These three objectives have been met, to the extent possible and acknowledging limitations of the work. However, there are still several questions that remain unanswered.

In conclusion, this thesis contributes toward an understanding of the role of haemodynamics in the localisation of atherosclerosis as follows:

(i). It demonstrates the effects of the Reynolds number (Re) (reflecting effects of different species and age, and hence body size) and flow partition (which may also vary with age and species) on aortic WSS around small side branches, such as the intercostal arteries in the thoracic aorta. Increase of these two parameters increases significantly the variation of the WSS around the branch ostium. Similarly, increase of the Reynolds number in the aortic arch increases the heterogeneity of the WSS distribution. Examination of the effects of flow division in the aortic arch was limited to one different value for low Re numbers

and therefore it is more difficult to conclude whether it shows the same effect as in the work of flow around model intercostal arteries.

(ii). It shows the quasi-steady nature of the flow for moderate Re values and physiological range of unsteady conditions. Consistent with earlier work, the effect of pulsatility is small under these conditions and the time-averaged WSS results are similar in character to the equivalent steady flow patterns.

(iii). It demonstrates the importance of reversing (retrograde) flow, an effect which changes with age (Sloop et al., 1998). Within the intercostal artery or the near-wall region of the thoracic aorta, reversing flow waveforms can cause significant alterations to the distributions of aortic WSS and oscillatory shear index (OSI). Elevated OSI values (hence, temporal oscillations of the WSS vector) correlate well with regions of low WSS values for reversing aortic near-wall flow, whereas this is not true for reversing side branch flow or forward flow waveforms (antegrade flow).

(iv). The use of more realistic geometries had little influence on the results of the study of flow around intercostal arteries, demonstrating the practicability of using *reduced* model geometries for understanding complex systems. However, the use of subject-specific geometries in the study of the mouse aortic arch showed the importance of the general anatomy, such as the curvature, non-planarity, cross-sectional area, torsion of the arch and angle of branching of the proximal arteries. In addition, more detailed geometrical features, such as small bumps or dips on the aortic wall, may cause local alterations of the WSS distribution (like the enlarged outer wall of the arch in Geometry 3, Chapter 4). Nevertheless, these differences concern primarily changes within a species. The use of the same geometries (Geometries 2 and 3, Chapter 4) for studying WSS differences between mice and men, showed that the flow conditions that in general characterise each species have greater influence on WSS (larger variations in the human case) than the specific geometry.

(v). It successfully correlates WSS distributions around intercostal ostia with in vivo lesion maps of mice of all ages (almost uniform WSS pattern at low Re and Q_b:Q_a values) and of mature rabbits (low WSS and high OSI lateral regions

under reversing aortic near-wall flow at higher Re and Q_b:Q_a). In addition, it correlates the low WSS region at the proximal wall of the brachiocephalic artery of wild-type mice with lesion locations in apoE-/- mice. Other locations of lesions, however, cannot be explained with the obtained results, perhaps implying that other localising mechanisms may also be important.

5.2 Suggestions for further work

Several suggestions can be made for further work, initially in terms of varying the boundary conditions in the models examined. In the study of flow around intercostal ostia, the use of a physiological velocity waveform at the inflow boundary condition could add to the characterisation of the WSS distribution. More importantly, however, the examination of a fully reversing aortic waveform could potentially produce new WSS patterns. Although it is expected to have little influence due to the small velocities of radial wall motion as compared to the radial flow components caused by the branch, it could be useful to take into consideration effects of oscillating wall motion in the model. In the study of WSS patterns in the mouse aortic arch, more accurate physiological boundary conditions could be examined, in particular an unsteady or physiological velocity waveform at the inlet (spatially and temporally). It would be of great value to include also effects of wall motion in the model. Finally, accurate measurements of the inlet flow rate and the branch flow splits in mice and men could help standardise some of these values.

The work of this thesis could be further extended to more complex investigations. We examined the flow around one or two intercostal ostia, which helps understand and explain single mechanisms. However, this could be extended to involve anatomically correct geometries including multiple pairs of intercostal arteries, or the whole arterial section from the aortic root to the abdominal aorta. This would identify whether there is any major influence of the upstream aortic flow. Arising from the left ventricle and flowing through the aortic arch, the flow may include features (in the form of secondary motions or skewed velocities) that may remain present at the level of intercostal arteries in the thoracic aorta, and therefore may affect the distribution of WSS. In addition, examining the WSS distribution in a number of

different anatomically correct geometries, also perhaps of different age, could help identify intraspecies variations.

Similarly, the study of WSS patterns in the mouse aortic arch could be extended to study more geometries and, in particular, to include anatomically correct human geometries. In addition, it would be interesting to extend the study to geometries from diseased mice and investigate the progression of atherosclerotic lesions and how they alter the local haemodynamic environment, by examining variations of WSS at different stages of lesion progression. Finally, it would be valuable to investigate distributions of WSS around advanced plaques in conjunction with plaque characterisation by histopathology.

Idealised and simplified models help us understand the fundamental mechanisms behind distributions that otherwise would be difficult to identify. Ultimately, they should help identifying mechanical correlates of regions prone to athersoclerosis, and thus potentially help find mechanisms to prevent or reverse the disease.

Appendix A

Appendix

A.1 Womersley solution for prescribed average cross sectional flow between two parallel flat plates

The governing equations of motion for a Newtonian fluid of density ρ and dynamic viscosity μ can be described by the incompressible Navier-Stokes equations (Equations 3.1-3.2). Flow between two parallel flat plates, with velocity components $u = u(z,t)$, $v = w = 0$ (the flow assumed in the x-direction), can be expressed as:

$$\frac{\partial u}{\partial t} = -\frac{1}{\rho}\frac{\partial p}{\partial x} + \nu\frac{\partial^2 u}{\partial z^2} \tag{A.1}$$

where $\nu = \mu/\rho$ is the kinematic viscosity of the fluid and $\partial p/\partial x$ the pressure gradient.

If $u(z,t) = u'(z)e^{i\omega t}$ and $p = p(x,t) = A_p x e^{i\omega t}$, Equation A.1 can be written as:

$$\frac{d^2u'}{dz^2} - \frac{i\omega}{\nu}u' = -\frac{A_p}{\rho\nu} \quad , A_p > 0 \tag{A.2}$$

where A_p is a complex number representing a negative pressure gradient along the direction of flow.

Equation A.2 is a linear non-homogeneous second-order ordinary differential equa-

tion (ODE) which can be expressed as the sum of a particular, $u'_p(z)$, and a homogeneous, $u'_h(z)$, solutions: $u'(z) = u'_p(z) + u'_h(z)$. The homogeneous ODE has an obvious solution ($u'_h = 0$) and a general solution, expressed as:

$$u'_h = \mathcal{C}(e^{\sqrt{\frac{i\omega}{\nu}}z} + e^{-\sqrt{\frac{i\omega}{\nu}}z}) \tag{A.3}$$

where $\mathcal{C}$ is a constant. It is likely that the form of the particular solution is $u'_p = \mathcal{C}_p$, where $\mathcal{C}_p$ is a constant. By substitution is found that: $u'_p = -\frac{A_p i}{\rho\omega}$.

Hence the general solution to Equation A.2 is:

$$u'(z) = \mathcal{C}(e^{\sqrt{\frac{i\omega}{\nu}}z} + e^{-\sqrt{\frac{i\omega}{\nu}}z}) - \frac{A_p i}{\rho\omega} \tag{A.4}$$

Taking D_a to be the distance between the flat plates and by replacing $\sqrt{\frac{i\omega}{\nu}} = \frac{2\alpha}{D_a} i^{1/2}$ (where $\alpha = D_a/2\sqrt{\frac{\omega}{\nu}}$ is the Womersley number), the solution to Equation A.1 is written as:

$$u(z,t) = [\mathcal{C}(e^{\frac{2\alpha}{D_a} i^{1/2} z} + e^{-\frac{2\alpha}{D_a} i^{1/2} z}) - \frac{A_p i}{\rho\omega}]e^{i\omega t} \tag{A.5}$$

Because of the no-slip condition, which requires $u(D_a/2, t) = u(-D_a/2, t) = 0$, it is possible to determine the constant $\mathcal{C}$. Hence, the axial velocity for flow between two parallel plates is written, in its complex form, as:

$$\boxed{u(z,t) = -\frac{A_p i}{\rho\omega}[1 - \frac{\cosh(\alpha i^{1/2} \frac{2z}{D_a})}{\cosh(\alpha i^{1/2})}]e^{i\omega t}} \tag{A.6}$$

from which one must solve for the real part (see Section A.1.1).

However, a prescribed average cross sectional flow of the form $\bar{u}(t) = A\sin\omega t + B\cos\omega t$ is required. Assuming that the width of the channel (in the y-direction) is equal to the distance between the plates, D_a, so that $A_a = D_a^2$, the sectionally averaged velocity is found:

$$\boxed{\bar{u}(t) = -\frac{A_p i}{\rho\omega}[1 - \frac{1}{\alpha i^{1/2}} \tanh(\alpha i^{1/2})]e^{i\omega t}} \tag{A.7}$$

from which one needs to evaluate the real part (see Section A.1.2).

By replacing:

$$-\frac{A_p i}{\rho\omega} = c_r + i \cdot c_i$$

$$1 - \frac{1}{\alpha i^{1/2}} \tanh(\alpha i^{1/2}) = J_r + i \cdot J_i$$

$$1 - \frac{\cosh(\alpha i^{1/2} \frac{2z}{D_a})}{\cosh(\alpha i^{1/2})} = J_r^o(z) + i \cdot J_i^o(z)$$

$\bar{u}(t)$ can be expressed as:

$$\begin{aligned} \bar{u}(t) &= [(c_r J_r - c_i J_i)\cos\omega t - (c_r J_i + c_i J_r)\sin\omega t] \\ &\quad + i \cdot [(c_r J_r - c_i J_i)\sin\omega t + (c_r J_i + c_i J_r)\cos\omega t] \end{aligned}$$

The real part of $\bar{u}(t)$ is therefore $\Re\{\bar{u}(t)\} = (c_r J_r - c_i J_i)\cos\omega t - (c_r J_i + c_i J_r)\sin\omega t$, and equating the sine and cosine terms with the expression for the prescribed cross sectional flow, gives: $A = c_r J_r - c_i J_i, B = -c_r J_i - c_i J_r$.

Substitution of c_i, c_r into the solution of $u(z,t)$ (Equation A.6), gives:

$$\begin{aligned} u(z,t) &= \{[c_r J_r^o(z) - c_i J_i^o(z)]\cos\omega t - [c_r J_i^o(z) + c_i J_r^o(z)]\sin\omega t\} \\ &\quad + i \cdot \{[c_r J_i^o(z) + c_i J_r^o(z)]\cos\omega t + [c_r J_r^o(z) - c_i J_i^o(z)]\sin\omega t\} \end{aligned}$$

Thus, the solution of flow between two parallel plates and prescribed average cross sectional flow is the real part of the above equation, i.e.:

$$\Re\{u(z,t)\} = [c_r J_r^o(z) - c_i J_i^o(z)]\cos\omega t - [c_r J_i^o(z) + c_i J_r^o(z)]\sin\omega t \qquad \text{(A.8)}$$

where

$$c_r = \frac{AJ_r - BJ_i}{J_r^2 + J_i^2}, c_i = \frac{-AJ_i - BJ_r}{J_r^2 + J_i^2}$$

$$J_r = \Re\{1 - \tfrac{1}{\alpha i^{1/2}} \tanh(\alpha i^{1/2})\}$$

$$J_i = \Im\{1 - \tfrac{1}{\alpha i^{1/2}} \tanh(\alpha i^{1/2})\}$$

$$J_r^o = \Re\{1 - \frac{\cosh(\alpha i^{1/2} \frac{2z}{D_a})}{\cosh(\alpha i^{1/2})}\}$$

$$J_i^o = \Im\{1 - \frac{\cosh(\alpha i^{1/2} \frac{2z}{D_a})}{\cosh(\alpha i^{1/2})}\}$$

The expression $\left\{1 - \frac{\cosh(\alpha i^{1/2} \frac{2z}{D_a})}{\cosh(\alpha i^{1/2})}\right\}$ is evaluated in Section A.1.1, from which:

$$J_r^o = \tfrac{1}{\gamma}[\gamma - \cosh \Phi_1 \cos \Phi_2 - \cosh \Phi_2 \cos \Phi_1]$$

$$J_i^o = \tfrac{1}{\gamma}[\sinh \Phi_1 \sin \Phi_2 + \sinh \Phi_2 \sin \Phi_1]$$

The expression $\left\{1 - \frac{1}{\alpha i^{1/2}} \tanh(\alpha i^{1/2})\right\}$ is evaluated in Section A.1.2, thus:

$$J_r = 1 - \frac{1}{\frac{\alpha}{\sqrt{2}}\gamma} \cdot \cosh(\alpha\sqrt{2}) \sin(\alpha\sqrt{2})$$

$$J_i = -\frac{1}{\frac{\alpha}{\sqrt{2}}\gamma} \cdot \cosh(\alpha\sqrt{2}) \sin(\alpha\sqrt{2})$$

where $\gamma = \cosh(\alpha\sqrt{2}) + \cos(\alpha\sqrt{2})$, $\Phi_1 = \frac{\alpha}{\sqrt{2}}(1 + \frac{2z}{D_a})$, $\Phi_2 = \frac{\alpha}{\sqrt{2}}(1 - \frac{2z}{D_a})$.

A.1.1 Evaluation of the real part of Equation A.6

This section presents the analytical evaluation of the real part of Equation A.6:

$$\Re\{u(z,t)\} = \Re\left\{-\frac{A_p i}{\rho\omega}[1 - \frac{\cosh(\alpha i^{1/2}\frac{2z}{D_a})}{\cosh(\alpha i^{1/2})}]e^{i\omega t}\right\} \tag{A.9}$$

It follows:

$$1 - \frac{\cosh(\alpha i^{1/2}\frac{2z}{D_a})}{\cosh(\alpha i^{1/2})}$$

$$= \frac{2\sinh[\frac{\alpha}{2}(1+\frac{2z}{D_a})i^{1/2}]\sinh[\frac{\alpha}{2}(1-\frac{2z}{D_a})i^{1/2}]}{\cosh(\alpha i^{1/2})}$$

$$= \frac{2}{\cosh[\frac{\alpha}{\sqrt{2}}(1+i)]} \cdot \sinh[\frac{\alpha}{2\sqrt{2}}(1+\frac{2z}{D_a})(1+i)]\sinh[\frac{\alpha}{2\sqrt{2}}(1-\frac{2z}{D_a})(1+i)]$$

If $\mathcal{K}_1 = \frac{\alpha}{2\sqrt{2}}(1+\frac{2z}{D_a}), \mathcal{K}_2 = \frac{\alpha}{2\sqrt{2}}(1-\frac{2z}{D_a})$, and $\mathcal{K} = \frac{\alpha}{\sqrt{2}}$, then

$$= \frac{2}{\cosh\mathcal{K}\cos\mathcal{K}+i\cdot\sinh\mathcal{K}\sin\mathcal{K}} \cdot$$
$$(\sinh\mathcal{K}_1\cos\mathcal{K}_1 + i\cdot\cosh\mathcal{K}_1\sin\mathcal{K}_1)\cdot(\sinh\mathcal{K}_2\cos\mathcal{K}_2 + i\cdot\cosh\mathcal{K}_2\sin\mathcal{K}_2)$$

$$= \frac{2}{\cosh^2\mathcal{K}+\cos^2\mathcal{K}-1} \cdot (\cosh\mathcal{K}\cos\mathcal{K} - i\cdot\sinh\mathcal{K}\sin\mathcal{K})\cdot$$
$$[(\sinh\mathcal{K}_1\cos\mathcal{K}_1\sinh\mathcal{K}_2\cos\mathcal{K}_2 - \cosh\mathcal{K}_1\sin\mathcal{K}_1\cosh\mathcal{K}_2\sin\mathcal{K}_2)$$
$$+i\cdot(\sinh\mathcal{K}_1\cos\mathcal{K}_1\cosh\mathcal{K}_2\sin\mathcal{K}_2 + \cosh\mathcal{K}_1\sin\mathcal{K}_1\sinh\mathcal{K}_2\cos\mathcal{K}_2)]$$

$$= \frac{2}{\frac{1}{2}[\cosh(\alpha\sqrt{2})+\cos(\alpha\sqrt{2})]} \cdot$$
$$\{[(\sinh\mathcal{K}_1\cos\mathcal{K}_1\sinh\mathcal{K}_2\cos\mathcal{K}_2 - \cosh\mathcal{K}_1\sin\mathcal{K}_1\cosh\mathcal{K}_2\sin\mathcal{K}_2)\cosh\mathcal{K}\cos\mathcal{K}$$
$$+(\sinh\mathcal{K}_1\cos\mathcal{K}_1\cosh\mathcal{K}_2\sin\mathcal{K}_2 + \cosh\mathcal{K}_1\sin\mathcal{K}_1\sinh\mathcal{K}_2\cos\mathcal{K}_2)\sinh\mathcal{K}\sin\mathcal{K}]$$
$$+i\cdot[-(\sinh\mathcal{K}_1\cos\mathcal{K}_1\sinh\mathcal{K}_2\cos\mathcal{K}_2 - \cosh\mathcal{K}_1\sin\mathcal{K}_1\cosh\mathcal{K}_2\sin\mathcal{K}_2)\sinh\mathcal{K}\sin\mathcal{K}$$
$$+(\sinh\mathcal{K}_1\cos\mathcal{K}_1\cosh\mathcal{K}_2\sin\mathcal{K}_2 + \cosh\mathcal{K}_1\sin\mathcal{K}_1\sinh\mathcal{K}_2\cos\mathcal{K}_2)\cosh\mathcal{K}\cos\mathcal{K}]\}$$

$$= \frac{4}{\gamma}\cdot\{\mathcal{O} + i\cdot\Theta\}$$

where $\gamma = \cosh(\alpha\sqrt{2})+\cos(\alpha\sqrt{2})$ and $\mathcal{O}$, Θ are, respectively, the real and imaginary parts of the above complex expression within the braces.

Equation A.6 can now be expressed as:

$$\begin{aligned} u(z,t) &= -\tfrac{A_p i}{\rho\omega}\cdot\tfrac{4}{\gamma}\cdot\{\mathcal{O}+i\cdot\Theta\}\cdot e^{i\omega t} \\ &= \frac{4A_p}{\rho\omega\gamma}\cdot\{[\Theta\cos\omega t+\mathcal{O}\sin\omega t]+i\cdot[\Theta\sin\omega t-\mathcal{O}\cos\omega t]\} \end{aligned}$$

The real part of $u(z,t)$ is then $\Re\{u(z,t)\}=\dfrac{4A_p}{\rho\omega\gamma}\cdot[\Theta\cos\omega t+\mathcal{O}\sin\omega t]$.

More compact expressions for Θ and $\mathcal{O}$ can be found as follows:

$$\begin{aligned} \Theta &= -(\sinh\mathcal{K}_1\cos\mathcal{K}_1\sinh\mathcal{K}_2\cos\mathcal{K}_2-\cosh\mathcal{K}_1\sin\mathcal{K}_1\cosh\mathcal{K}_2\sin\mathcal{K}_2)\sinh\mathcal{K}\sin\mathcal{K} \\ &\quad +(\sinh\mathcal{K}_1\cos\mathcal{K}_1\cosh\mathcal{K}_2\sin\mathcal{K}_2+\cosh\mathcal{K}_1\sin\mathcal{K}_1\sinh\mathcal{K}_2\cos\mathcal{K}_2)\cosh\mathcal{K}\cos\mathcal{K} \\ &= \tfrac{1}{4}\{-[\cosh(\mathcal{K}_1+\mathcal{K}_2)-\cosh(\mathcal{K}_1-\mathcal{K}_2)][\cos(\mathcal{K}_1-\mathcal{K}_2)+\cos(\mathcal{K}_1+\mathcal{K}_2)] \\ &\quad +[\cosh(\mathcal{K}_1+\mathcal{K}_2)+\cosh(\mathcal{K}_1-\mathcal{K}_2)][\cos(\mathcal{K}_1-\mathcal{K}_2)-\cos(\mathcal{K}_1+\mathcal{K}_2)]\}\sinh\mathcal{K}\sin\mathcal{K} \\ &\quad +\tfrac{1}{4}\{[\sinh(\mathcal{K}_1+\mathcal{K}_2)+\sinh(\mathcal{K}_1-\mathcal{K}_2)][-\sin(\mathcal{K}_1-\mathcal{K}_2)+\sin(\mathcal{K}_1+\mathcal{K}_2)] \\ &\quad +[\sinh(\mathcal{K}_1+\mathcal{K}_2)-\sinh(\mathcal{K}_1-\mathcal{K}_2)][\sin(\mathcal{K}_1-\mathcal{K}_2)+\sin(\mathcal{K}_1+\mathcal{K}_2)]\}\cosh\mathcal{K}\cos\mathcal{K} \\ &= \tfrac{1}{2}\{[-\cosh(\mathcal{K}_1+\mathcal{K}_2)\cos(\mathcal{K}_1+\mathcal{K}_2)+\cosh(\mathcal{K}_1-\mathcal{K}_2)\cos(\mathcal{K}_1-\mathcal{K}_2)]\sinh\mathcal{K}\sin\mathcal{K} \\ &\quad +[\sinh(\mathcal{K}_1+\mathcal{K}_2)\sin(\mathcal{K}_1+\mathcal{K}_2)-\sinh(\mathcal{K}_1-\mathcal{K}_2)\sin(\mathcal{K}_1-\mathcal{K}_2)]\cosh\mathcal{K}\cos\mathcal{K}\} \\ &= \tfrac{1}{2}\{-\tfrac{1}{4}[\sinh(\mathcal{K}+\mathcal{K}_1+\mathcal{K}_2)+\sinh(\mathcal{K}-\mathcal{K}_1-\mathcal{K}_2)][\sin(\mathcal{K}-\mathcal{K}_1-\mathcal{K}_2)+\sin(\mathcal{K}+\mathcal{K}_1+\mathcal{K}_2)] \\ &\quad +\tfrac{1}{4}[\sinh(\mathcal{K}+\mathcal{K}_1-\mathcal{K}_2)+\sinh(\mathcal{K}-\mathcal{K}_1+\mathcal{K}_2)][\sin(\mathcal{K}-\mathcal{K}_1+\mathcal{K}_2)+\sin(\mathcal{K}+\mathcal{K}_1-\mathcal{K}_2)] \\ &\quad +\tfrac{1}{4}[\sinh(\mathcal{K}+\mathcal{K}_1+\mathcal{K}_2)-\sinh(\mathcal{K}-\mathcal{K}_1-\mathcal{K}_2)][-\sin(\mathcal{K}-\mathcal{K}_1-\mathcal{K}_2)+\sin(\mathcal{K}+\mathcal{K}_1+\mathcal{K}_2)] \\ &\quad -\tfrac{1}{4}[\sinh(\mathcal{K}+\mathcal{K}_1-\mathcal{K}_2)-\sinh(\mathcal{K}-\mathcal{K}_1+\mathcal{K}_2)][-\sin(\mathcal{K}-\mathcal{K}_1+\mathcal{K}_2)+\sin(\mathcal{K}+\mathcal{K}_1-\mathcal{K}_2)]\} \\ &= \tfrac{1}{4}[-\sinh(\mathcal{K}+\mathcal{K}_1+\mathcal{K}_2)\sin(\mathcal{K}-\mathcal{K}_1-\mathcal{K}_2)-\sinh(\mathcal{K}-\mathcal{K}_1-\mathcal{K}_2)\sin(\mathcal{K}+\mathcal{K}_1+\mathcal{K}_2) \\ &\quad +\sinh(\mathcal{K}+\mathcal{K}_1-\mathcal{K}_2)\sin(\mathcal{K}-\mathcal{K}_1+\mathcal{K}_2)+\sinh(\mathcal{K}-\mathcal{K}_1+\mathcal{K}_2)\sin(\mathcal{K}+\mathcal{K}_1-\mathcal{K}_2)] \end{aligned}$$

However:

$$\begin{aligned} \mathcal{K}+\mathcal{K}_1+\mathcal{K}_2 &= \alpha\sqrt{2} \\ \mathcal{K}-\mathcal{K}_1-\mathcal{K}_2 &= 0 \\ \Phi_1 = \mathcal{K}+\mathcal{K}_1-\mathcal{K}_2 &= \tfrac{\alpha}{\sqrt{2}}(1+\tfrac{2z}{D_a}) \\ \Phi_2 = \mathcal{K}-\mathcal{K}_1+\mathcal{K}_2 &= \tfrac{\alpha}{\sqrt{2}}(1-\tfrac{2z}{D_a}) \end{aligned}$$

Therefore:

$$\Theta = \frac{1}{4}[\sinh\Phi_1 \sin\Phi_2 + \sinh\Phi_2 \sin\Phi_1] \tag{A.10}$$

Similarly:

$$\begin{aligned} \mathcal{O} &= (\sinh\mathcal{K}_1\cos\mathcal{K}_1\sinh\mathcal{K}_2\cos\mathcal{K}_2 - \cosh\mathcal{K}_1\sin\mathcal{K}_1\cosh\mathcal{K}_2\sin\mathcal{K}_2)\cosh\mathcal{K}\cos\mathcal{K} \\ &\quad +(\sinh\mathcal{K}_1\cos\mathcal{K}_1\cosh\mathcal{K}_2\sin\mathcal{K}_2 + \cosh\mathcal{K}_1\sin\mathcal{K}_1\sinh\mathcal{K}_2\cos\mathcal{K}_2)\sinh\mathcal{K}\sin\mathcal{K} \\ &= \tfrac{1}{2}\{[\cosh(\mathcal{K}_1+\mathcal{K}_2)\cos(\mathcal{K}_1+\mathcal{K}_2) - \cosh(\mathcal{K}_1-\mathcal{K}_2)\cos(\mathcal{K}_1-\mathcal{K}_2)]\cosh\mathcal{K}\cos\mathcal{K} \\ &\quad +[\sinh(\mathcal{K}_1+\mathcal{K}_2)\sin(\mathcal{K}_1+\mathcal{K}_2) - \sinh(\mathcal{K}_1-\mathcal{K}_2)\sin(\mathcal{K}_1-\mathcal{K}_2)]\sinh\mathcal{K}\sin\mathcal{K}\} \\ &= \tfrac{1}{4}[\cosh(\mathcal{K}+\mathcal{K}_1+\mathcal{K}_2)\cos(\mathcal{K}-\mathcal{K}_1-\mathcal{K}_2) + \cosh(\mathcal{K}-\mathcal{K}_1-\mathcal{K}_2)\cos(\mathcal{K}+\mathcal{K}_1+\mathcal{K}_2) \\ &\quad -\cosh(\mathcal{K}+\mathcal{K}_1-\mathcal{K}_2)\cos(\mathcal{K}-\mathcal{K}_1+\mathcal{K}_2) - \cosh(\mathcal{K}-\mathcal{K}_1+\mathcal{K}_2)\cos(\mathcal{K}+\mathcal{K}_1-\mathcal{K}_2)] \\ &= \tfrac{1}{4}[\cosh(\alpha\sqrt{2}) + \cos(\alpha\sqrt{2}) - \cosh\Phi_1\cos\Phi_2 - \cosh\Phi_2\cos\Phi_1] \\ &= \tfrac{1}{4}[\gamma - \cosh\Phi_1\cos\Phi_2 - \cosh\Phi_2\cos\Phi_1] \end{aligned}$$

Hence:

$$\boxed{\begin{aligned} \Re\{u(z,t)\} = \frac{A_p}{\rho\omega\gamma}\cdot\{&[\sinh\Phi_1\sin\Phi_2 + \sinh\Phi_2\sin\Phi_1]\cos\omega t \\ &+[\gamma - \cosh\Phi_1\cos\Phi_2 - \cosh\Phi_2\cos\Phi_1]\sin\omega t\} \end{aligned}} \tag{A.11}$$

where

$$\begin{aligned} \gamma &= \cosh(\alpha\sqrt{2}) + \cos(\alpha\sqrt{2}) \\ \Phi_1 &= \frac{\alpha}{\sqrt{2}}(1+\frac{2z}{D_a}) \\ \Phi_2 &= \frac{\alpha}{\sqrt{2}}(1-\frac{2z}{D_a}) \end{aligned}$$

A.1.2 Evaluation of the expression appearing in Equation A.7

The following expression appears in Equation A.7 and can be evaluated as follows:

$$1 - \frac{1}{\alpha i^{1/2}} \tanh(\alpha i^{1/2})$$

$$= 1 - \frac{1}{\frac{\alpha}{\sqrt{2}}(1+i)} \frac{\sinh[\frac{\alpha}{\sqrt{2}}(1+i)]}{\cosh[\frac{\alpha}{\sqrt{2}}(1+i)]}$$

$$= 1 - \frac{1}{\frac{\alpha}{\sqrt{2}}(1+i)} \frac{\sinh(\frac{\alpha}{\sqrt{2}})\cos(\frac{\alpha}{\sqrt{2}}) + i\cdot\cosh(\frac{\alpha}{\sqrt{2}})\sin(\frac{\alpha}{\sqrt{2}})}{\cosh(\frac{\alpha}{\sqrt{2}})\cos(\frac{\alpha}{\sqrt{2}}) + i\cdot\sinh(\frac{\alpha}{\sqrt{2}})\sin(\frac{\alpha}{\sqrt{2}})}$$

If $\mathcal{K} = \frac{\alpha}{\sqrt{2}}$, then

$$= 1 - \frac{1}{\mathcal{K}} \frac{(1-i)(\cosh\mathcal{K}\cos\mathcal{K} - i\cdot\sinh\mathcal{K}\sin\mathcal{K})}{2[(\cosh\mathcal{K}\cos\mathcal{K})^2 + (\sinh\mathcal{K}\sin\mathcal{K})^2]} \cdot [\sinh\mathcal{K}\cos\mathcal{K} + i\cdot\cosh\mathcal{K}\sin\mathcal{K}]$$

$$= 1 - \frac{1}{4\mathcal{K}} \frac{(1-i)}{\frac{1}{2}[\cosh(\alpha\sqrt{2}) + \cos(\alpha\sqrt{2})]} \cdot i \cdot 2\cosh(2\mathcal{K})\sin(2\mathcal{K})$$

$$= [1 - \frac{1}{\frac{\alpha}{\sqrt{2}}\gamma} \cdot \cosh(\alpha\sqrt{2})\sin(\alpha\sqrt{2})] - i\cdot[\frac{1}{\frac{\alpha}{\sqrt{2}}\gamma} \cdot \cosh(\alpha\sqrt{2})\sin(\alpha\sqrt{2})]$$

where $\gamma = \cosh(\alpha\sqrt{2}) + \cos(\alpha\sqrt{2})$.

A.2 Volume flow rate for flow in a channel

The volume flow rate of a fluid flow in a channel, found by integration of the velocity [Equation (A.11)] over the full height channel inflow area D_a^2, can be expressed as:

$$Q(t) = \frac{A_p D_a^4}{4\mu\alpha^3}$$

$$\cdot\sqrt{\left[\frac{\sinh(\alpha\sqrt{2})}{\gamma}\right]^2 + \left[\frac{\sin(\alpha\sqrt{2})}{\gamma}\right]^2 - \frac{\alpha\sqrt{2}[\sinh(\alpha\sqrt{2}) + \sin(\alpha\sqrt{2})]}{\gamma} + \alpha^2} \quad \text{(A.12)}$$

$$\cdot \sin(\omega t + \theta)$$

where

$$\theta = \arctan\left[\frac{\sinh(\alpha\sqrt{2}) - \sin(\alpha\sqrt{2})}{\alpha\gamma\sqrt{2} - \sinh(\alpha\sqrt{2}) - \sin(\alpha\sqrt{2})}\right]$$

$$\gamma = \cosh(\alpha\sqrt{2}) + \cos(\alpha\sqrt{2})$$

A.3 Figures of Chapter 3 in grayscale

Because some features show better in grayscale, this section presents grayscale versions of the WSS_n patterns presented in Chapter 3. No further comments are given. The figure numbers corresponding to those of Chapter 3 are also provided.

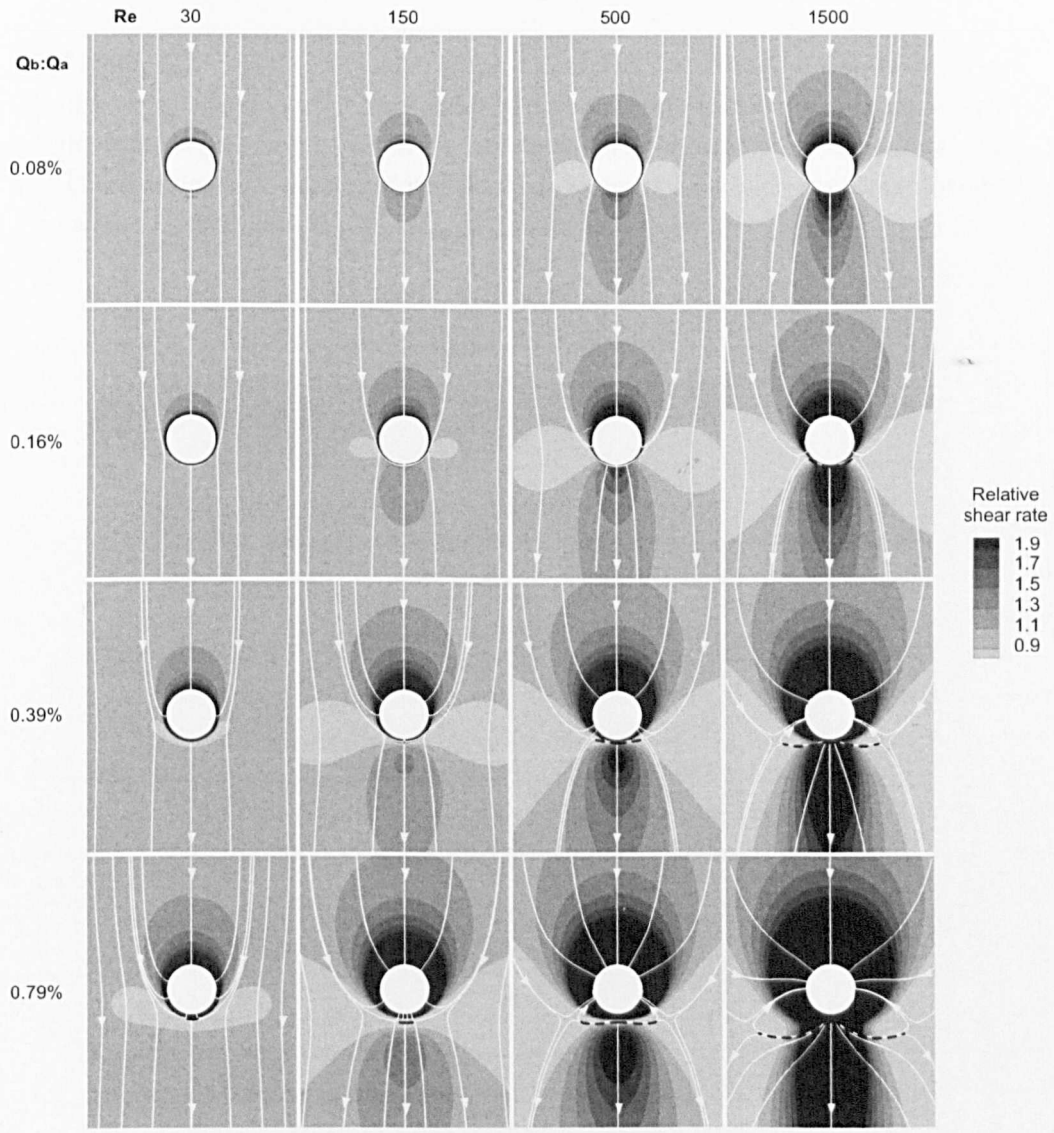

Figure A.1: (Grayscale of Figure 3.4) Magnitude and direction of non-dimensionalised aortic wall shear stress around the ostium of the simple intercostal junction of Figure 3.1a. Mean aortic flow is from top to bottom. The simulations were performed at a range of Reynolds numbers and flow partitions to account for different species and ages within a species. Dashed lines indicate flow attachment.

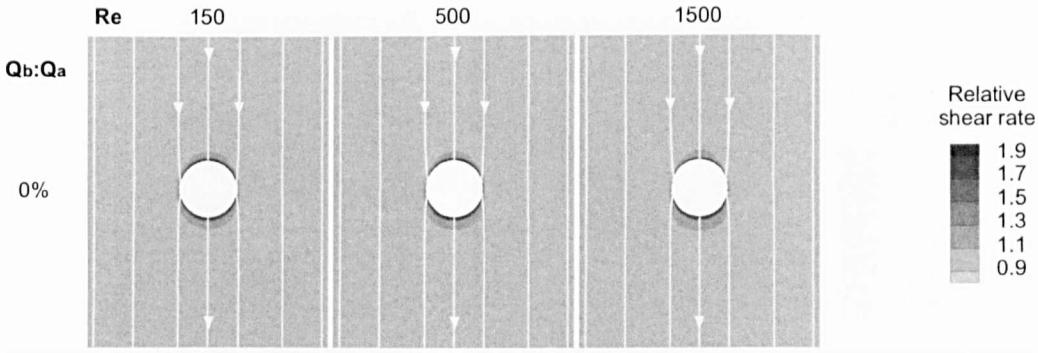

Figure A.2: (Grayscale of Figure 3.5) Magnitude and direction of non-dimensionalised aortic wall shear stress around the ostium of the simple intercostal junction of Figure 3.1a Mean aortic flow is from top to bottom. The simulations were performed at a range of Reynolds numbers for the case of ligated side branch ($Q_b = 0$).

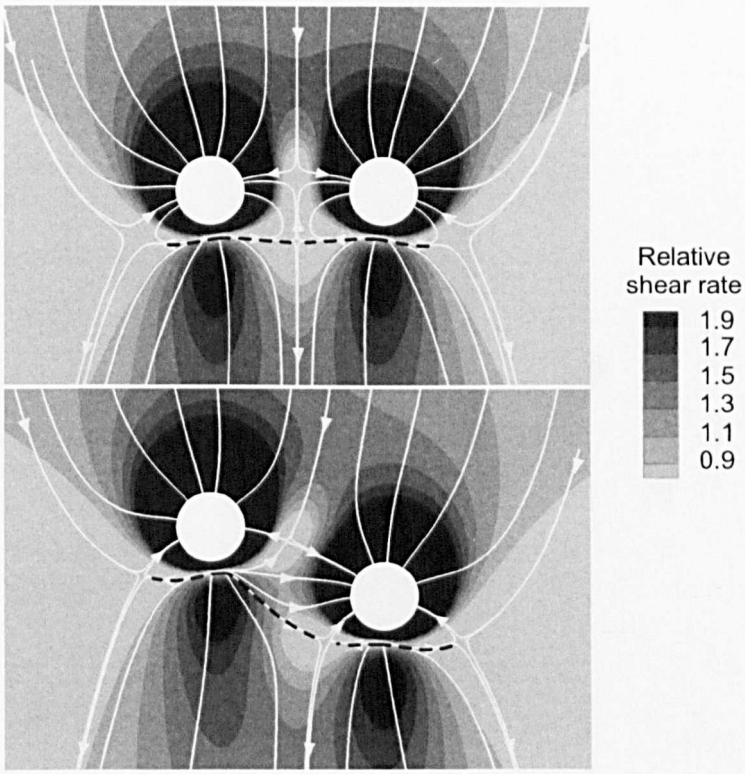

Figure A.3: (Grayscale of Figure 3.6) Magnitude and direction of non-dimensionalised aortic wall shear stress around a pair of intercostal ostia at the same streamwise position (top, Figure 3.1d) and at staggered positions (bottom). Mean aortic flow is from top to bottom. The simulations were performed for $Re = 500$ and Q_b:$Q_a = 0.79\%$. Dashed lines indicate flow attachment.

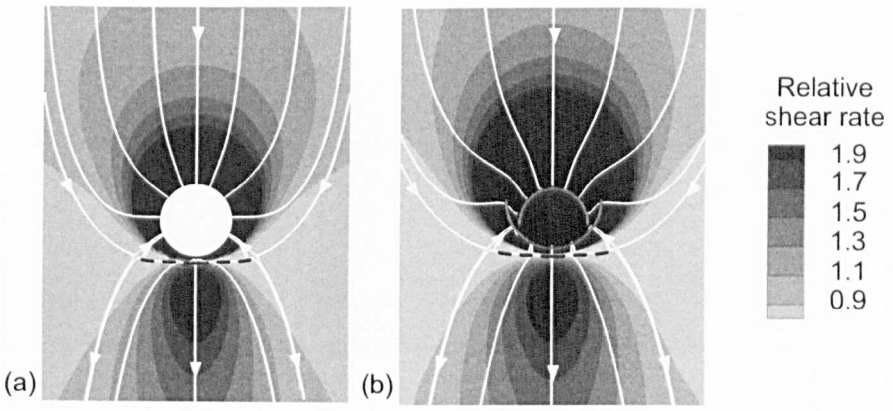

Figure A.4: (Grayscale of Figure 3.7) Magnitude and direction of non-dimensionalised aortic wall shear stress around the ostium of (a) the aortic model of Figure 3.1b and (b) the realistic aorto-intercostal junction of Figure 3.1c. Mean aortic flow is from top to bottom. The simulations were performed for $Re = 500$ and Q_b:$Q_a = 0.79\%$. Dashed lines indicate flow attachment.

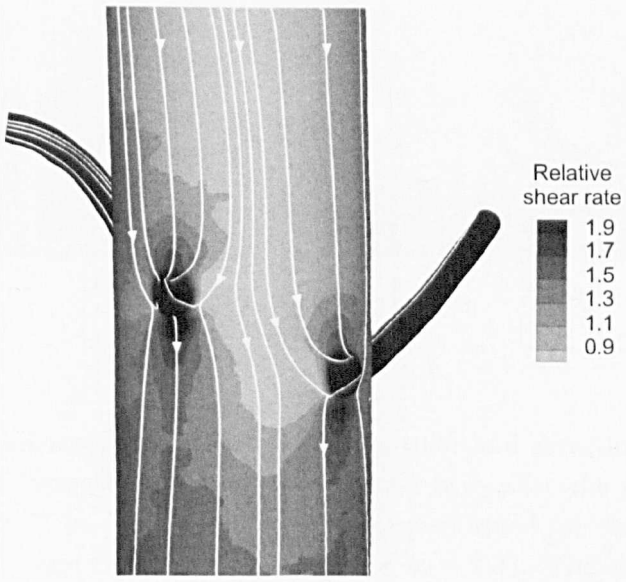

Figure A.5: (Grayscale of Figure 3.8, right image) Magnitude and direction of non-dimensionalised aortic wall shear stress in the anatomically correct geometry of Figure 3.3.Mean aortic flow is from top to bottom. The simulations were performed for $Re_{D_a^r} = 500$ and Q_b^r:$Q_a^r = 0.79\%$.

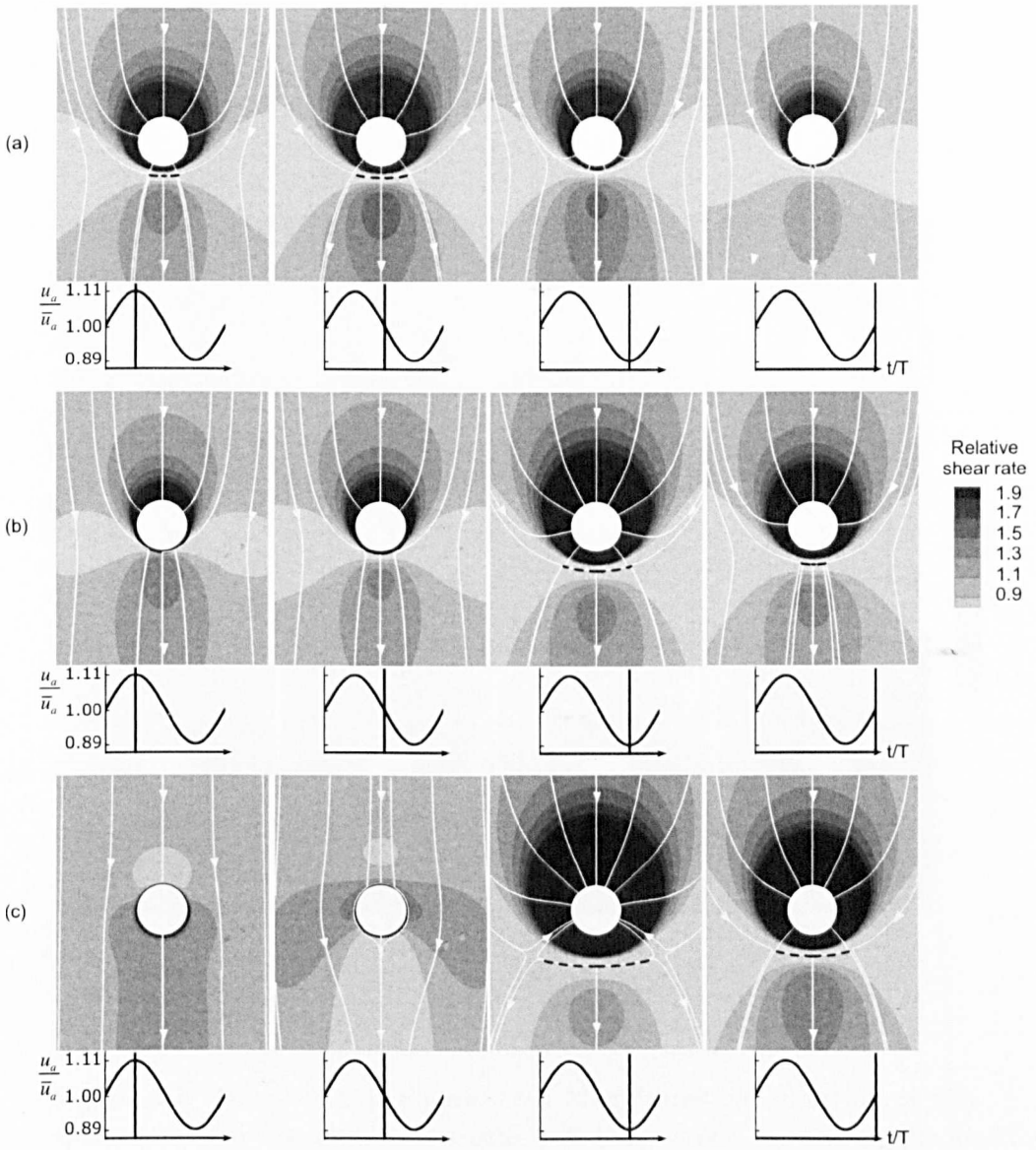

Figure A.6: (Grayscale of Figure 3.9) Magnitude and direction of non-dimensionalised instantaneous aortic wall shear stress for the simple geometry of Figure 3.1a. The simulations were performed for $Re_m = 150$, Q_b:$Q_{a_m} = 0.79\%$ and $U_{red} = 4$ (St = 0.25 or $\alpha \approx 7.7$). The side branch flow waveform had a phase shift with the aortic waveform of (a) $\phi = 0$, (b-c) $\phi = \pi$. In (c) the side branch flow was reversing for about one third of the cycle. Mean aortic flow is from top to bottom. Dashed lines indicate flow attachment.

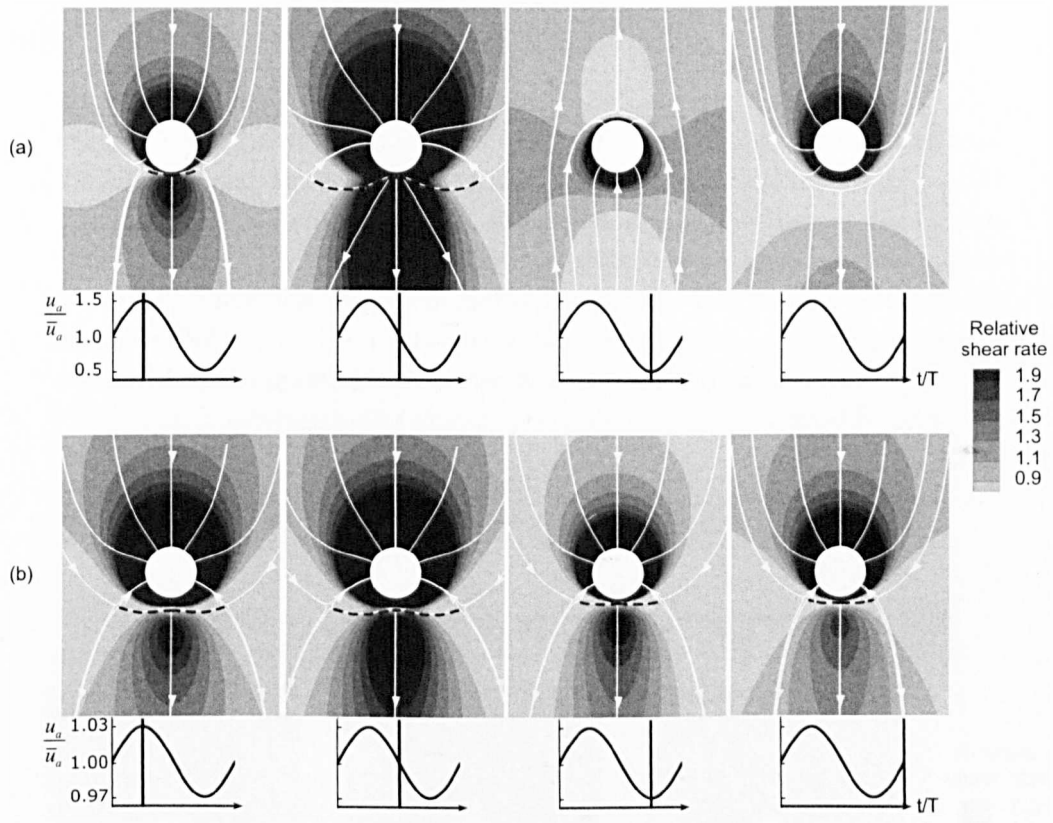

Figure A.7: (Grayscale of Figure 3.10) Magnitude and direction of non-dimensionalised instantaneous aortic wall shear stress for the simple geometry of Figure 3.1a.The simulations were performed for $Re_m = 500$, Q_b:$Q_{a_m} = 0.79\%$, $U_{red} = 4$ (St = 0.25 or $\alpha \approx 14$) and $\phi = 0$. The aortic waveform had a peak-to-mean of (a) 1.5 and (b) 1.03. Mean aortic flow is from top to bottom. Dashed lines indicate flow attachment.

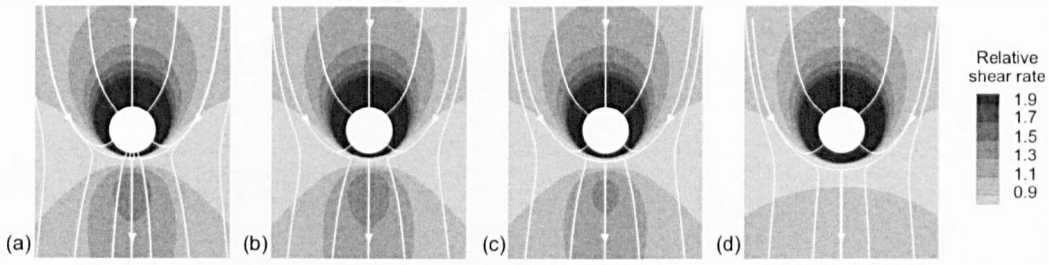

Figure A.8: (Grayscale of Figure 3.11) Magnitude and direction of non-dimensionalised time-averaged aortic wall shear stress for $Re_m = 150$, Q_b:$Q_{a_m} = 0.79\%$ and $U_{red} = 4$, corresponding to the instantaneous patterns of Figure 3.9. (a) Steady flow result at the same mean flow values. The side branch flow waveform had a phase shift, with respect to the aortic waveform, of (b) $\phi = 0$, (c-d) $\phi = \pi$, and in (d) it was reversing for about one third of the cycle. Mean aortic flow is from top to bottom.

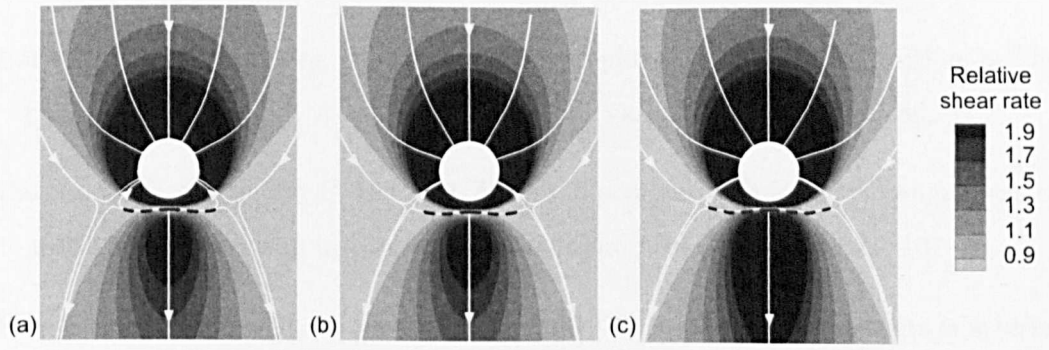

Figure A.9: (Grayscale of Figure 3.12) Magnitude and direction of non-dimensionalised time-averaged aortic wall shear stress for $Re_m = 500$, Q_b:$Q_{a_m} = 0.79\%$, and $U_{red} = 4$ ($\phi = 0$), corresponding to the instantaneous patterns of Figure 3.10. (a) Steady flow result at the same mean flow values. The aortic waveform had a peak-to-mean of (b) 1.03 (Figure 3.10b) and (c) 1.5 (Figure 3.10a). Mean aortic flow is from top to bottom.

Bibliography

Abrahams, P. H., 2001. McMinn's interactive clinical anatomy (CD-ROM 2.0). Mosby.

Ajjan, R., Grant, P. J., 2006. Coagulation and atherothrombotic disease. Atherosclerosis 186, 240–259.

Al-Musawi, S. L., Bishton, J., Dean, J., Williams, S., Cremers, S. G., Weinberg, P. D., 2004. Evidence for a reversal with age in the pattern of near-wall blood flow around aortic branches. Atherosclerosis 172, 79–84.

Barnes, S. E., Weinberg, P. D., 1998. Contrasting patterns of spontaneous aortic disease in young and old rabbits. Arterioscler. Thromb. Vasc. Biol. 18, 300–308.

Barnes, S. E., Weinberg, P. D., 1999. Two patterns of lipid deposition in the cholesterol-fed rabbit. Arterioscler. Thromb. Vasc. Biol. 19, 2376–2386.

Barnes, S. E., Weinberg, P. D., 2001. Strain-dependent differences in the pattern of aortic lipid deposition in cholesteol-fed rabbits. Exp. Mol. Path. 71, 161–70.

Bergel, D. H., Nerem, R. M., Schwartz, C. J., 1976. Fluid dynamic aspects of arterial disease. Atherosclerosis 23, 253–261.

Bond, A. R., Weinberg, P. D., 2006. Haemodynamic stresses and wall structure can account for the pattern of lipid deposition around aortic branches in mice. Atherosclerosis suppl 7, 200. Abstract.

Buchanan Jr., J. R., Kleinstreuer, C., Truskey, G. A., Lei, M., 1999. Relation between non-uniform hemodynamics and sites of altered permeability and lesion growth at the rabbit aorto-celiac junction. Atherosclerosis 143, 27–40.

Caro, C. G., 2001. Vascular fluid dynamics and vascular biology and disease. Math. Meth. Appl. Sci. 24 (17-18), 1311–1324.

Caro, C. G., Doorly, D. J., Tarnawski, M., Scott, K. T., Long, Q., Dumoulin, C. L., 1996. Non-planar curvature and branching of arteries and non-planar-type flow. Proc. R. Soc. Lond. A 452, 185–197.

Caro, C. G., Fitz-Gerald, J. M., Schroter, R. C., 1971. Atheroma and arterial wall shear. observation, correlation and proposal of a shear dependent mass transfer mechanism for atherogenesis. Proc. R. Soc. Lond. B Biol. Sci. 177 (46), 109–159.

Caro, C. G., Parker, K. H., Fish, P. J., Lever, M. J., 1985. Blood flow near the arterial wall and arterial disease. Clin. Hemorheol. 5 (6), 849–871.

Caro, C. G., Pedley, T. J., Schroter, R. C., Seed, W. A., 1978. The mechanics of the circulation. Oxford University Press.

Caro, C. G., Schroter, R. C., Watkins, N., Sherwin, S. J., Sauret, V., 2002. Steady inspiratory flow in planar and non-planar models of human bronchial airways. Proc. R.Soc. Lond. A 458, 701–809.

Cheer, A. Y., Dwyer, H. A., Barakat, A. I., Sy, E., Bice, M., 1998. Computational study of the effect of geometric and flow parameters on the steady flow field at the rabbit aorto-celiac bifurcation. Biorheology 35 (6), 415–435.

Cheng, C., Helderman, F., Tempel, D., Segers, D., Hierck, B., Poelmann, R., van Tol, A., Duncker, D. J., Robbers-Visser, D., Ursem, N. T., van Haperen, R., Wentzel, J. J., Gijsen, F., van der Steen, A. F., de Crom, R., Krams, R., 2007. Large variations in absolute wall shear stress levels within one species and between species. Atherosclerosis 195, 225–235.

Coppola, G., Sherwin, S. J., Peiró, J., 2001. Nonlinear particle tracking for high-order elements. J. Comput. Phys. 172 (1), 356–386.

Cornhill, J. F., Levesque, M. J., Nerem, R. M., 1980. Quantitative study of the localization of sudanophilic coeliac lesions in the white carneau pigeon. Atherosclerosis 35, 103–110.

Cornhill, J. F., Roach, M. R., 1976. A quantitative study of the localization of atherosclerotic lesions in the rabbit aorta. Atherosclerosis 23, 489–501.

Davies, P. F., 1995. Flow-mediated endothelial mechanotransduction. Physiol. Rev. 75 (3), 519–560.

DeMestre, N. J., Guiney, D. C., 1971. Low Reynolds number oscillatory flow through a hole in a wall. J. Fluid Mech. 47 (4), 657–666.

Eskillson, C., Sherwin, S., 2005. An introduction to spectral/*hp* element methods for hyperbolic problems. In: EUA4X Marie Curie training course. 34th CFD Very high-order discretization methods. Belgium.

Ethier, R. C., 2005. Haemodynamics gets small, Aerodynamics seminar, Dept. Aeronautics, Imperial College London, 11 May 2005, UK.

Farthing, S., 1978. Flow in the thoracic aorta and its relation to atherogenesis. PhD Thesis, University of Cambridge.

Feintuch, A., Ruengsakulrach, P., Lin, A., Zhang, J., Zhou, Y. Q., Bishop, J., Davidson, L., Courtman, D., Foster, F. S., Steinman, D. A., Henkelman, R. M., Ethier, C. R., 2007. Hemodynamics in the mouse aortic arch as assessed by MRI, ultrasound, and numerical modeling. Am. J. Physiol. Heart Circ. Physiol. 292, H884–H892.

Ferziger, J. H., Perić, M., 2002. Computational methods for fluid dynamics, 3rd Edition. Springer-Verlag.

Fry, D. L., 1969. Certain chemorheologic considerations regarding the blood vascular interface with particular reference to coronary artery disease. Circulation 40 (5S4), 38–57.

Giordana, S., 2004. Geometrical reconstruction from medical images, classification and modelling of arterial by-pass grafts. Ph.D. thesis, Imperial College London.

Giordana, S., Sherwin, S. J., Peiró, J., Doorly, D. J., Crane, J. S., Lee, K. E., Cheshire, N. J., Caro, C. G., 2005a. Local and global goemetric influence on steady flow in distal anastomoses of peripheral by-pass grafts. J. Biomech. Eng. 127 (7), 1087–1098.

Giordana, S., Sherwin, S. J., Peiró, J., Doorly, D. J., Papaharilaou, Y., Caro, C. G., Watkins, N., Cheshire, N., Jackson, M., Bicknall, C., Zervas, V., 2005b. Automated classification of peripheral distal by-pass geometries reconstructed from medical data. J. Biomech. 38, 47–62.

Greve, J. M., Les, A. S., Tang, B. T., Blomme, M. T. D., Wilson, N. M., Dalman, R. L., Pelc, N. J., Taylor, C. A., 2006. Allometric scaling of wall shear stress from mice to humans: Quantification using cine phase-contrast mri and computational fluid dynamics. Am. J. Physiol. Heart Circ. Physiol. 291, H1700–H1708.

Hansson, G. K., Robertson, A. L., Söderberg-Nauclér, C., 2006. Inflammation and atherosclerosis. Annu. Rev. Pathol. Mech. Dis. 1, 297–329.

Hartley, C. J., Reddy, A. K., Madala, S., Martin-McNulty, B., Vergona, R., Sullivan, M. E., Halks-Miller, M., Taffet, G. E., Michael, L. H., Entman, M. L., Wang, Y., 2000. Hemodynamic changes in apolipoprotein E-knockout mice. Am. J. Physiol. Heart Circ. Physiol. 279, H2326–H2334.

He, X., Ku, D., 1996. Pulsatile flow in the human left coronary artery bifurcation. J. Biomech. Eng. 118, 74–82.

Hydon, P. E., Pedley, T. J., 1993. Axial dispersion in a channel with oscillating walls. J. Fluid Mech. 249, 535–555.

Iiyama, K., Hajra, L., Iiyama, M., Li, H., DiChiara, M., Medoff, B. D., Cybulsky, M. I., 1999. Patterns of vascular cell adhesion molecule-1 and intercellular adhesion molecule-1 expression in rabbit and mouse atherosclerotic lesions and at sites predisposed to lesion formation. Circ. Res. 85, 199–207.

Jin, S., Oshinski, J., Giddens, D. P., 2003. Effects of wall motion and compliance on flow patterns in the ascending aorta. J. Biomech. Eng. 125, 347–354.

Johnson, J. L., Jackson, C. L., 2001. Atherosclerotic plaque rupture in the apolipoprotein E knockout mouse. Atherosclerosis 154 (2), 399–406.

Karniadakis, G. E., Israeli, M., Orszagc, S. A., 1991. High-order splitting methods for the incompressible Navier-Stokes equations. J. Comput. Phys. 97 (2), 414–443.

Karniadakis, G. E., Sherwin, S. J., 2005. Spectral/*hp* element methods for computational fluid dynamics, 2nd Edition. Oxford Science Publications.

Kazakidi, A., Sherwin, S. J., Weinberg, P. D., 2006. Alteration of Reynolds number and flow partition modify wall shear stresses at arterial branches in a way that can explain age- and species-dependent patterns of arterial disease. J. Biomech. 39 (S1), S611.

Kazakidi, A., Sherwin, S. J., Weinberg, P. D., 2007. Reverse flow in arterial branches influences wall shear stress patterns around branch ostia. Heart 93, e2.

Kazakidi, A., Sherwin, S. J., Weinberg, P. D., 2008. Effect of Reynolds number and flow division on patterns of haemodynamic wall shear stress near branch points in the descending thoracic aorta. Published online J. R. Soc. Interface, doi:10.1098/rsif.2008.0323.

Krams, R., Segers, D., Gourabi, B. M., Maat, W., Cheng, C., van Pelt, C., van Damme, L. C. A., de Feyter, P., van der Steen, T., de Korte, C. L., Serruys, P. W., 2003. Inflammation and atherosclerosis: Mechanisms underlying vulnerable plaque. J. Interv. Cardiol. 16 (2), 107–113.

Ku, D. N., Giddens, D. P., Zarins, C. K., Glagov, S., 1985. Pulsatile flow and atherosclerosis in the human carotid bifurcation. Positive correlation between plaque location and low oscillating shear stress. Arteriosclerosis 5 (3), 293–302.

Landau, L. D., Lifshitz, E. M., 1959. Fluid Mechanics. Pergamon Press.

Langheinrich, A. C., Kampschulte, M., Buch, T., Bohle, R. M., 2007. Vasa vasorum and atherosclerosis—Quid novi? Thromb. Haemost. 97, 873–879.

Langille, B. L., Adamson, S. L., 1981. Relationship between blood flow direction and endothelial cell orientation at arterial branch sites in rabbits and mice. Circ. Res. 48, 481–488.

Loudon, C., Tordesillas, A., 1998. The use of the dimensionless Womersley number to characterize the unsteady nature of internal flow. J. Theor. Biol. 191 (1), 63–78.

Lucas, A. D., Greaves, D. R., 2001. Atherosclerosis: role of chemokines and macrophages. Expert. Rev. Mol. Med. 3, 1–18.

Lygate, C. A., Schneider, J. E., Hulbert, K., ten Hove, M., Sebag-Montefiore, L. M., Cassidy, P. J., Clarke, K., Neubauer, S., 2006. Serial high resolution 3D-MRI after aortic banding in mice: band internalization is a source of variability in the hypertrophic response. Basic Res. Cardiol. 101, 8–16.

Malek, A. M., Alper, S. L., Izumo, S., 1999. Hemodynamic shear stress and its role in atherosclerosis. J. Am. Med. Assoc. 282 (21), 2035–2042.

Mayerl, C., Lukasser, M., Sedivy, R., Niederegger, H., Seiler, R., Wick, G., 2006. Atherosclerosis research from past to present—on the track of two pathologists with opposing views, Carl von Rokitansky and Rudolf Virchow. Virchows Archiv 449 (1), 96–103.

McAteer, M. A., Schneider, J. S., Clarke, K., Neubauer, S., Channon, K. M., Choudhury, R. P., 2004. Quantification and 3D reconstruction of atherosclerotic plaque components in apolipoprotein E knockout mice using ex vivo high-resolution MRI. Arterioscler. Thromb. Vasc. Biol. 24, 2384–2390.

McGillicuddy, C. J., Carrier, M. J., Weinberg, P. D., 2001. Distribution of lipid deposits around aortic branches of mice lacking ldl receptors and apolipoprotein E. Arterioscler. Thromb. Vasc. Biol. 21, 1220–1225.

Milnor, W. R., 1979. Aortic wavelength as a determinant of the relation between heart rate and body size in mammals. Am. J. Physiol. Regul. Integr. Comp. Physiol. 237, R3–R6.

Mitchell, J. R. A., Schwartz, C. J., 1965. Arterial disease. Blackwell, Oxford.

Mitusch, R., Doherty, C., Wucherpfennig, H., Memmesheimer, C., Tepe, C., Stierle, U., Kessler, C., Sheikhzadeh, A., 1997. Vascular events during follow-up in patients with aortic arch atherosclerosis. Stroke 28, 36–39.

Mori, D., Yamaguchi, T., 2002. Computational fluid dynamics modeling and analysis of the effect of 3-D distortion of the human aortic arch. Comput. Methods Biomech. Biomed. Engin. 5 (3), 249–260.

Nakashima, Y., Plump, A. S., Raines, E. W., Breslow, J. L., Ross, R., 1994. ApoE-deficient mice develop lesions of all phases of atherosclerosis throughout the arterial tree. Arterioscler. Thromb. Vasc. Biol. 14 (1), 133–140.

Nguyen, K. T., Clark, C. D., Chancellor, T. J., Papavassiliou, D. V., 2008. Carotid geometry effects on blood flow and on risk for vascular disease. J. Biomech. 41, 11–19.

Nichols, W. W., O'Rourke, M. F., 1998. McDonald's blood flow in arteries. Theoretical, experimental and clinical principles, 4th Edition. Arnold, London.

Norrie, D. H., De Vries, G., 1978. An introduction to finite element analysis. Academic Press.

O'Dea, R. D., Waters, S. L., 2006. Flow and solute uptake in a twisting tube. J. Fluid Mech. 562, 173–182.

Papaharilaou, Y., Doorly, D. J., Sherwin, S. J., 2002. The influence of out-of-plane geometry on pulsatile flow within a distal end-to-side anastomosis. J. Biomech. 35, 1225–1239.

Parker, K. H., 1977. Chapter 16: Instability in arterial blood flow, In: Cardiovascular Flow Dynamics and Measurements. University Park Press.

Parker, K. H., Caro, C. G., 1993. Chapter 6: Flow in the macrocirculation: basic concepts from fluid mechanics, In: Magnetic Resonance Angiography, Concepts and Applications. Mosby, St. Louis.

Pedley, T. J., 1980. The fluid mechanics of large blood vessels. Cambridge University Press.

Pedley, T. J., 1995. High Reynolds number flow in tubes of complex geometry with application to wall shear stress in arteries. Symp. Soc. Exp. Biol. 49, 219–241.

Peiró, J., Formaggia, L., Gazzola, M., Radaelli, A., Rigamonti, V., 2007. Shape reconstruction from medical images and quality mesh generation via implicit surfaces. Int. J. Numer. Meth. Fluids 53, 1339–1360.

Peiró, J., Giordana, S., Griffith, C., Sherwin, S. J., 2002a. High-order algorithms for vascular flow modelling. Int. J. Numer. Meth. Fluids 40, 137–151.

Peiró, J., Peraire, J., Morgan, K., 1994. *Felisa* system reference manual. Version 1.1.

Peiró, J., Sayma, A. I., 1995. A 3-D unstructured multigrid Navier-Stokes solver. In: Morton, K. W., Baines, M. J. (eds.), Numerical methods for fluid dynamics V. Oxford University Press.

Peiró, J., Sherwin, S. J., Giordana, S., 2002b. High-order unstructured mesh generation. 1st conference on advances and applications of GiD, 20-22 February 2002, Barcelona, Spain.

Peraire, J., Peiró, J., Morgan, K., 1993. Multigrid solution of the 3-D compressible euler equations on unstructured tetrahedral grids. Int. J. Numer. Meth. Eng. 36, 1029–1044.

Perktold, K., Resch, M., Florian, H., 1991. Pulsatile non-Newtonian flow characteristics in a three-dimensional human carotid bifurcation model. J. Biomech. Eng. 113, 464–475.

Reitsma, S., Slaaf, D. W., Vink, H., van Zandvoort, M. A. M. J., oude Egbrink, M. G. A., 2007. The endothelial glycocalyx: composition, functions, and visualization. Pflugers Arch.: Eur. J. Physiol. 454, 345–359.

Richards, J. P., Weinberg, P. D., 2000. Distribution of disease around the aorto-coeliac branch of white carneau pigeons at different ages. Exp. Mol. Path. 66, 95–103.

Richardson, P. D., Davies, M. J., Born, G. V. R., 1989. Influence of plaque configuration and stress distribution on fissuring of coronary atherosclerotic plaques. The Lancet 2 (8669), 941–944.

Rose, G., 1991. Epidemiology of atherosclerosis. Br. Med. J. 303, 1537–1539.

Sayma, A. I., Peiró, J., 1995. A system for the solution of the 3D laminar navier-stokes equations using unstructured meshes. Department of Aeronautics, Imperial College London.

Schneider, J. E., Cassidy, P. J., Lygate, C., Tayler, D. J., Wiesmann, F., Grieve, S. M., Hulbert, K., Clarke, K., Neubauer, S., 2003. Fast, high-resolution in vivo cine magnetic resonance imaging in normal and failing mouse hearts on a vertical 11.7T system. J. Magn. Reson. Imag. 18, 691–701.

Schneider, J. E., McAteer, M. A., Tayler, D. J., Clarke, K., Channon, K. M., Choudhury, R. P., Neubauer, S., 2004. High-resolution, multicontrast three-dimensional-MRI characterizes atherosclerotic plaque composition in apoE-/- mice ex vivo. J. Magn. Reson. Imag. 20, 981–989.

Schroter, R. C., Sudlow, M. F., 1969. Flow patterns in models of the human bronchial airways. Respir. Physiol. 7 (3), 341–355.

Sebkhi, A., Weinberg, P. D., 1994. Age-related variations in transport properties of the rabbit arterial wall near branches. Atherosclerosis 106, 1–8.

Sebkhi, A., Weinberg, P. D., 1996. Effect of age on the pattern of short-term albumin uptake by the rabbit aortic wall near intercostal branch ostia. Arterioscler. Thromb. Vasc. Biol. 16 (2), 317–327.

Secomb, T. W., 1978. Flow in a channel with pulsating walls. J. Fluid Mech. 88, 273–288.

Shahcheraghi, N., Dwyer, H. A., Cheer, A. Y., Barakat, A. I., Rutaganira, T., 2002. Unsteady and three-dimensional simulation of blood flow in the human aortic arch. J. Biomech. Eng. 124 (4), 378–87.

Sherwin, S., Alastruey, J., Cookson, A., Doorly, D., Kazakidi, A., Parker, K., Peiró, J., Weinberg, P., 2008. Arteries and algorithms: Multiple scale modelling of flow in the cardiovascular system. In: Proceedings of the 16th Annual Conference of the CFD Society of Canada, Saskatoon, Saskatchewan, Canada, 9 - 11 June.

Sherwin, S. J., 1997. Hierarchical *hp* finite elements in hybrid domains. Finite Elem. Anal. Des. 27, 109–119.

Sherwin, S. J., Blackburn, H. M., 2005. Three-dimensional instabilities and transition of steady and pulsatile axisymmetric stenotic flows. J. Fluid Mech. 533, 297–327.

Sherwin, S. J., Karniadakis, G. E., 1996. Tetrahedral *hp* finite elements: algorithms and flow simulations. J. Comput. Phys. 124, 14–45.

Sherwin, S. J., Mathews, I., 2004. Finite element methods. MSc short course, Department of Aeronautics, Imperial College London.

Sherwin, S. J., Peiró, J., 2002. Mesh generation in curvilinear domains using high-order elements. Int. J. Numer. Meth. Eng. 53, 207–223.

Sherwin, S. J., Peiró, J., Shah, O., Karamanos, G. S., Doorly, D. J., 2000a. Computational haemodynamics: Geometry and non-Newtonian modelling using spectral/*hp* element methods. Comput. Visual. Sci. 3, 77–83.

Sherwin, S. J., Shah, O., Doorly, D. J., Peiró, J., Papaharilaou, Y., Watkins, N., Caro, C. G., Dumoulin, C. L., 2000b. The influence of out-of-plane geometry on the flow within a distal end-to-side anastomosis. J. Biomech. Eng. 122, 1–10.

Siggers, J. H., Waters, S. L., 2008. Unsteady flows in pipes with finite curvature. J. Fluid Mech. 600, 133–165.

Sinzinger, H., Silberbauer, K., Auerswald, W., 1980. Quantitative investigation of sudanophilic lesions around the aortic ostia of human fetuses, newborn and children. Blood Ves. 17, 44–52.

Sloop, G. D., Perret, R. S., Brahney, J. S., Oalmann, M., 1998. A description of two morphologic patterns of aortic fatty streaks, and a hypothesis of their pathogenesis. Atherosclerosis 141, 153–160.

Sobey, I. J., 1977a. Bio-fluid dynamics of bifurcations. Ph.D. thesis, University of Cambridge.

Sobey, I. J., 1977b. Laminar boundary-layer flow past a two-dimensional slot. J. Fluid Mech. 83 (1), 33–47.

Suo, J., Ferrara, D. E., Sorescu, D., Guldberg, R. E., Taylor, W. R., Giddens, D. P., 2007. Hemodynamic shear stresses in mouse aortas: Implications for atherogenesis. Arterioscler. Thromb. Vasc. Biol. 27, 346–351.

Svindland, A., Walløe, L., 1985. Distribution pattern of sudanophilic plaques in the descending thoracic and proximal abdominal human aorta. Atherosclerosis 57, 219–224.

Tarbell, J. M., 2003. Mass transport in arteries and the localization of atherosclerosis. Annu. Rev. Biomed. Eng. 5, 79–118.

Tuck, E. O., 1970. Unsteady flow of a viscous fluid from a source in a wall. J. Fluid Mech. 41 (3), 641–652.

Tutty, O. R., 1988. Flow in a tube with a small side branch. J. Fluid Mech. 191, 79–109.

Weinberg, P. D., 2002. Disease patterns at arterial branches and their relation to flow. Biorheology 39, 533–537.

Weinberg, P. D., Ethier, C. R., 2007. Twenty-fold difference in hemodynamic wall shear stress between murine and human aortas. J. Biomech. 40, 1594–1598.

White, R. A., 1989. Atherosclerosis and arteriosclerosis: Human pathology and experimental animal methods and models. CRC Press.

WHO, 2007. Cardiovascular diseases. World Health Organization Fact sheet 317.

Womersley, J. R., 1955. Method for the calculation of velocity, rate of flow and viscous drag in arteries when the pressure is known. J. Physiol. 127, 553–563.

Won, D., Zhu, S.-N., Chen, M., Teichert, A.-M., Fish, J. E., Matouk, C. C., Bonert, M., Ojha, M., Marsden, P. A., Cybulsky, M. I., 2007. Relative reduction of endothelial nitric-oxide synthase expression and transcription in atherosclerosis-prone regions of the mouse aorta and in an in vitro model of disturbed flow. Am. J. Pathol. 171 (5), 1691–1704.